Ferrocene-Terminated Self-Assembled Monlayers for the Electrochemical Non-Contact AFM Detection of Single Electron Redox Events

Harrisonn Robert Griffin

Department of Physics
McGill University
Montréal, Québec, Canada

February 4, 2020

A thesis submitted to McGill University in partial fulfillment of the requirements of the degree of **Master of Science**

Contents

List of Figures

Abstract

We aim to measure the charging energy of individual ferrocene molecules using Electrostatic Force Microscopy (EFM). Ferrocene molecules only accept a single electron upon charging, thus characterizing their electrical properties is more difficult than performing a traditional current-voltage transport measurement. However, one can utilize non-contact atomic force microscopy (NC-AFM) techniques as an alternative. By oscillating an atomic force microscope (AFM) cantilever over the sample, the metallic tip will be capacitively coupled to the ferrocene molecule. The charge of the molecule acts as a force on the cantilever in which we can observe by measuring the changing dynamics of the cantilever – primarily its resonance frequency and damping. This direct charge sensing technique can reveal valuable information about the ferrocene molecule, for example Coulomb-blockade effects and molecular reorganization energies.

To make such sensitive measurements, it is necessary to have a clean resonance of the AFM cantilever during NC-AFM measurements. Spurious mechanical resonances that arise from various mechanical components during piezoelectric excitation cause signal artifacts in the frequency shift and dissipation signals. In this work, we present an experimental setup to excite only the cantilever in a optical fiber interferometer via an optical excitation force.

The major focus of this thesis is the preparation and characterization of the samples. Self-assembled monolayers (SAMs) of alkanethiolates are formed on Au substrates via spontaneous adsorption from the liquid or vapor phase. Incubating a fresh Au substrate in a solution of alkanethiols provides a simple means to create organic thin films that can act as electron transport barriers. By making a mixed SAM with ferrocenylhexadecanethiolate ($FcC_{16}SH$) diluted to low coverage in pentadecanethiolate ($C_{15}SH$), we create an ideal sample to study the long-range electron transfer at the interface of the ferrocene molecule and Au substrate separated by the alkanethiolate tunneling barrier.

Although the formation of SAMs with n-alkanethiol systems seems straightforward, the faster adsorption kinetics of the $FcC_{16}SH$ in a mixed SAM makes it difficult to predict the surface density and distribution of $FcC_{16}SH$ molecules in the self-assembled layer. For successful single molecule redox measurements, we need to ensure full dispersion between the individual ferrocene molecules. When characterizing our SAMs with a combination of electrochemical cyclic voltammetry (CV) and AFM measurements, we see a disparity in the ferrocene molecule density by over a factor of 20 in our preliminary data, likely due to clustering of $FcC_{16}SH$ domains.

Abrégé

Notre objectif est de mesurer l'énergie de charge de molécules de ferrocène individuelles à l'aide de la microscopie à force électrostatique (EFM). Les molécules de ferrocène n'acceptent qu'un seul électron lors de la charge, il est donc plus difficile de caractériser leurs propriétés électriques que d'effectuer une mesure de transport courant-tension classique. Cependant, on peut utiliser comme alternative les techniques de microscopie à force atomique sans contact (NC-AFM). En faisant osciller un cantilever du microscope à force atomique (AFM) sur l'échantillon, la pointe métallique sera couplée de manière capacitive à la molécule de ferrocène. La charge de la molécule agit comme une force sur le porte-à-faux dans lequel nous pouvons observer en mesurant la dynamique changeante du porte-à-faux - principalement sa fréquence de résonance et son amortissement. Cette technique de détection de charge directe peut révéler des informations précieuses sur la molécule de ferrocène, par exemple des effets de blocage de Coulomb et des énergies de réorganisation moléculaire.

Pour effectuer de telles mesures sensibles, il est nécessaire d'avoir une résonance propre du cantilever AFM lors des mesures NC-AFM. Les résonances mécaniques parasites générées par divers composants mécaniques lors d'une excitation piézoélectrique provoquent des artefacts de signal dans les signaux de décalage et de dissipation de fréquence. Dans ce travail,

nous présentons un montage expérimental pour exciter uniquement le cantilever dans un interféromètre à fibre optique via une force d'excitation optique.

L'objectif principal de cette thèse est la préparation et la caractérisation des échantillons. Des monocouches auto-assemblées (SAMs) d'alcanethiolates sont formées sur des substrats en Au via une adsorption spontanée à partir de la phase liquide ou vapeur. L'incubation d'un substrat d'Au frais dans une solution d'alcanethiols constitue un moyen simple de créer des films minces organiques pouvant servir de barrières au transport d'électrons. En fabriquant une SAM mixte avec de ferrocenylhexadecanethiolate ($FcC_{16}SH$) dilué dans des pentadecanethiolate ($C_{15}SH$) à faible couverture, nous créons un échantillon idéal pour étudier le transfert d'électrons à longue distance à l'interface de la molécule de ferrocène et du substrat Au séparés par la barrière tunnel alcanethiolate.

Bien que la formation de SAM avec des systèmes n-alkanethiol semble simple, la cinétique d'adsorption plus rapide du $FcC_{16}SH$ dans un SAM mixte rend difficile la prédiction de la densité de surface et de la distribution des molécules de $FcC_{16}SH$ dans la couche auto-assemblée. Pour réussir les mesures d'oxydoréduction d'une seule molécule, nous devons assurer une dispersion complète entre les molécules de ferrocène individuelles. Lors de la caractérisation de nos SAM avec une combinaison de mesures de voltamétrie cyclique électrochimique (CV) et d'AFM, nous constatons une disparité de la densité en molécules de ferrocène d'un facteur 20 dans nos données préliminaires, probablement en raison du regroupement des domaines $FcC_{16}SH$.

Acknowledgements

I would foremost like to thank Professor Peter Grütter. His knowledge, insight of theory and instrumentation, and overall positive attitude made our weekly meetings enjoyable and productive. His support throughout my project was always encouraging, and his big-picture ideas gave my work meaning and motivation, especially during the times where instrumentation was not behaving.

I would like to thank Antoine Roy-Gobeill for his experimental and theoretical support during his time as a post-doc, but more importantly for his mentorship. He inspired my interests in programming, software, and open source, and would happily discuss my research even after he left the group. His attitude towards science has been what I have strived to achieve.

I would like to thank Antonella Badia and Eric Dionne at Universite de Montreal for all of their help in the preparation of the thiol samples used for my experiments. Eric's expertise in electrochemistry was an immense help in me understanding redox reactions in SAMs and properly preparing samples. All of the electrochemistry data in this work was performed with his assistance.

I thank Yoichi Miyahara for all of his help with operating and maintaining the low-

temperature atomic force microscope used in this work. His knowledge of electronics is immense, and he taught me everything I know about the operation and inner workings of the microscope.

I thank Tyler Enright for his support in the lab and his accompaniment in de-stressing bike rides. I also thank the rest of the Grütter group for their help and support.

A special thanks to Percy Zahl at Brookhaven National Labs for his support and development of GXSM open source scanning software. He offered valuable insight into the software, and his contributions to open science made this project possible.

A special thanks to Tor and Aude Bechu for their continued support during my degree, as well as the rest of my family.

Statement of Originality and Contribution

The following aspects of the thesis represent novel scientific advancements.

- Photothermal excitation and detection of a cantilever in a single optical fiber for low-temperature AFM experiments. This work is currently under review, and the manuscript is presented in chapter 3. Yoichi Miyahara is an equal contributor for this work.
- Correlating scanning probe microscopy images with electrochemistry cyclic voltammetry measurements of ferrocene-terminated alkanethiols self-assembled monolayers is presented in chapter 5. This work was performed by the author.

The Low-Temperature AFM described in chapter 2 has been developed by former generations of students, including Mark Roseman, Romain Stomp, Lynda Cockins, and Antoine Roy-Gobeil. The addition and characterization of photothermal excitation (chapter 3) was implemented by Antoine Roy-Gobeil, Yoichi Miyahara, and the author. The technique for template stripped gold and self assembled monolayer ferrocene thiol sample prepartaion of samples in the LT-AFM (chapter 4) was originally implemented by Antoine Roy-Gobeil, and further improvements (such as binary solution incubation and electrochemical characterization) were implemented by the author.

1 | Introduction

1.1 Motivation

Chemical reactions are ultimately the transfer of charges between different materials. Generating charges is a fundamental step in these reactions, as we see in reduction, oxidation, photovoltaics, and energy storage. Understanding how this exchange of charges happens is important to interpret the efficiency of their kinetics, and how they can be used for applications.

Recently, organic molecules have become popular for their potential applications in photovoltaics, molecular electronics, sensors, etc. If we want to create technology that exploits organic molecules, it should be obvious that we need to fully understand the properties of single isolated molecules, not just in bulk.

For these applications, we can imagine adsorbing some molecules to a surface. In a simple view, all of the molecules are chemically the same, thus they should behave identically. However, the heterogeneous environment in which the individual molecule is adsorbed will influence its energy states. In the real world, there are many different types of adsorption sites – flat terraces, bumps, steps, valleys – in which the molecules can be. The different local environments implies there are different local structure changes. In order to understand how different structures of the same molecule affect the sample, one needs to study the individual molecule, not one in bulk.

Experimentally characterizing the charging energies of molecules in these heterogeneous environments is limited by difficulties in isolating and analyzing a single molecule. Many instruments, especially in the electrochemistry domain, do not offer the resolution and imaging characteristics needed to study such small individual structures. However, we can use a microcantilever to image single molecules using scanning probe microscopy (SPM) techniques while also applying different potentials to perform topographical and energetic analyses of single molecules. Experimental data illustrating the effects of different local environments on molecules would advance the understanding between molecular structure and its properties, for example determining the most efficient structures for converting light into energy.

In this work, we describe samples in chapter 4 which are mixed self assembled monolayer (SAM) which has individual reactive ferrocene molecules sitting on top of an insulating barrier of alkane thiols. The SAM is formed on atomically flat gold, which provides a back gate between the tunnel barrier and the reactive ferrocene, giving us a playground in which we can study the electronics of single molecules.

We aim to measure how location and number of neighboring ferrocenes influence the oxidation and reduction energies of a given single ferrocene molecule. We study the effects of varying the concentration of ferrocene molecules in the sample using traditional electrochemistry techniques and AFM, with the goal of producing well characterized and controlled samples for single molecule charging experiments using SPM. Additionally, we describe in detail the instrumentation used in our home built low temperature AFM which will be used in the future for the single electron charging experiments.

1.2 Single Electron Spectroscopy via NC-AFM

Although there are different varieties of SPM techniques, they involve bringing a sharp tip on a microcantilever near the surface of a sample with sub-nm precision in order for imaging and spectroscopy. In scanning tunneling microscopy (STM), the probe is used as an electrode to measure tunneling current between the tip and the sample. Conductance and transport measurements of our ferrocene molecule can be performed using the double tunnel barrier technique as shown in figure 1.1, but requires very close proximity to achieve a significant tunneling current. This perturbs the molecule, meaning we may be measuring its perturbed ground state. Additionally, since this is a two terminal configuration, one has to disentangle 2 coupling constants.

Instead of using STM, we can use AFM to measure forces instead of a tunneling current. Using the cantilever as a force sensor, we can measure the capacitive forces between the molecule and the cantilever. A bias voltage can be applied to the cantilever tip, acting both as a movable gate and an electrode to detect single electrons. This method is favorable over STM for charge sensing as it is less invasive (can be performed at longer ranges on the order of 10 nm) and only requires a single tunnel barrier, as shown in figure 1.1.

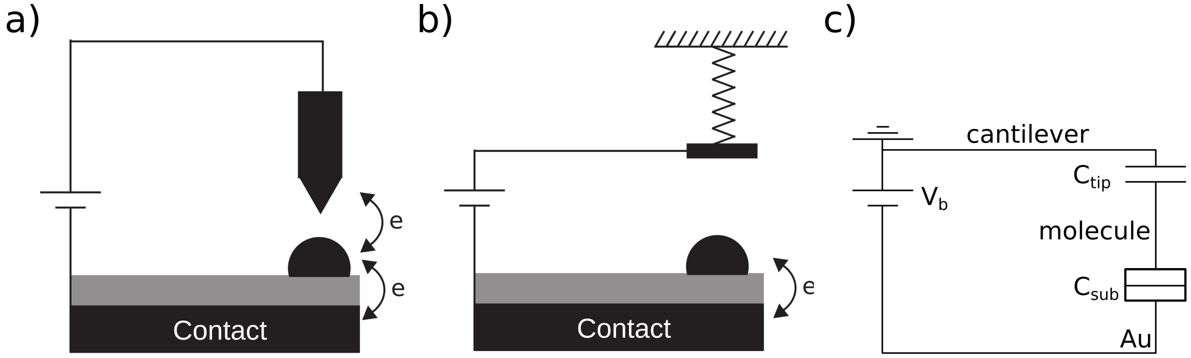

Figure 1.1: Schematic of scanning probe microscopy techniques used for electron charging experiments. The grey region is a tunnel barrier and the arrows indicate electron tunneling. a) shows the setup for STM, where the sharp tip is brought very close to the sample to perform transport measurements. b) shows the setup up for charge sensing via AFM. The tip is brought close to the sample and charges are detected via the capacitive force on the cantilever [1]. c) shows the single electron box circuit for the configuration adapted from [2].

For full details on the charge sensing technique using AFM, we direct you to the thesis of Antoine Roy-Gobeil [1]. This explains the charge sensing mechanism in full depth, and all of the relevant theory required to understand the single electron transport. It reviews the literature for quantum dots electrostatically coupled with mechanical oscillators, and provides an efficient algorithm to determine the response of the coupled electro-mechanical systems using linear response theory [4].

In more recent work, it has been shown that this direct charge sensing technique can reveal valuable information about the quantum mechanical processes of a single ferrocene molecule by measuring the electric force associated with long-range electron transfer redox events. These processes are manifested via electron tunneling and the associated nuclear vibronic states from the intramolecular vibrational relaxation. The AFM cantilever response at varying oscillation amplitudes during NC-AFM experiments exhibits discrete steps which agree with the single-electron tunneling model with quantized nuclear state transitions associated with the reduced and oxidized electronic states. This means that with this technique, we can simultaneously study quantized electron and nuclear dynamics of a single ferrocene molecule [5].

1.3 Structure of Thesis

In chapter 2 of this thesis, we discuss the instrumentation of the home built low temperature AFM. This includes details on the hardware and software, as well as information on how to properly mount and align the cantilever and sample. In chapter 3, we present the manuscript that has been submitted to the European Physics Journal of Techniques and Instrumentation.

This manuscript describes the implementation of a single fiber approach for optical excitation and detection of a cantilever in our microscope. In chapter 4, we detail the preparation of our atomically flat template stripped gold and self assembled monolayer samples. The description of characterizing the monolayers with electrochemistry measurements is also included. Finally, in chapter 5, we present preliminary data showing the disparity between traditional electrochmistry and AFM in characterizing the number of molecules on the surface of our self assembled monolayer samples.

2 | Instrumentation

2.1 The Low-Temperature Atomic Force Microscope

The atomic force microscope that we use for this thesis is a home built low-temperature atomic force microscope (LT-AFM). The microscope was engineered and designed with considerations to ensure the highest measurement sensitivity as possible. The operation, hardware, and characterization of the Fabry Perot interferometer of our microscope are discussed in chapter 3, but here we will elaborate on some details of the microscope necessary for successful operation.

During my work, I converted our LT-AFM to being a fully open-source microscope. This was was ultimately made possible by the open-source microscopy package GXSM [6] and the open-source scanning probe microscopy controller SoftdB MK2-A810 [7] that was designed especially for GXSM[8]. This software and hardware make scanning probe microscopy accessible to lab groups world-wide, and allow one to build and operate an AFM for a fraction of the price of a commercial system. In addition to these, we have implemented additional hardware and software to control other parts of the microscope, primarily the piezoelectric walkers to control the fiber and sample walker position.

Open-source hardware and software is a key aspect of promoting open access science. I am proud to be a contributor to the open science field and hope that others will follow suit to help make science accessible to everybody.

2.1.1 LT-AFM Hardware

The experimental setup of our LT-AFM is shown in figure 2.1, and the operation of the AFM in non-contact mode is discussed in chapter 3. We will discuss all of the hardware components of the LT-AFM in more detail here, and specify their role in the successful operation of NC-AFM at low temperatures.

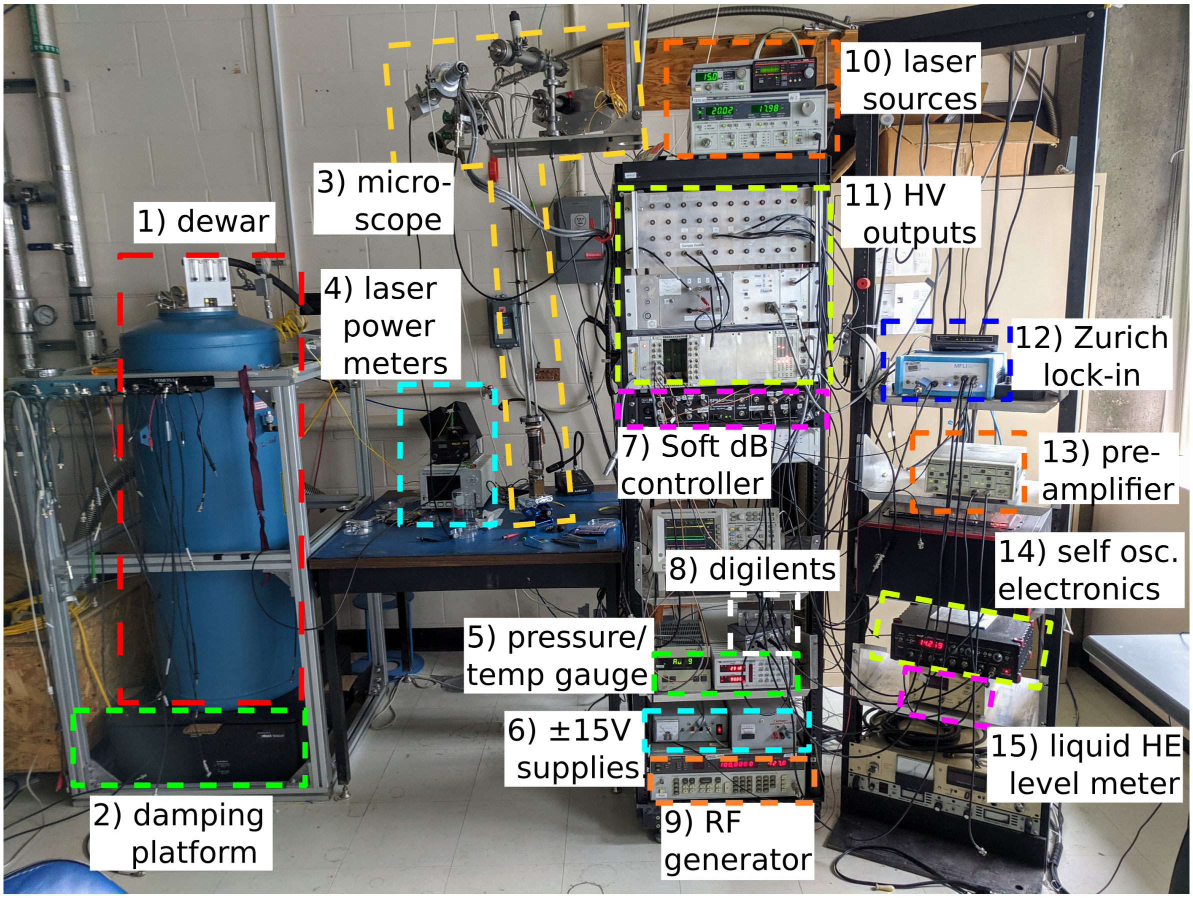

Figure 2.1: The LT-AFM is and all of its constituent hardware as shown in the lab. The microscope (3) is outside of the dewar (1), in its position where we would prepare the sample, cantilever, and closing of the can for experiments.

The original design of the microscope was by Mark Roseman [9] and was further improved by Romain Stomp [10], Lynda Cockins [2], and Antoine Roy-Gobeil [1]. The current AFM head design is shown in figure 2.2.

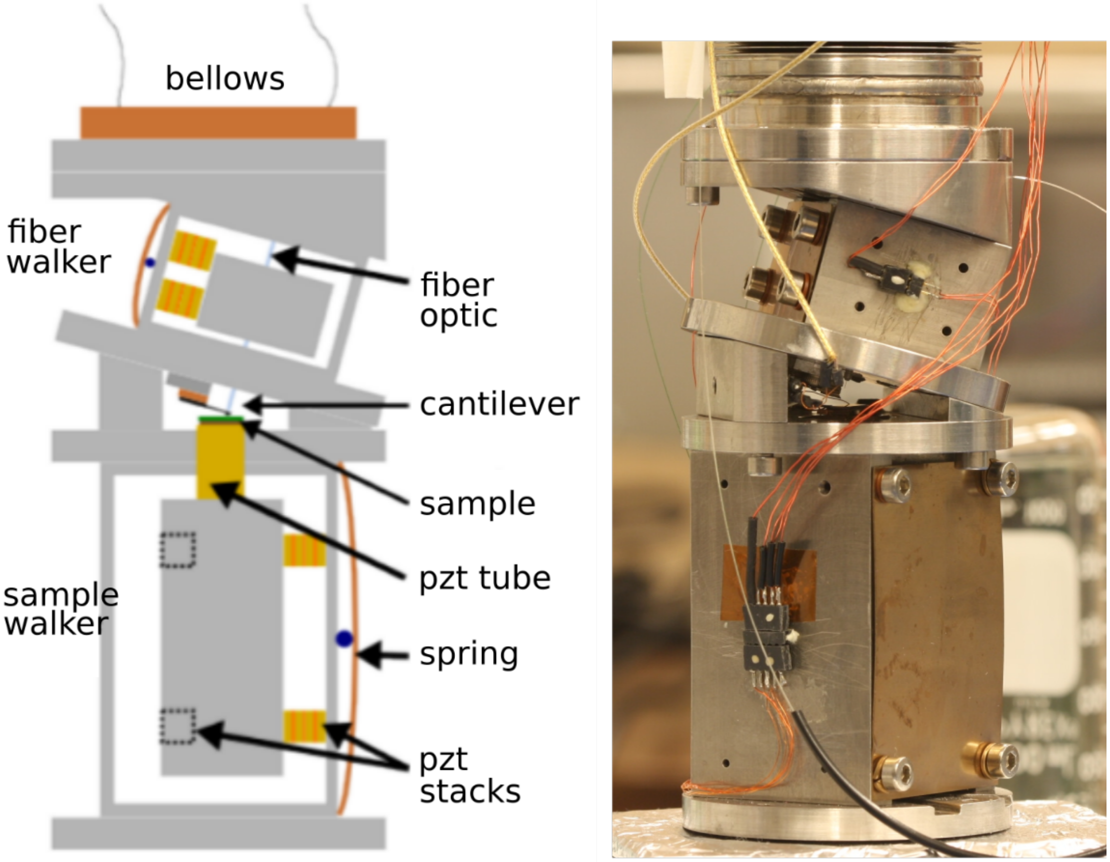

Figure 2.2: The current design of the LT-AFM head. The schematic diagram is shown in (a) and a picture of the assembled head is shown in (b).

Mounting of Cantilever onto Holder

The cantilever used in our microscope as the force sensor is an NCLR Nanosensors cantilever [11]. This cantilever is coated with aluminum on the backside for increased reflectivity of the incident detection laser and platinum-coated on the tip-side to make it conductive for charging experiments. These cantilevers are approximately 200 μm long and on average have a resonant frequency of roughly 150 kHz.

To mount the cantilever into our microscope, we attach the cantilever to a specially designed and machined holder which can then be screwed into our microscope body. There are several different ways to attach the cantilever to the holder, primarily by using metallic paint, metallic epoxy, or a mechanical clamp. Each of these means of attaching the cantilever has been explored, and are still being used for current experiments.

Empirically we find that certain mounting configurations cause the cantilever to have a low Q-factor. This is likely a result of some energy being dissipated into the cantilever chip, which theory and modeling have suggested is possible simply from the presence of silicon dust from moving the cantilever with tweezers [12, 13, 14]. Since the charging measurements we ultimately want to take are of the dissipation of energy and frequency shift of the cantilever, we must have a high Q-factor and as little energy dissipation into the chip as possible. We have explored all of the different means of attaching the cantilever in this work. The cantilever holder was always cleaned with ethanol and wiped down with a fiber particle-free cotton swabs before installing a cantilever.

The first way in which we explored attaching the cantilever to the cantilever holder was by using conductive silver paint. This paint from Sigma Aldrich company uses acetone as the solvent, which means that the drying time is much quicker than those silver paints which are water-soluble. For mounting, the cantilever chip was placed in the microfabricated grooves of the cantilever holder which perfectly match the protrusions on the cantilever chip. The top of the chip was pushed on with forceps to ensure that it was in its correct position, and would not slide or rotate. Then, the silver paint was thoroughly mixed, and a toothpick was used to pick up a drop of paint and place it on to the back of the cantilever chip, which was then left to dry.

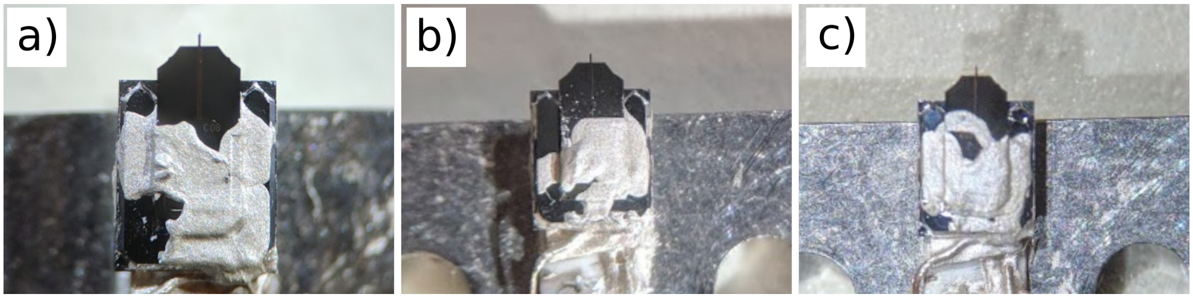

Figure 2.3: Pictures of various cantilevers attached to the cantilever holder via conductive silver paint. a) b) and c) illustrate the inconsistency in which the silver paint can be applied.

Several examples of painted on cantilevers are shown in figure 2.3. The technique we employed was to use a toothpick to deposit a single drop of silver paint on the back end of the chip (opposite side of the cantilever) such that the paint would bridge the top of the chip to the cantilever holder. As you can see, the resulting paint was somewhat uncontrolled and hard to reproduce. Much of this can be attributed to the viscosity of the paint. Since the solvent would evaporate, more solvent would be added before it could be used. Since it is difficult to know exactly how much to add, the resulting viscosity of the paint would vary. The less viscous the paint, the more it would run along the chip. Ideally, a thicker blob would be best to produce a single drop of contact. To remove the cantilever, the paint could be removed with a combination of acetone and scraping away with a razor blade.

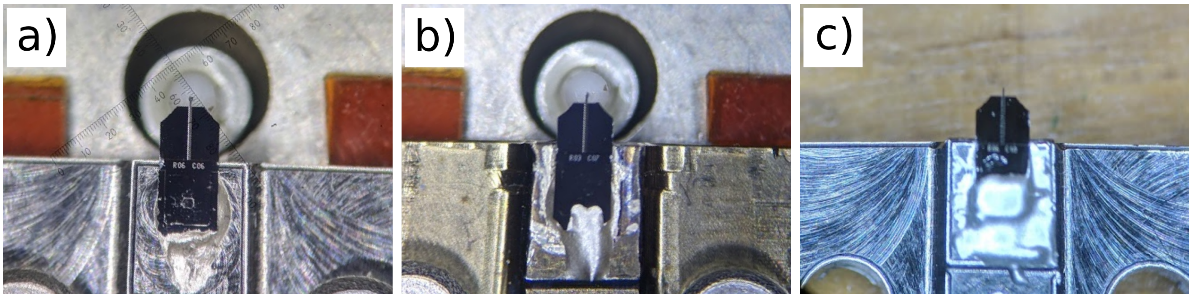

Figure 2.4: Pictures of various cantilevers attached to the cantilever holder via conductive silver epoxy. a) and b) The ideal placement of a drop of epoxy on the back of the chip. c) An example of a chip that had much more epoxy on it.

A stronger and more robust alternative to adhesion via silver paint is a conductive metal epoxy. We used EPO-TEK H20E electrically conductive silver epoxy. This two-part epoxy would be measured out in a 1:1 ratio according to the specification sheet and thoroughly mixed for 60 seconds with a toothpick. Similarly to the paint, the epoxy was applied to the back cantilever chip with a toothpick. Ideally, we tried to make a single blob connecting the chip to the holder. Once the epoxy was placed, the chip and cantilever holder were baked in a covered Petri dish at 150°C for 60 minutes. The epoxy's conductive properties were electrically verified by checking the resistance between the holder and the chip. Successfully cured epoxies would yield resistances of approximately 10 Ω.

Examples of different cantilevers with epoxy are shown in figure 2.4. As you can see, the deposition of the epoxy was cleaner and more reproducible than the silver paint. Although the epoxy is easier to deposit, it is impossible to remove without damaging the cantilever. We remove the epoxy by baking the cantilever holder at a temperature of 450°C, which is above the degradation temperature of epoxy. This burns the epoxy and turns it into ash, but also burns the cantilever. Therefore, this method does not allow for reuse of the cantilever for future experiments, or for the characterization of cantilevers after removal from the holder.

The final method we use for mounting cantilevers was by using a mechanical clamp. A piece of copper-beryllium was cut into a rectangle and bent into a leaf spring. A hole was drilled on one side which allows the leaf spring to be attached to the cantilever holder. On the end of the leaf spring which makes contact with the chip, we attached a 0.4 mm sapphire hemisphere to the underside with EPO-TEK H20E metallic epoxy, as shown in figure 2.5 a. The surface of the hemisphere was also covered in this conductive epoxy and sanded until smooth, allowing for a conductive single point of contact onto the chip.

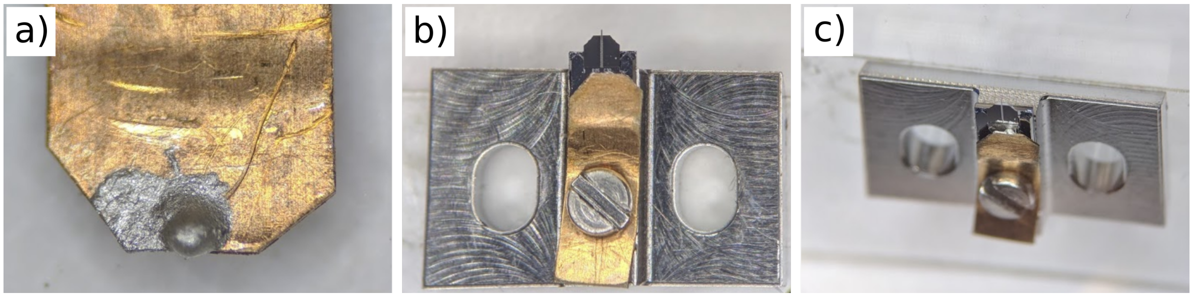

Figure 2.5: Pictures of the copper-beryllium leaf spring used to mechanically clamp the cantilever. a) The placement of the 0.4 mm sapphire hemisphere attached via conductive metal epoxy. b) and c) A successfully clamped cantilever from different angles.

The chip would be placed on the chip holder, and the loosened leaf spring would be placed on top of the chip, trying to center the sphere laterally on the chip. The leaf spring could then be tightened by tightening the screw. Qualitatively, we would tighten the spring until just past finger tight. The attached configuration can be seen in figure 2.5 b and c.

The mechanical leaf spring clamp is my preferred method as it allows for quick and efficient mounting and dismounting and is non-destructive to cantilevers. Additionally, its ability to tune the point of contact in one dimension along the radius of the leaf spring means we can specifically choose our point of contact. This could be useful for investigating the effect of clamping on mechanical nodes in the chip and its effect on dissipation.

Thin Film Coating of Fiber End

We coat the fiber end in a thin film of TiO_2 to increase back reflection as discussed in chapter 3. For completeness, a diagram showing the optical setup for making the fibers is shown in figure 2.6. An incident laser diode with a wavelength of 1550 nm travels through an optical coupler, where it is split in half. Half of the incident light travels to a reference photodiode detector and the other half to the fiber end. The reflected light off the fiber end then travels back through the optical coupler, where half of it goes to another photodiode detector. By monitoring the two photodiodes, we can measure the back reflection of the fiber in real-time.

A perfectly cleaved bare fiber will have a back reflection of approximately 3.3%. These would be the ideal candidates used for applying the thin film. As reported in the manuscript, back reflections of up to 35% are achievable.

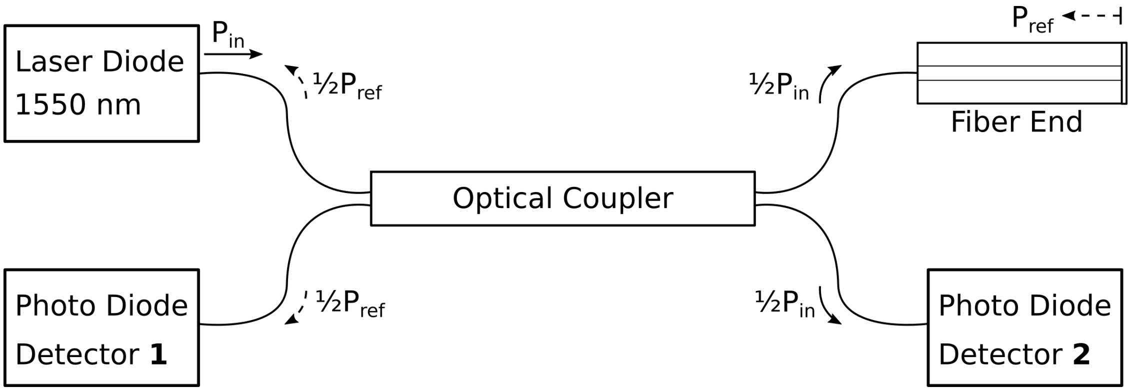

Figure 2.6: The schematic diagram showing the optical set up used for coating fiber ends with a thin film of titanium dioxide. The back reflection of the fiber end was measured in real-time using the two photodiode detectors.

Optical Fiber - Cantilever Alignment

As discussed in chapter 3, our LT-AFM operates with a Fabry-Perot interferometer (FPI) as our cantilever detection system. This cavity is formed from the reflective coating of an AFM cantilever and the end of a optical fiber cable coated in a TiO_2 thin film to increase back reflectivity and is discussed in depth in the manuscript.

For the successful operation of our microscope with the FPI detection cavity, it is essential to ensure that the two mirrors in our cavity are aligned. Alignment is done manually by hand and is determined primarily by human inspection, although it can be verified by looking at the cavity behavior in the interferometer signal.

The cantilever alignment procedure is shown in figure 2.7. Firstly, we look down at the fully retracted fiber without the cantilever mounted using a tabletop stereoscope. The stereoscope is adjusted such that the fiber end and ferrule are as close to parallel with our viewpoint. This is done by focusing on the top of the fiber, then the bottom of the ferrule, and seeing if any edges of the ferrule can be seen. If some part of an edge is seen, this means that the angle isn't correct and it is adjusted until the edge is no longer seen. Additionally, there are concentric rings around the ferrule that we can use as a visual aid. We try to get these rings to be perfectly even all around the ferrule.

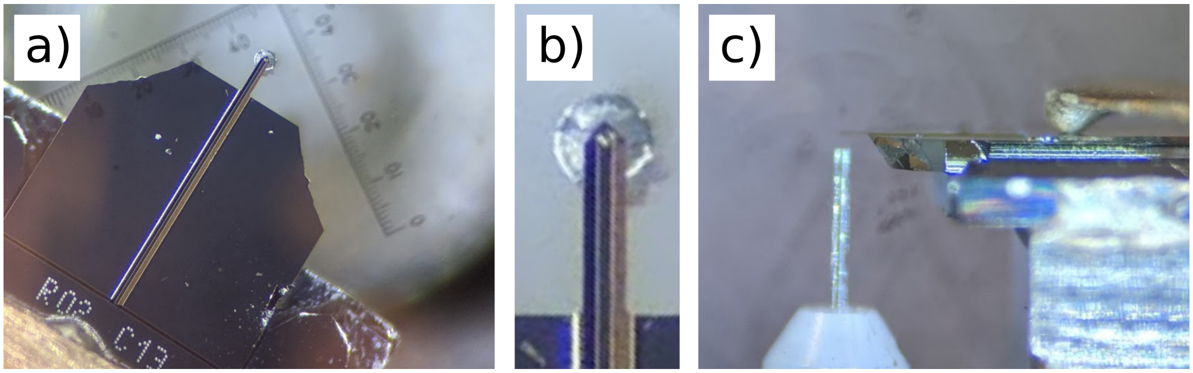

Figure 2.7: Pictures showing the proper alignment of the cantilever over the fiber end. a) and b) The optimal position for the cantilever relative to the fiber. c) The fiber-cantilever separation used for alignment. The cantilever shown is 231 μm long, 33 μm wide, and 7 μm thick.

Once the alignment of the stereoscope with fiber is complete, we can then mount the cantilever holder onto the microscope body. We adjust the cantilever holder position until we center the tip of the cantilever over the fiber end. We want the fiber to be as close to the edge of the cantilever as possible, ensuring we have the highest sensitivity. As mentioned in figure 2 in chapter 3, the actual fiber core only has a diameter of 8 μm. By centering the cantilever along the cantilever axis and slightly past the center of the fiber, we can achieve the optimal position, as shown in figure 2.7 a) and b).

With the optimal position obtained we then approach the fiber to the cantilever until it is approximately 200 μm away, or one cantilever distance, as shown in figure 2.7 c. In this position, we can finely adjust the position if necessary. Firstly we can make sure that the cantilever looks to be in our optimal position. Then we can monitor the interferometer signal of our cavity and make sure that we see interference fringes.

Piezoelectric Walkers

In our microscope set up, we need to be able to approach and retract both the optical fiber interferometer and the sample. The fiber needs to be able to move towards or away the cantilever to adjust our FPI cavity, allowing us to choose the desired interferometer sensitivity. To move the fiber and sample with the nanometer precision we require, we use stick-slip piezo motors with shear piezoelectric stacks, which can be seen in the microscope schematic in figure 2.2.

Piezoelectric materials exhibit the piezoelectric effect; a linear strain change as a function of applied electrical field. If the material is stressed by squeezing or bending, the piezoelectric crystal produces a polarization P proportional to the stress applied. Conversely, by applying a voltage to the material and inducing a polarization, we can cause the crystal to expand or contract [15].

We can use this effect to our advantage by stacking piezoelectric sheets interlaced with an insulating layer, as the schematic in 2.8 a shows. Our shear piezo stacks are home built by glueing piezoelectric squares to aluminum oxide insulating layers with conductive metal epoxy. When a sawtooth waveform is applied to the shear piezo stack, the entire stack shears towards one direction as the voltage is ramped up, as shown in the displacement in figure 2.8 b). The polarity of the applied voltage will determine if there is a negative or positive displacement.

At the end of the ramp up, the voltage quickly drops to 0 V, causing the piezo stack to contract to its initial orientation. If the effective inertia of the stack is tuned properly, the friction on the piezo will be low enough so that it contracts to it's new position via stick slip motion. The inertia can be adjusted via the springs on the side of the AFM head, as

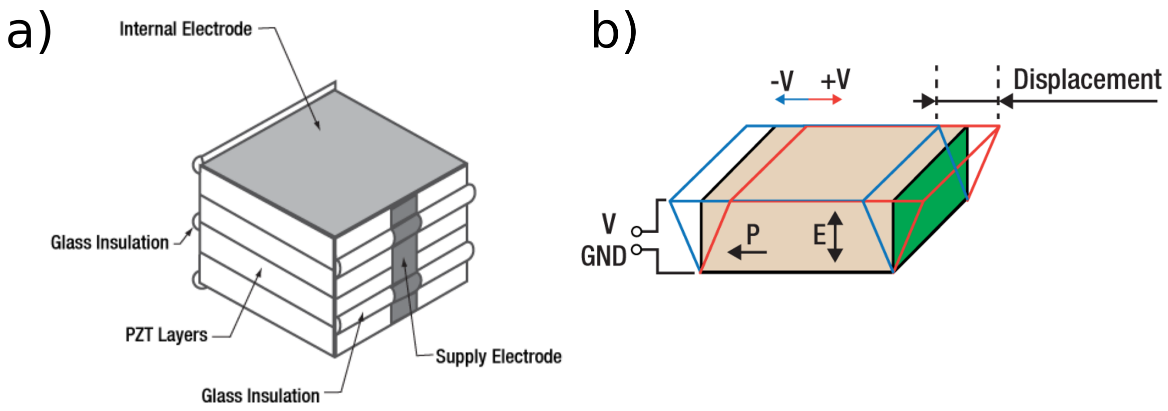

Figure 2.8: a) A schematic of a sample shear piezoelectric stack. In our configuration, the glass insulation is aluminum oxide. b) The shear movement of the piezo stack when a positive or negative voltage is applied to the supply electrode.

shown in figure 2.2. The sample walker in its fully extended and fully retracted positions are shown in figure 2.9. Increasing the tension of the springs increases the force (and thus effective mass and thus inertia) of the piezowalker. A too large spring tension will lead to a large static friction that can not be overcome by the piezo walker. If the tension (and thus inertial moment) is too small the piezowalker will just shake and not move.

In our experiments, before approaching the sample via an auto approach, we manually approach until the tip is approximately 50 microns from the surface (or 1/4 of a cantilever length), as shown in figure 2.10. This allows for a quicker auto approach once the microscope can is closed for experiments. For moving the piezos, we program two Analog Discovery 2 by Digilent for both generating wave forms and recording the interferometer signals. These are shown as 8 in figure 2.1. Digilent Analog Discovery 2 is a USB oscilloscope and multi-function instrument that allows users to measure, visualize, generate, record, and control mixed-signal circuits of all kinds.

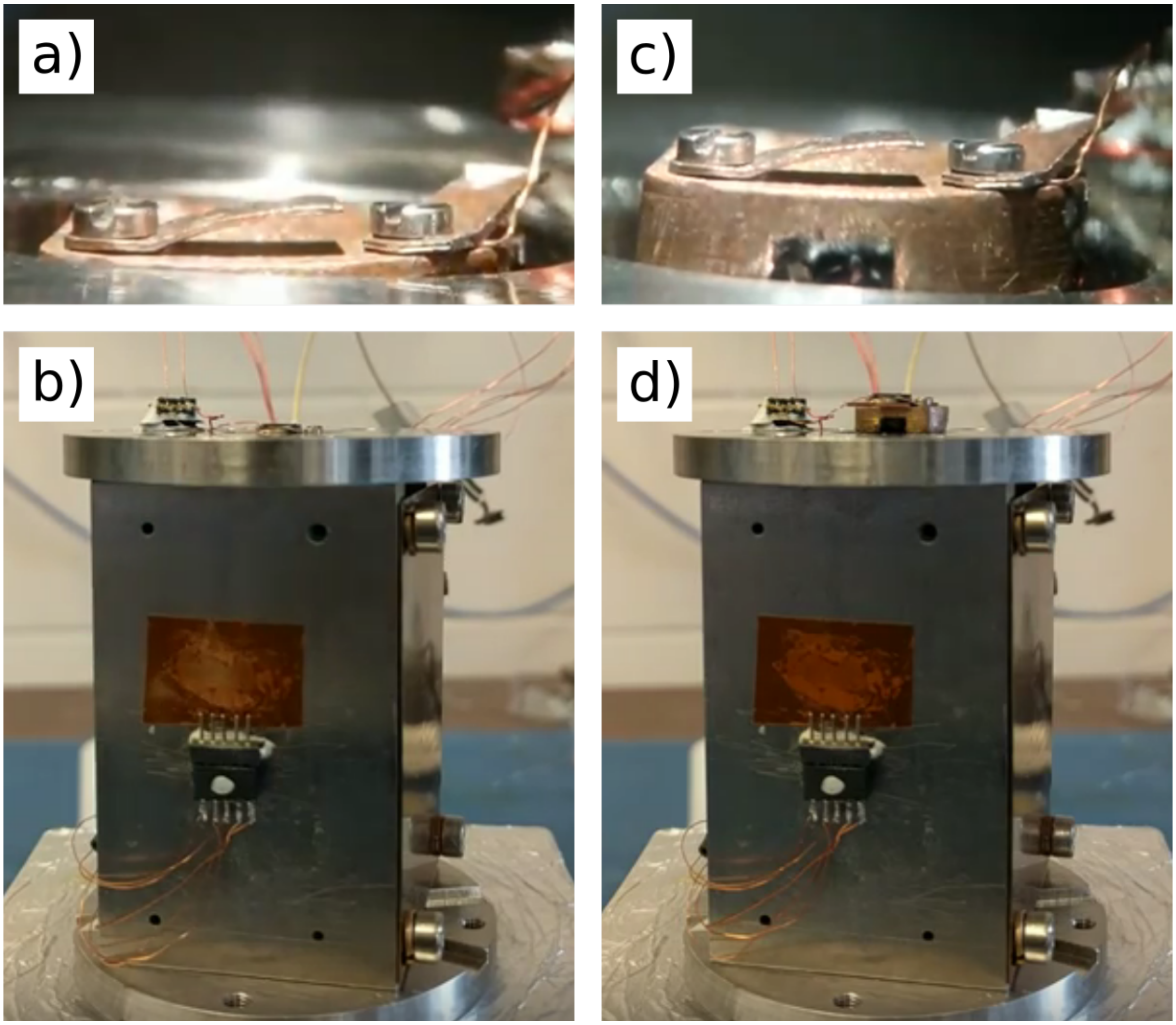

Figure 2.9: a) and b) The sample walker in its fully retracted position. Through applying sawtooth waveforms of a specific voltage, we can step the sample walker to its fully extended position, as shown in c) and d).

We can move the optical fiber using the fiber walker piezo stack, which is discussed in chapter 3. By measuring the interferometer signal as we move the fiber, we can measure the peak separation in steps, as shown in figure 2.11. An example of a fiber retracting a greater distance is shown in figure 2.12 top. We can then plot the histogram of the step sizes between peaks, as shown in figure 2.12 bottom. Since the peak separation is equal to half of the wavelength of the detection laser, we can convert the step size into distance. In this example, the mean peak separation is 31.7 steps which is approximately 24.4 nm. The standard deviation of peak separation is 1.87 steps (1.4 nm), showing the consistency of the fiber walker over large distances. If the same amplitude waveform is used for approaching the cantilever as retracting, the step sizes will be larger for the approach. This is due to gravity helping pull the fiber walker towards the cantilever. However, since we do not need to overcome the weight of the fiber walker while approaching (as we do in retracting), it is possible to move the fiber walker with smaller amplitude waveforms, thus taking smaller steps. Typical step sizes when approaching can be as small as 15 nm (or 50 steps between peaks). A typical sawtooth waveform would have an amplitude of 1.5 V with a frequency of 2 kHz (500 μs rise time and 0.1 μs decay time), with successive pulses every 250 ms.

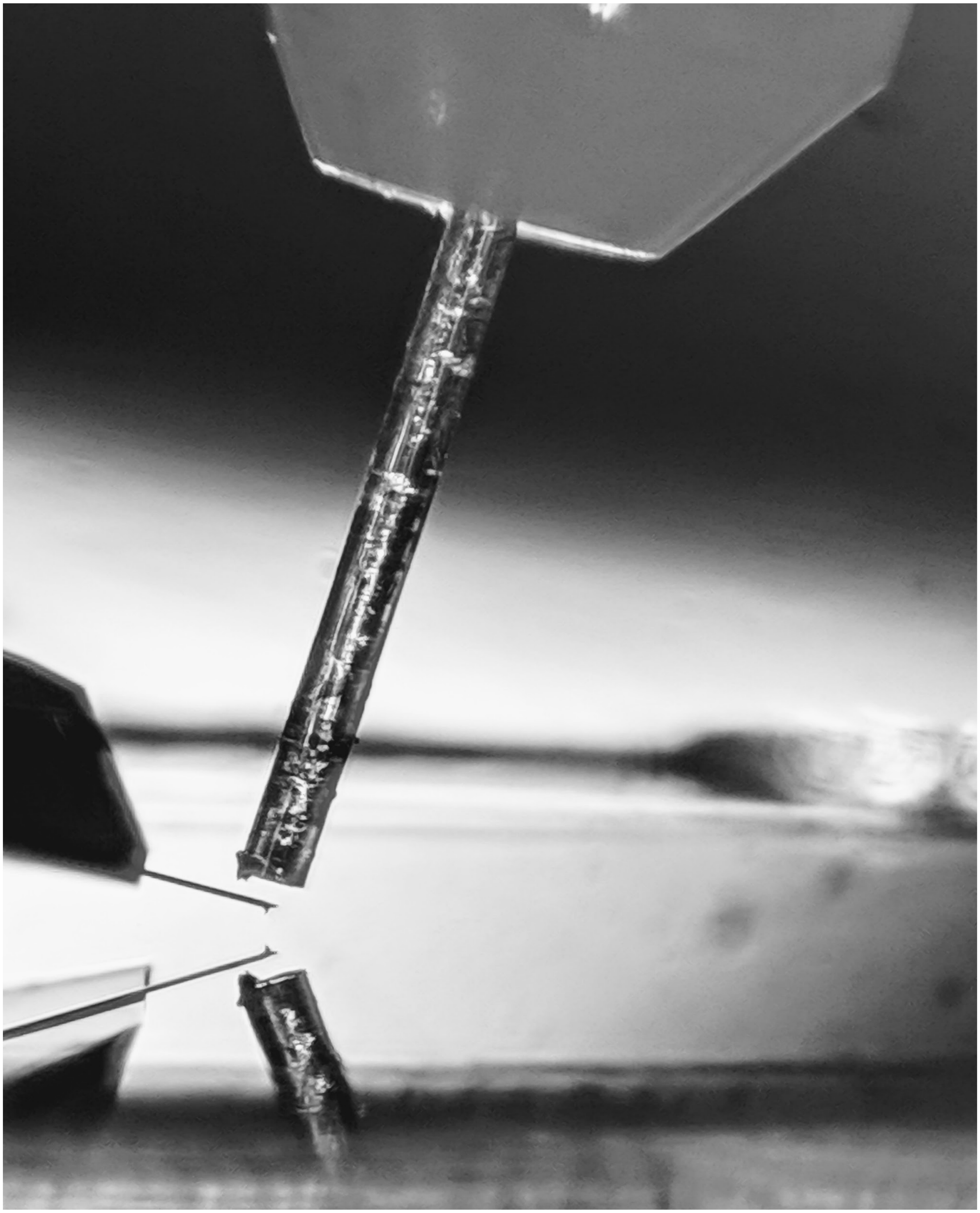

Figure 2.10: A photograph of the fiber, cantilever, and sample configuration in the microscope. The tip is approximately 50 microns from the surface (or 1/4 of a cantilever length). One can observe the reflection of the tip and fiber on the flat sample.

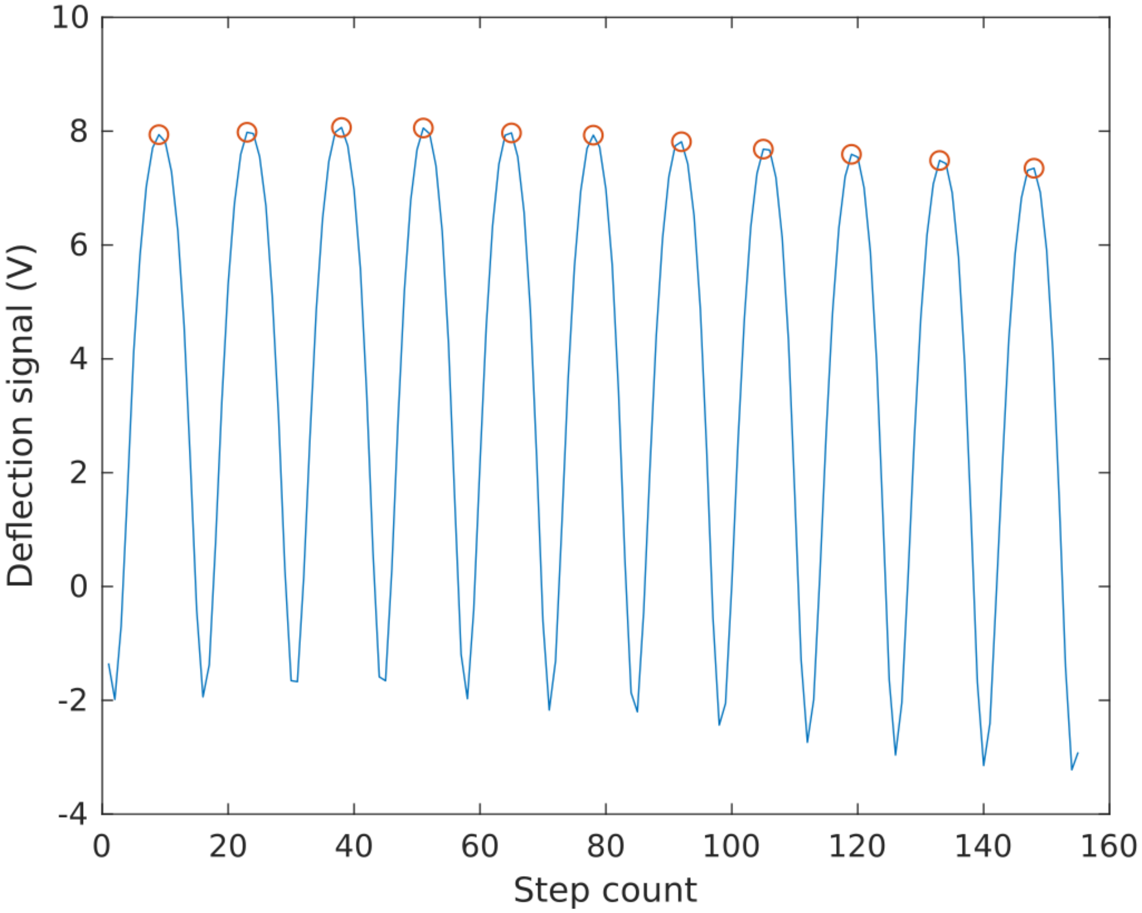

Figure 2.11: An example of retracting the fiber from the cantilever showing the interferometer signal as a function of walker steps. The detected peaks are circled.

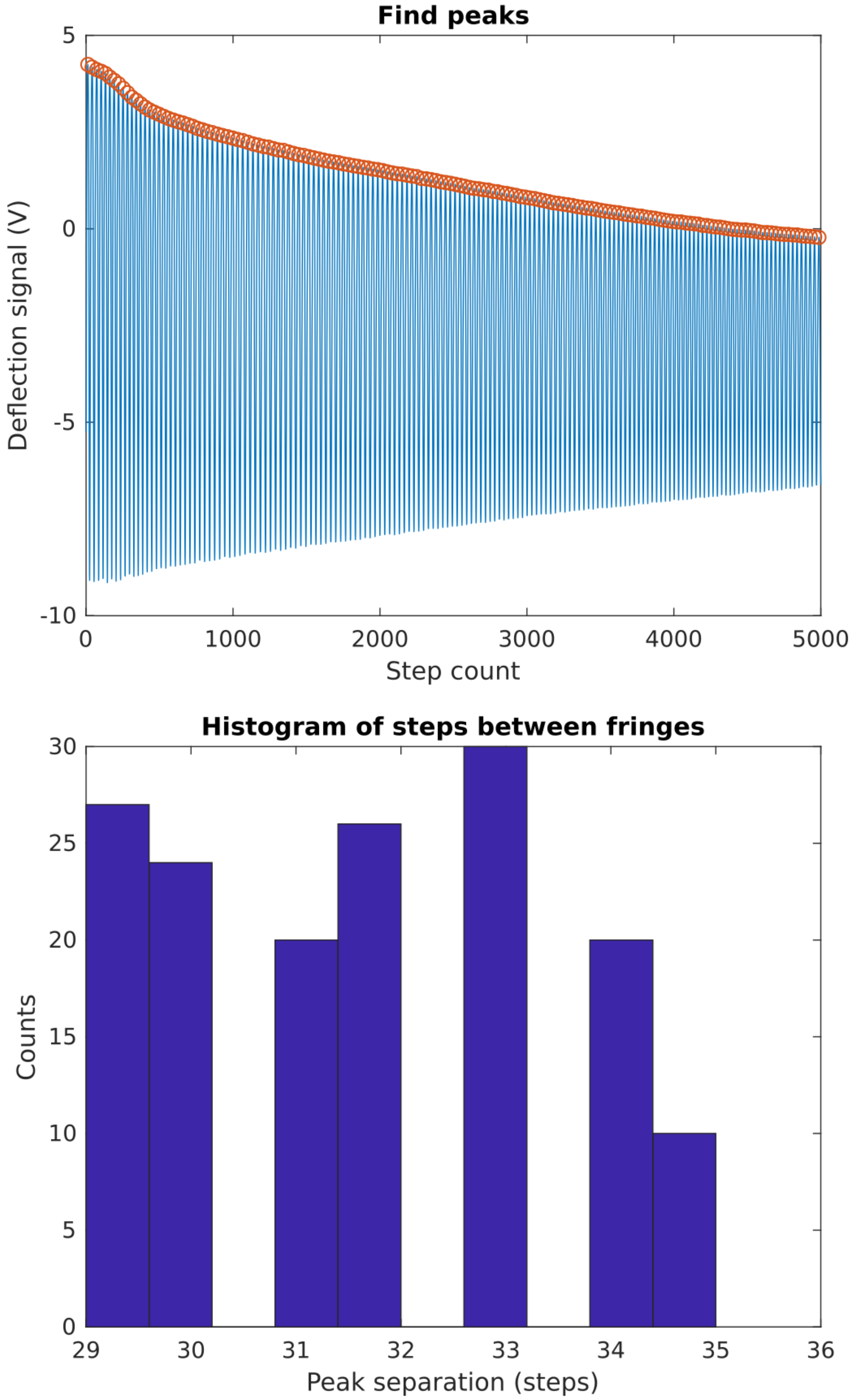

Figure 2.12: An example of retracting the fiber 158 fringes, or 118.5 μm, from the cantilever. The top shows the interferometer signal with detected peaks. The bottom shows the histogram of peak separation in steps. The mean peak separation is 31.7 steps with a standard deviation of 1.87 steps.

Optics Box on Microscope

The optical components used to build our interferometer and to perform optical excitation of our cantilever is described in depth in section 3. To complete the story, here we show a picture of the optics box of the microscope, as seen in figure 2.13. All of the components here are detailed in the manuscript and this instrumentation section, with this image simply providing visual assistance.

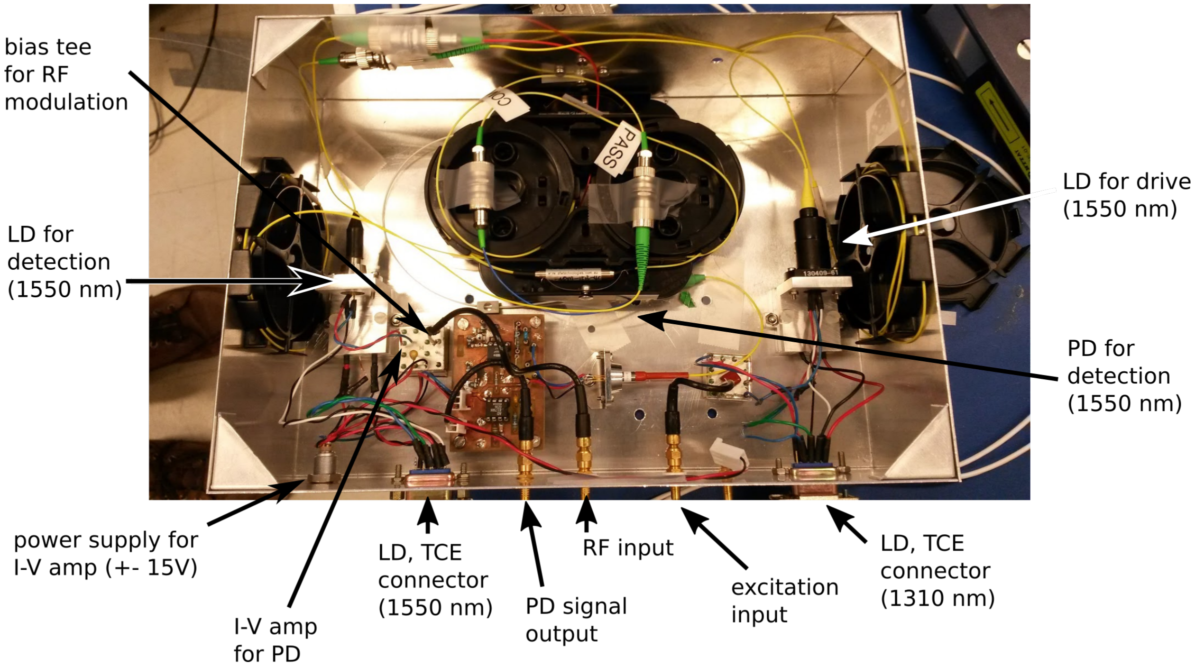

Figure 2.13: A labeled picture of the optics box on the microscope. This serves as the connection between the laser sources on the rack and the optical fiber in the microscope, and is the heart of the optics for the experiment.

Electronics for Non-Contact AFM

To operate the LT-AFM in non-contact AFM mode, we need to operate the cantilever in self-oscillation mode, as discussed in detail in the thesis on Antoine Roy-Gobeil [1]. The specifics to the set up are describe in chapter 3, but we will briefly describe them here.

In order to achieve self-oscillation, the cantilever needs to be always driven on its resonance frequency. To achieve this, the output of the oscillator is used as a feedback signal to drive the excitation system. The detector output can be phase-shifted and amplified to achieve a steady amplitude in a high Q factor resonator [16]. To realize self-oscillation in our experiment, we use the phase and amplitude easyPLLplus controller by Nanosurf, as shown as 14 in figure 2.1. Note we slightly customized the easyPLL, as described in Antoine's thesis [1].

The frequency shift measurement was made using a phase-locked loop (PLL) frequency detector (HF2LI with PLL option, Zurich Instruments) with a detection bandwidth of 100 Hz. This is shown as 12 in figure 2.1. The DC interferometer detection signal for both frequency tracking and self-oscillation is amplified using a low noise preamplifier Model SR560 by Stanford Research Systems, shown as 13 in figure 2.1. This is the second amplification stage after the I/V converter.

For scanning and performing bias spectroscopy measurements, we use the DSP based SoftdB MK2-A810 open-source SPM controller, shown as 7 in figure 2.1.

Temperature, Pressure, and RF Controls

In order to measure the temperature of the microscope head during experiments, we use a cryogenic temperature probe and controller by LakeShore Cryotronics. This provides reliable temperature readings from room temperature (278 K) down to liquid helium (4 K). To monitor the pressure of the vacuum can in which the microscope is contained, we use a Pirani gauge and cold cathode ionization gauge controlled by a Total Pressure Gauge Controller TPG 300 by Pfeiffer Vacuum. These are shown as 5 in figure 2.1. A characteristic pump down curve for our microscope being pumped down with a turbopump is shown in figure 2.14. Pressures of 10^{-4} mbar are reached after 8 hours while pumping down to pressures of 10^{-5} mbar are reached after 85 hours of pumping. Before these measurements, the microscope was in ambient lab air for several weeks. Pump down times are dependent on how long the microscope has been exposed to ambient conditions, how humid the environment is, and contaminants such as fingerprints being introduced onto the microscope during assembly. It is best practice to keep the microscope under vacuum even if it is not being operated for faster pump downs in the future.

The radiofrequency (RF) generator is used to suppress laser noise, which can be seen in 9 figure 2.1. Note that RF bias modulation is standard in many optical systems, including CD, DVD, and Blu-ray systems. Internal reflections can arise throughout the fiber at different optical connections and lead to unwanted back reflection in the laser. These back reflections lead to laser amplitude noise, which lead to an increased interferometer noise floor. By reducing the laser coherence using RF bias modulation, these back reflected signals do not interact strongly with the laser cavity, thus stabilizing laser intensity and thereby minimizing interferometer noise. In order to optimize the amplitude and frequency of the RF signal input into the interferometer, we can monitor the root mean squared signal of the noise while adjusting the RF parameters. For the current configuration, we find that a frequency of 192 MHz at an amplitude of -5.0 dBm suppressed the most noise in the frequency shift

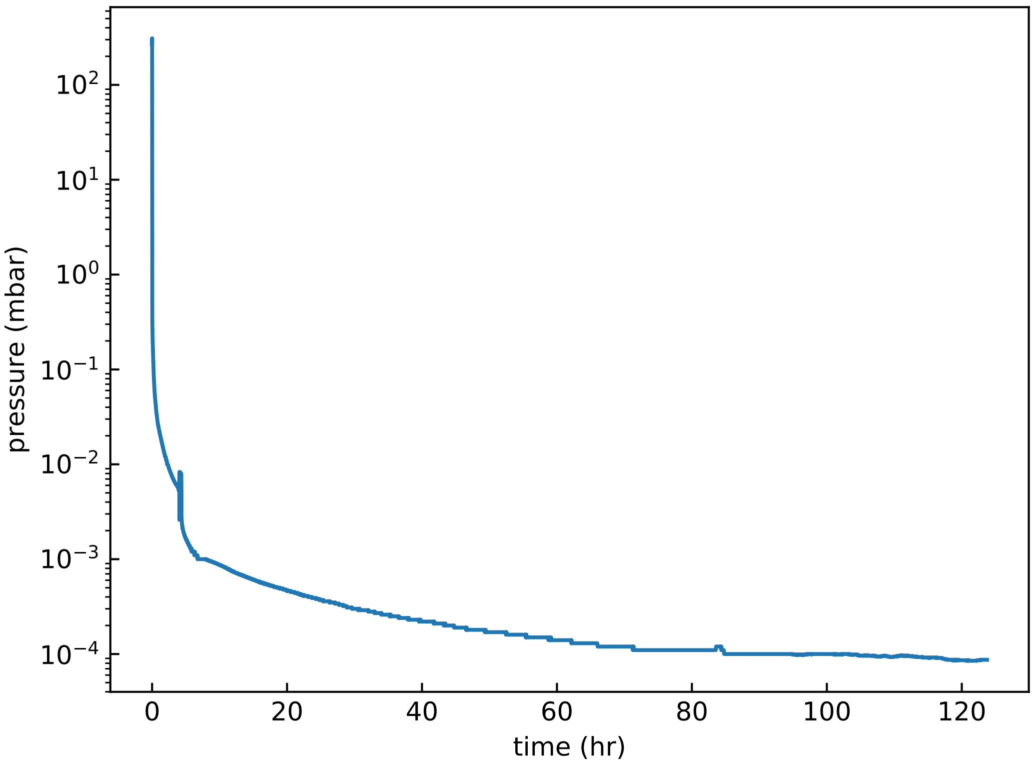

Figure 2.14: A typical pump down curve of our LT-AFM from ambient pressure and temperature to 8.5×10^{-5} mbar. The fluctuations around 4 hours between 10^{-3} and 10^{-4} mbar is the TPG controller switching between the Pirani gauge and cold cathode ionization gauge. Pressure on the order of 10^{-4} mbar is reached after 8 hours, while pressures of 10^{-5} take over 80 hours. The shoulder around 5 hours is characteristic of our system, and is likely related to cross over between pumping volume, pumping surface, and virtual leaks.

channel.

Dewar and Damping Platform

For preparing experiments, the microscope is hung above the preparation table, as is pictured in figure 2.1. This allows us easy access for assembling and disassembling the head for cantilever mounting and alignment, as well as sample mounting. In order to run experiments, the microscope head is closed with a vacuum canister sealed with 6mm indium wire. The indium wire is the ideal hermetic seal as it is easily compressible, doesn't damage the flanges of the vacuum canister, and is low-temperature and magnetic field compatible. Once the microscope is sealed, it is then lifted into the air via pully, slid along a ceiling-suspended rail, and ultimately lowered into the dewar. From this position, the microscope is connected to the turbopump.

The dewar is manufactured by Precision Cryogenic Systems and holds approximately 30 L of cryogenic liquids. It sits upon a vibration damping platform by Minus K Technology. This damping platform uses a passive mechanical vibration isolator which is able to dampen vibrations down to 0.5 Hz, eliminating the need for active dampeners that rely on electricity or compressed air canisters. The platform is tuned to a specific weight, which we can manually adjust as the mass of the dewar changes with the evaporation of our cryogenic liquid. The Dewar and damping platform are shown as 1 and 2 in figure 2.1.

Cooling Down

Before cooling the microscope, we make sure that we have achieved a high vacuum on the order of 10^{-4} mbar or better. Then, the microscope is overpressured to more than 1 atm with helium gas which is used for its heat transfer properties. It is important to make sure no voltage is on any of the electrodes, otherwise a potentially catastrophic plasma discharge will be ignited. Then, the cryogenic liquid is pumped from a low-pressure 100 L dewar into microscope dewar. Liquid nitrogen transfer takes approximately 1 to 2 hours, and we use approximately 35 L for one fill (5 L initially for colling down transfer line and dewar, and 30 L to fill).

While the microscope is cooling down, the interferometer signal is measured and observed in real-time. As the mechanical components of the microscope cool, they contract at different rates to the different thermal expansion coefficients of different materials. We observe that as the microscope cools down, the relative fiber-cantilever separation decreases. We observe this by seeing the interference fringes of the cavity. Cooling down from room temperature 290 K to liquid nitrogen temperature 77 K, the fiber will approach the cantilever $\tilde{1}30$ fringes, or approximately 100 μm. A typical cooldown interferometer curve is shown in figure 2.15. Once the desired microscope temperature is reached, we can pump down the microscope with the turbopump.

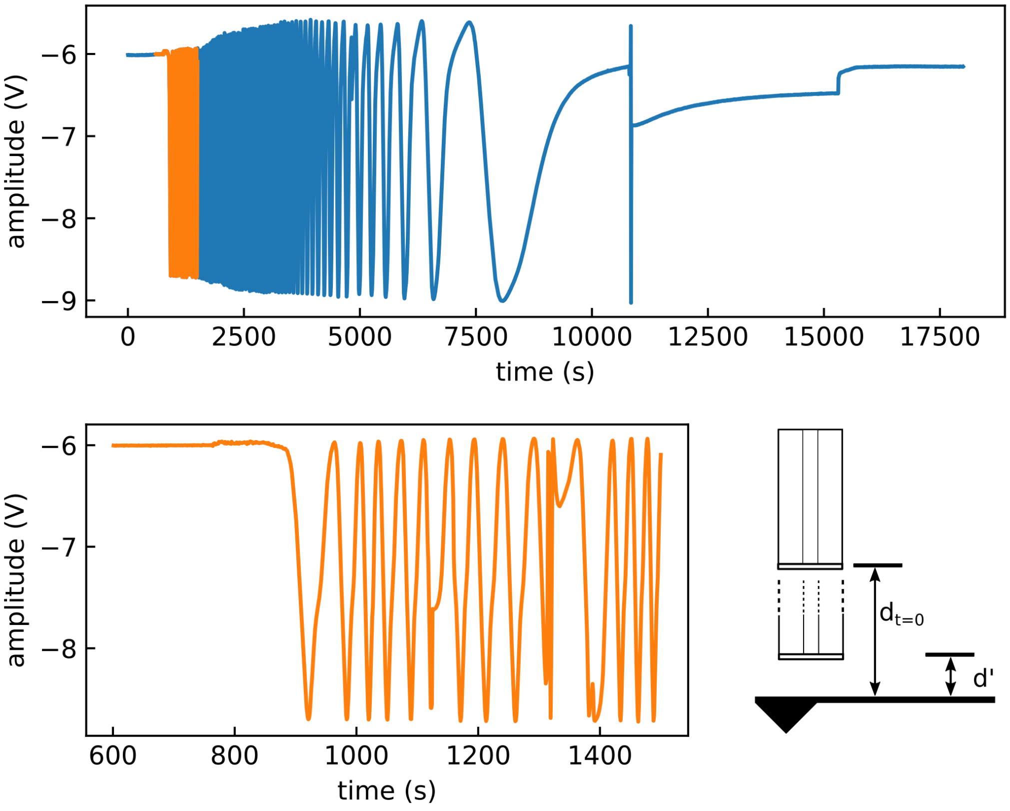

Figure 2.15: Top shows the interferometer detection signal as a function of time during a cool down from 290 K to 77 K. As the microscope cools down, the relative distance between the fiber and cantilever decreases, causing the fiber to approach approximately 100 microns. As you can see, we see smooth fringes until it eventually stabilizes once 77 K has been reached. The discontinuities at 11000 and 15500 secs are me manually moving the fiber to make sure contact between the fiber and cantilever wasn't made. The bottom shows a zoom-in of the beginning fringes when the microscope first begins to cool. Non-continuous jumps in the signal are likely a result of non-linearities in contracting.

2.1.2 AFM Software

The software used for controlling the microscope is detailed in this section. We briefly explain the role of each of them and the importance, and direct you to the source where you can download the software for yourself. Everything that is open-sourced will have a link to the repository. For our preferred workflow, we chose to use all command-line programs. However, this source code could be used to make a Python GUI program in a rather straight forward manner.

Digilent Controllers

The Digilent Analog Discovery 2 (DAD2) is very versatile, but we primarily use it for its analog I/O capabilities. We can use two simultaneously giving us 4 separate output and input channels at once, with two devices connected to the microscope computer via USB. There is a GUI software called Waveforms that gives you an interface to use the DAD2 as a digital oscilloscope. But for our purposes, we used the Waveforms Python API to control the inputs and outputs of the devices.

To move the piezo walkers, we send out a sawtooth waveform from the Digilent output, and in the four inputs, we will typically measure the interferometer detection signal, the interferometer excitation signal, the oscillation amplitude of the cantilever, and the phase. These channels are all outputs from the Zurich lockin, however, we can choose to acquire any DC signals we choose. Retracting the fiber walker 500 steps with a sawtooth waveform of frequency of 2000 Hz and amplitude of 1.5 V is as is done in the command line with:

```
./fiber_walker.py 2000 1.5 -500 y
```

This would yield a resulting plot as shown in the example in figure 2.16, and saves the data as CSVs for future manipulation.

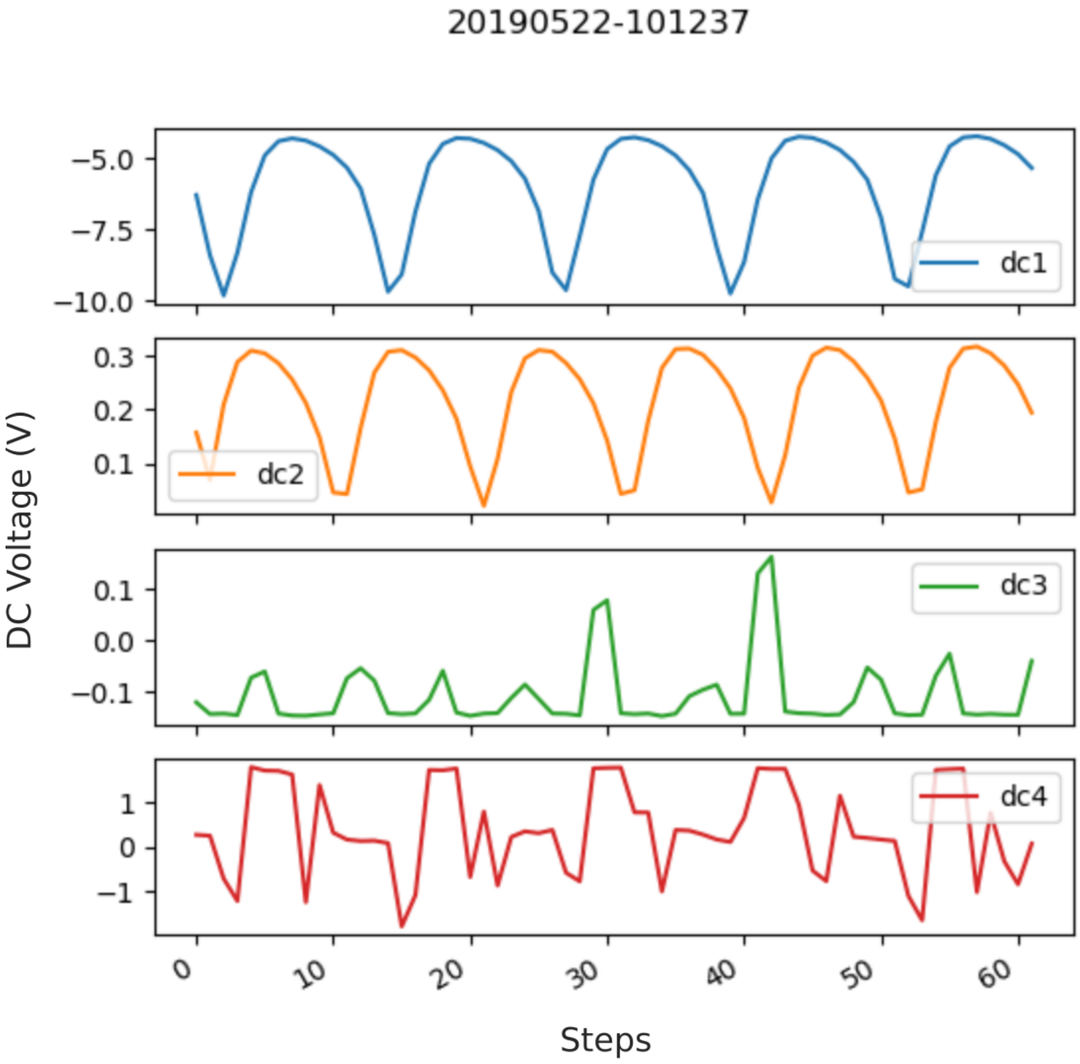

Figure 2.16: An example output plot showing the fiber walker moving 61 steps. This example follows the typical hardware configuration, with channels 1,2,3, and 4 being detection interferometer, excitation interferometer, cantilever oscillation amplitude, and phase.

Another useful program is to have the Digilent arbitrarily record a channel. This is useful for monitoring the interferometer signal over a extended period of time, which can be useful for measuring thermal drifts due to thermal fluctuations in the microscope. For example, we can record on channel 3 input of the Diglient until the user quits the program with the following command:

```
./analog_record.py 3
```

This would result in an output plot of the DC channel as a function of time that is updated in real time and records the data to a CSV for future manipulation. Further examples and source code can be found at https://github.com/harryturr/lt-afm-software-suite.

Zurich Instruments API

The Zurich Instruments lock-in amplifier is used in our experiments for characterizing the cantilever via frequency response sweeps and as a lock-in amplifier for our frequency shift measurements. The device is connected to the microscope computer via an ethernet connection. Zurich instruments provide a web GUI LabOne for interfacing with the hardware, but additionally, they support a Python API zhinst which provides communication between Zurich Instruments devices with via the Python programming language.

We used this package to develop command-line interface programs that can control almost all of the functionality of the microscope that we want. For example, recording a frequency sweep centered at 150 kHz spanning 4096 Hz with a bandwidth of 100 (as defined by Zurich Instruments) and 1024 data points is as simple as calling the following command from the terminal:

```
./sweeper.py sweep 150000 4096 1024 100
```

In addition to doing the frequency sweep, the quality factor is determined by taking the numerical derivative of the phase slope at resonance. The sample outputs of this program are shown in figures 2.17 and 2.18.

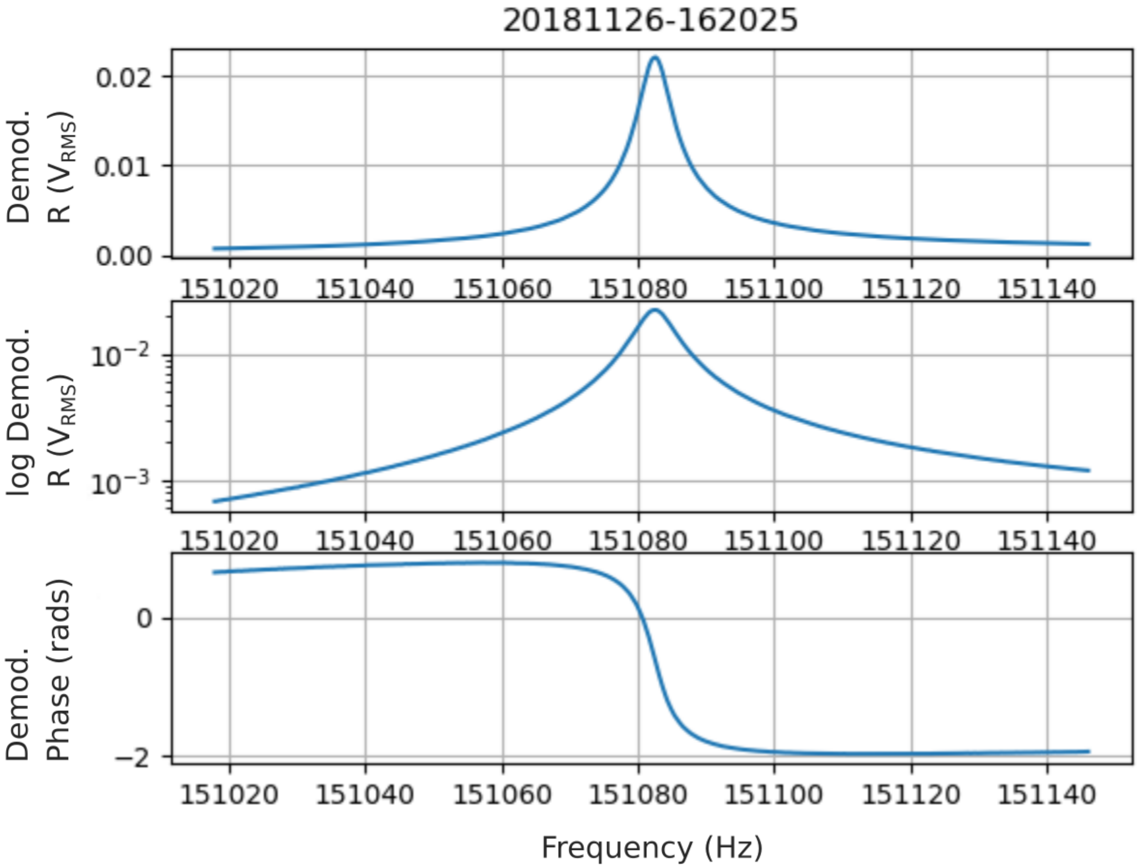

Figure 2.17: An example output plot showing the cantilever being swept at 77 K. We see that the resonance is at approximately 151082 Hz.

Further examples, source code, and more detailed information can be found at https://github.com/harryturr/lt-afm-software-suite.

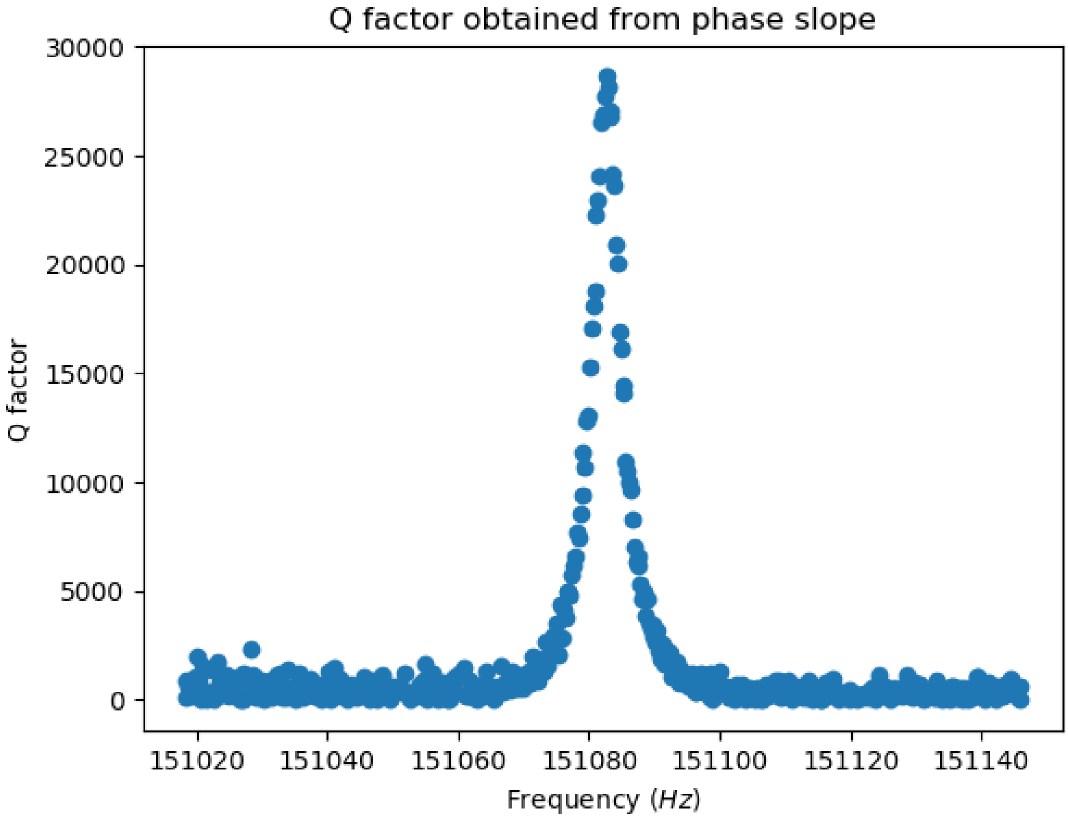

Figure 2.18: An example output plot showing the numerical derivative of the phase from the cantilever frequency sweep. The Q-factor is determined to be the derivative of the phase on resonance, which in this case is 28643.

TPG 300

The Total Pressure Gauge Controller (TPG 300) by Pfeiffer Vacuum is used for interfacing with Pirani and cold cathode gauges to read the pressure of the microscope. The TPG 300 is connected via serial port and allows communication in a variety of ways. For simple commands, we communicate with it via Telnet. However, for constant monitoring and real time updates and plots for the pressure, we have written a simple Matlab script to run in the background during experiments. Source code can be found at https://github.com/harryturr/lt-afm-software-suite and an example plot of the real-time pressure is shown in figure 2.14.

GXSM SPM Software

The Gnome X Scanning Microscopy project (GXSM) is a powerful open-source graphical interface that pairs with a DSP open-source controller. The GXSM software allows full control over any aspect of the experiment, offering the standard toolbox that most commercial controlling software has, with the added benefits of being able to fully customize and hack the software. With a fully integrated Python console, experiments become easily scriptable. Full source code, information, and manual are available at http://gxsm.sourceforge.net/.

3 | Manuscript

In order to perform NC-AFM experiments, the AFM cantilever needs to be constantly excited on its resonant frequency while the resulting frequency shift from interaction forces is measured and used as the set point. In single electron charging experiments, the signals we are interested in are very small and appear in the frequency shift and dissipation AFM channels. If we use a piezoelectric material for AFM cantilever excitation, we excite additional resonances in the microscope body which can create artifacts in the frequency shift and dissipation channels. This causes non-reliable operation of the microscope and makes it difficult to interpret our data from experiments.

For successful operation of our microscope in these very sensitive charging experiments of single molecules, we implemented a single fiber optical excitation and detection system for our cantilever, where we can simultaneously drive and measure the position of the cantilever using two different wavelengths of light.

In this work, I performed the experiments with YM and ARG, analyzed the data and prepared all figures excluding 2 and 4, developed the modeling of the cavity with YM, and wrote and prepared the manuscript for submission with YM and PG.

The manuscript has been submitted to the European Physics Journal of Techniques and Instrumentation and is currently under review. The preprint can be seen on the arXiv [17].

RESEARCH

Optical excitation of atomic force microscopy cantilever for accurate spectroscopic measurements

Yoichi Miyahara[1,2*], Harrisonn Griffin[1*], Antoine Roy-Gobeil[1], Ron Belyansky[1], Hadallia Bergeron[1], José Bustamante[1] and Peter Grutter[1]

Abstract

Reliable operation of frequency modulation mode atomic force microscopy (FM-AFM) depends on a clean resonance of an AFM cantilever. It is recognized that the spurious mechanical resonances which originate from various mechanical components in the microscope body are excited by a piezoelectric element that is intended for exciting the AFM cantilever oscillation and these spurious resonance modes cause the serious undesirable signal artifacts in both frequency shift and dissipation signals. We present an experimental setup to excite only the oscillation of the AFM cantilever in a fiber-optic interferometer system using optical excitation force. While the optical excitation force is provided by a separate laser light source with a different wavelength (excitation laser : $\lambda = 1310$ nm), the excitation laser light is still guided through the same single-mode optical fiber that guides the laser light (detection laser : $\lambda = 1550$ nm) used for the interferometric detection of the cantilever deflection. We present the details of the instrumentation and its performance. This setup allows us to eliminate the problems associated with the spurious mechanical resonances such as the apparent dissipation signal and the inaccuracy in the resonance frequency measurement.

Keywords: atomic force microscopy; fiber optic interferometer; optomechanical coupling

Full list of author information is available at the end of the article
[*] Equal contributor

Introduction

Reliable operation of frequency modulation mode atomic force microscopy (FM-AFM) depends on a clean resonance of an AFM cantilever. It is recognized that the spurious mechanical resonances originating from the various mechanical components of the microscope body are excited inadvertently by a piezoelectric element that is intended for exciting the AFM cantilever oscillation and these spurious resonances cause the serious undesirable signal artifacts in both frequency shift and dissipation signals [1, 2].

The additional frequency-dependent amplitude response causes a crosstalk between the dissipation and frequency shift signals, resulting in artifact signal in dissipation channel which misleads the interpretation of the tip-sample interaction physics. Although such dissipation artifacts could be corrected for by off-line signal processing [2], the additional frequency-dependent phase responses near the cantilever's resonance frequency can cause the deviation of the oscillation frequency from the cantilever's resonance frequency for the cantilevers with low quality (Q) factor case [1] which makes quantitative measurement of tip-sample interaction challenging. Even in the case of the high-Q cantilever, excessive amount of phase changes due to spurious resonances can cause an interruption of the self oscillation by breaking the phase matching condition, resulting in the loss of distance feedback signal. For this reason, it is important to develop a cantilever excitation scheme which can eliminate the excitation of the spurious mechanical resonances. While the optical excitation of AFM cantilever oscillation has been adopted mainly for the operation in liquid in which case the quality factor is strongly damped [3], it is also widely recognized that the effects of spurious resonances are important at low temperature in high vacuum environment [2] where the Q-factors of spurious resonances are enhanced substantially. Here we report an experimental setup for optical AFM cantilever excitation based on an all fiber optic interferometer which is commonly used for low-temperature AFM systems [4]. As this setup requires only one optical fiber which is used for both sensing and actuation, it can be easily adopted to the existing AFMs which employ fiber-optic interferometers.

Experimental

Figure 1 shows a diagram of the optical setup. In this setup, two separate laser lights with different wavelengths are used for the detection (Laser diode 1, 1550 nm DFB laser with an optical isolater, NECSEL) and excitation (Laser diode 2, 1310 nm, LPS-1310-FC, Thorlabs) of the AFM cantilever oscillation. The excitation and detection laser lights are combined with a filter wavelength division multiplexer (FWDM, FWDM-1513, AFW Technology) and launched into a single-mode optical fiber (SMF-28e) [5]. The reflected light from the fiber end and cantilever interfere each other and go back the same FWDM. Only the detection laser light can pass the FWDM and reach a photodiode via an optical circulator (CIR-3-15, AFW Technology) [6]. The intensity of the excitation laser is modulated by modulating the drive current with a power combiner (PRSC-2050, Mini Circuits). The drive current for the detection laser is modulated by a radio frequency signal (several hundred MHz) to suppress stray interferences [7].

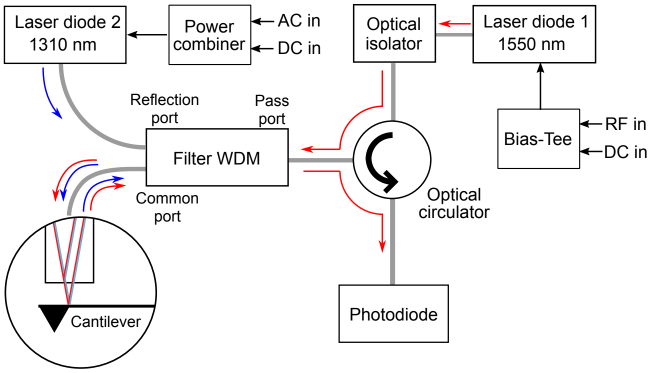

Figure 1 Schematic diagram of the experimental setup. Two laser lights from Laser diode 1 (1550 nm) and Laser diode 2 (1310 nm) are combined with a filter Wavelength Division Multiplexer (FWDM). The combined light is launched into a single-mode optical fiber. While a fraction of the light is reflected at the fiber-vacuum interface, the rest of the light which comes out of the fiber is reflected on the back side of the cantilever and goes back into the fiber. Only the 1550 nm laser can pass through the filter WDM and reach the photo diode.

We coated the cleaved optical fiber end to increase the back reflection to improve the detection sensitivity of the interferometer [8]. The TiO_2 solution used for fiber coating was prepared using a solution of titanium-(IV)-2-ethylhexoxide (Sigma-Aldrich) diluted with xylene. The cleaved fiber end was dipped 1 cm into the solution, then passed through a propane torch for less than one second for flash annealing. Optimal flash parameters, such as placement of fiber in the flame and time in flame were determined via trial and error. The reflectivity of the fiber was monitored in real time with a photodiode back reflection set up. Successfully annealed fibers would typically have reflectivity between 20 - 30%, with the best fibers having up to 35%. Examples of successfully coated fibers are shown in Fig 2.

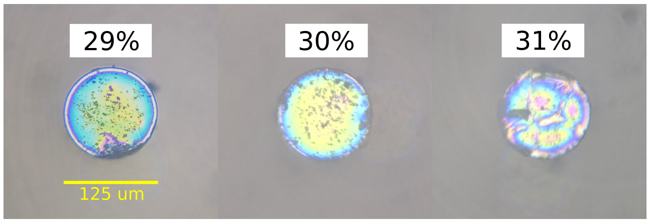

Figure 2 Three example fibers showing the reflective titanium dioxide coating with varying back reflectance. The fiber has a core diameter of 8 μm with a fiber cladding of 125 μm radius.

Characterizing optical cavity

The home built low temperature AFM uses a Fabry-Perot interferometer (FPI) in reflective mode to precisely and accurately measure the distance between the end of the optical fiber and the reflective aluminum coating of the AFM cantilever. An FPI is an optical cavity which is made with two parallel semi-reflective mirrors (mirror 1 and 2) with reflectances R_1 and R_2, separated by a cavity length d. In our case, the coated fiber and cantilever are the mirror 1 and 2, respectively, and the cavity medium is vacuum. The coated fiber is aligned to the tip end of the cantilever to maximize the deflection measurement sensitivity. Incident light from the detection laser travels down the fiber, where some of the light is internally reflected off of the fiber end, and the rest is injected into the FPI. This light is reflected off of the cantilever where it is then reflected multiple times between the two mirrors of the cavity before ultimately reentering the optical fiber. The reentered light is guided through the fiber, WDM, and circulator and its intensity, I_r, is measured by the photodiode (Fig. 1). The FPI lends itself to being more sensitive than other interferometers because of the multiple reflections between the mirror 1 and 2 when the separation between the mirrors is small enough [9, 10, 11]. It is important to notice that the multiple reflection also plays an important role for the excitation laser light as it enhances the optical force. We use the FPI model reported in Ref. [12] for the following analysis.

The ratio of the intracavity intensity, I_{circ}, to the intensity incident upon mirror 1 , I_{inc}, (enhancement factor, A'_{circ}) is given by Airy distribution,

$$A'_{\mathrm{circ}} = \frac{I_{\mathrm{circ}}}{I_{\mathrm{inc}}} = \frac{1-R_1}{(1-\sqrt{R_1R_2})^2 + 4\sqrt{R_1R_2}\sin^2\phi}. \tag{1}$$

where ϕ is the single-pass phase shift between the mirrors and can be expressed as

$$\phi = \frac{2\pi d}{\lambda} \tag{2}$$

where d is the distance between two mirrors (cavity length) and λ is wavelength. Similarly, the enhancement factor for the total back reflected light with respect to I_{inc} is given by

$$\frac{I_{\mathrm{refl}}}{I_{\mathrm{inc}}} = \frac{(\sqrt{R_1}-\sqrt{R_2})^2 + 4\sqrt{R_1R_2}\sin^2\phi}{(1-\sqrt{R_1R_2})^2 + 4\sqrt{R_1R_2}\sin^2\phi}. \tag{3}$$

Figure 3(a) shows the experimentally measured interference fringe and theoretical one given by Eq. 3 assuming $R_1 = 0.33$ and $R_2 = 0.96$. These values are in good agreement with the value obtained from the measured back reflection of the coated fiber ($R_1 = 0.30$) and the reflectance of the Al coated cantilever $R_2 = 0.96$ assuming 100% collection of the reflected beam from the cantilever. The good agreement between the theory and experiment confirms the validity of the model. For $R_1 = 0.33$ and $R_2 = 0.96$, the enhancement factor, A'_{circ} is found to be 3.5.

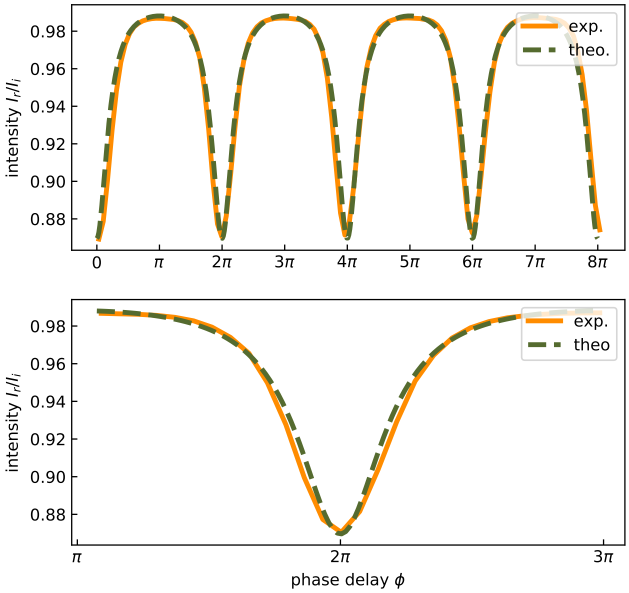

Figure 3 Theoretical and experimental transfer function of the reflective mode of the Fabry-Perot interferometer. **Top** shows the measured and theoretical interference response of the cavity as a function of increasing phase delay (i.e. increasing fiber-cantilever separation). This fiber end has a 30% back reflection. **Bottom** shows the first full interference peak that occurs as peak intensity as a function of phase delay. The experimental data is plotted with the theoretical fit.

Results

Figure 4 shows the frequency responses of an AFM cantilever (NCLR Nanosensors, Al backside coated and Pt tip-side coated) excited by piezo excitation (red line) and optical excitation (blue line). The response by piezo excitation shows spurious resonance modes around the cantilever's fundamental resonance frequency. These additional frequency-dependent amplitude responses are not present when the cantilever is optically driven. The optical force does not excite the various mechanical resonances of the microscope body, thus giving us cleaner signals in the frequency shift and dissipation channels. Through removing the artifacts, we can better study the tip-sample interaction physics.

Quantifying optical excitation force

In order to determine the magnitude of the optical force quantitatively, we use the following relation between the oscillation amplitude and the amplitude of the excitation optical force when the cantilever is excited by harmonic excitation force, $F(t) = F_{\mathrm{opt}} \sin(2\pi f_0 t)$, at the resonance frequency, f_0:

$$A = \frac{Q}{k} F_{\mathrm{opt}}. \tag{4}$$

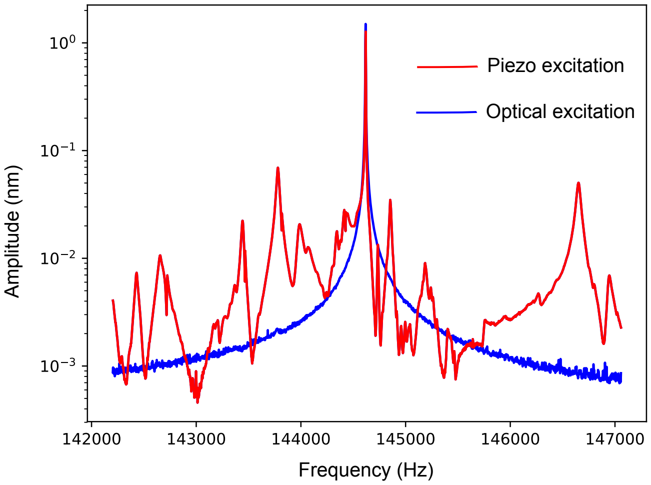

Figure 4 Amplitude frequency response of the AFM cantilever excited by piezo excitation (red) and optical excitation (blue) measured at 4.5 K. Note the spurious mechanical resonances in the piezo excitation which arise from vibrations in the microscope body.

Here A is the amplitude of the oscillation, Q the quality factor, k the spring constant of the cantilever and F_{opt} the amplitude of the oscillating optical force, We used the Sader method to calibrate the effective spring constant of the fundamental flexural mode of cantilevers [13] and obtained a spring constant $k = 19$ N/m for the cantilever used.

In our interferometer setup, the fiber-cantilever distance can be adjusted by a piezoelectric stick-slip motor with the step size as small as 20 nm. The step size is confirmed to be very uniform over several fringes. As we change the fiber-cantilever distance by stepping the fiber position, we record the signal at the photodiode V_{PD}. The resulting interference fringes show nearly periodic peaks and the peak separation, known to be $\lambda/2$ from Eq. 3. This well-defined separation allows us to calibrate the horizontal axis that determine the sensitivity of the interferometer.

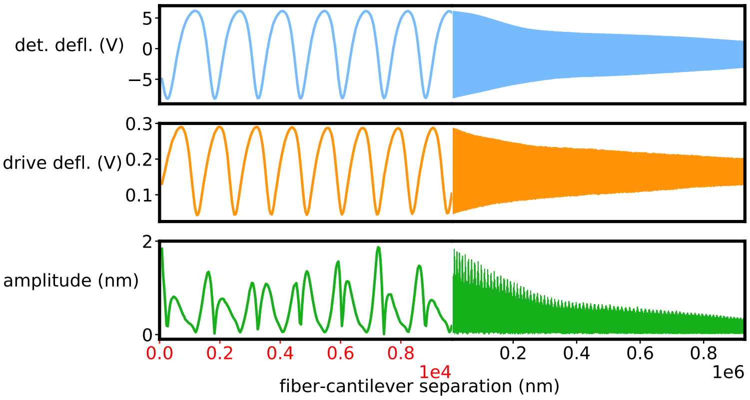

Figure 5 Interference fringes of detection (1550 nm) (cyan) and excitation (1310 nm) (orange) lasers as a function of fiber-cantilever separation measured at 77 K in vacuum of 10^{-5} mbar.

The interferometer sensitivity S is calculated as the derivative of the measured interferometer output voltage V_{PD} with respect to the fiber fiber-cantilever distance z [14]: Since the distance between successive peaks is known, we can convert the walker steps Δz into a distance by identifying successive peak positions and counting the steps between them. Now we can simply take the derivative of the photodiode signal versus the fiber-cantilever distance, then divide by the walker step Δz to obtain the sensitivity S. An example of such measurement is shown in Fig. 6. With the known sensitivity in units of V/nm, it is straightforward to determine the oscillation amplitude of the cantilever. We measure the ac component of the photodiode signal V_{PD}, and convert its amplitude in Volt to the amplitude in nm by dividing V_{PD} by the sensitivity S. The typical sensitivity during the experiments is 30 mV/nm. This sensitivity can also be used to calculate the detection noise of the interferometer. By taking a power spectral density of V_{PD} around the cantilever resonance, we can convert the measured interferometer noise in $\mathrm{V}/\sqrt{\mathrm{Hz}}$ into the detection noise in $\mathrm{fm}/\sqrt{\mathrm{Hz}}$. A typical detection noise at 77 K is $\approx 50\ \mathrm{fm}/\sqrt{\mathrm{Hz}}$ and at 4 K is $\approx 15\ \mathrm{fm}/\sqrt{\mathrm{Hz}}$. The best detection noise we have observed at 4 K is $7\ \mathrm{fm}/\sqrt{\mathrm{Hz}}$.

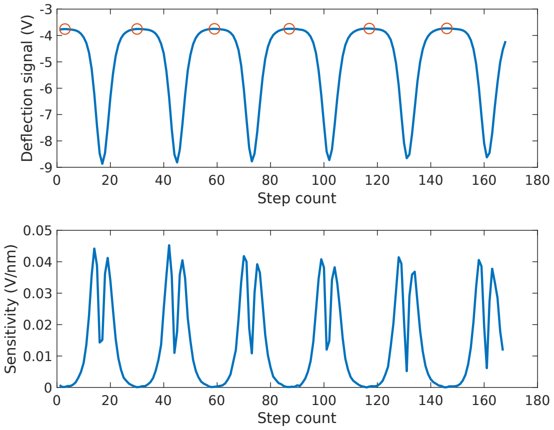

Figure 6 **Top** shows the photodiode signal as a function of the number of fiber walker steps as it is retracted from the cantilever. Peaks are indicated via circles, which are then used to determine the number of steps between adjacent fringes. **Bottom** shows sensitivity S which is calculated by taking the derivative of the photodiode signal and dividing by the average step size between fringes.

From the measured A, Q and k, we are able to obtain the optical excitation force, F_{opt} as a function of the amplitude of the modulated optical power by using Eq. 4, as shown on the right hand side axis of Fig. 7. We measured the optical power of the 1310 nm driving laser with a separate photodiode placed at the 10 % branch of a 90/10 coupler (not shown in Fig. 1) and its modulated amplitude, P, with the lock-in amplifier. Figure 7 shows the measured A-P relations with four different dc offset current settings. We can see that the oscillation amplitude is just dependent on the amplitude of modulated optical power and does not depend on the dc power. The average slope of the four data sets is 68.4 pN/mW.

Now let us compare the measured driving force with the theoretical optical forces. The theoretical optical scattering force (radiation pressure force), F_{scat}, acting on the AFM cantilever with reflectance R_2 in a FPI system is given by

$$F_{\mathrm{scat}} = \frac{2P_{\mathrm{circ}}R_2}{c} = \frac{2A'_{\mathrm{circ}}P_{\mathrm{inc}}R_2}{c} \qquad (5)$$

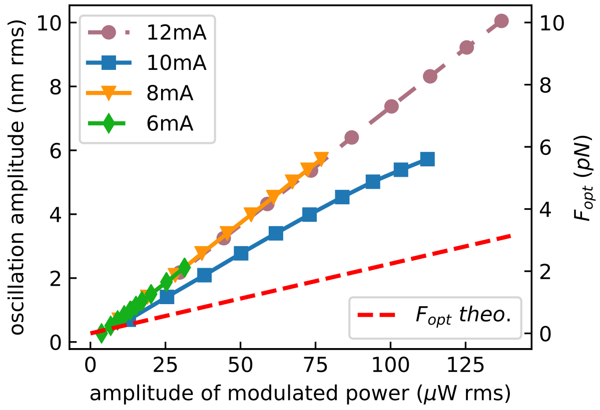

Figure 7 Cantilever oscillation amplitude as a function of modulation power at varying laser diode currents.

where $P_{\rm circ}$ is the optical power in the FPI cavity, $P_{\rm inc}$ the incident optical power and c the speed of light. While the enhancement factor $A'_{\rm circ}$ is in general dependent on the wavelength due to the wavelength-dependence of R_2, we confirmed $A'_{\rm circ} = 3.5$ for the excitation laser ($\lambda = 1330$ nm) by measuring the interferometer fringes as shown in Fig. 5. The theoretical slope of $F_{\rm scat} - P_{\rm inc}$ is therefore $F_{\rm scat}/P_{\rm inc} = 22.4$ pN/mW for $A'_{\rm circ} = 3.5$ and $R_2 = 0.96$. The fact that the experimental optical force $F_{\rm opt}$ is much larger than the expected optical scattering force $F_{\rm scat}$ indicates that the photothermal (bolometric) effect plays an important role [9].

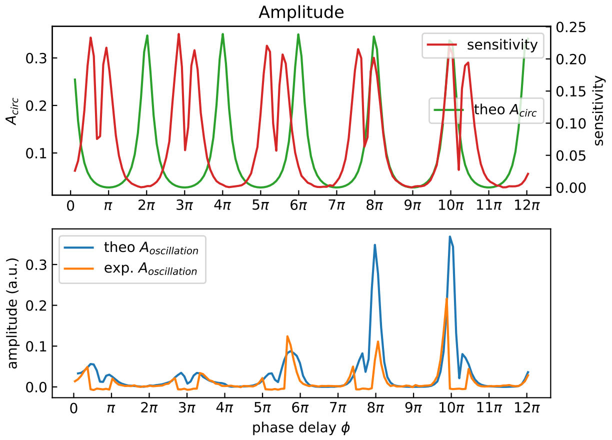

Figure 8 **Top** shows the theoretical $A'_{\rm circ}$ and the sensitivity S for a set of interference fringes. **Bottom** shows the theoretical and experimentally measured oscillation amplitude of the cantilever as a function of phase delay (cavity length). The theoretical amplitude was calculated by multiplying circulating enhancement factor $A'_{\rm circ}$ by sensitivity S.

Effect of optical driving force on frequency shift noise

In FM-AFM, the interaction forces between the sample and cantilever are detected as a frequency shift. Since the tip-sample distance is regulated by the frequency shift, a reduction in frequency shift noise will lead to high-resolution FM-AFM images. Additionally, in electrostatic force microscopy with single-electron sensitivity (e-EFM) measurements, achieving a detectable signal is only possible with a reduced frequency shift noise [14, 15]. In the following we will investigate if optically driving the cantilever introduces additional frequency noise. The frequency shift noise measurements were performed at 77 K with the AFM cantilevers that have spring constants of $k = 20$ N/m and quality factors at 77 K varying between 15,000 and 50,000. In these experiments, the cantilever is self-excited at its resonant frequency by feeding the deflection signal into the optical excitation system through an oscillation control electronics (easyPLLplus controller, Nanosurf) which consists of a phase shifter and amplitude controller [16].

To see if the average power of the excitation source affected the frequency shift noise of the microscope, we measured the frequency shift noise at various oscillation amplitudes from 0.5 to 10 nm, and increased the average optical power of the excitation laser. The amplitude was kept constant at different average optical powers. The frequency shift measurement was made using a phase-locked loop (PLL) frequency detector (HF2LI with PLL option, Zurich Instruments) with a detection bandwidth of 100 Hz. The frequency shift noise was measured using the root mean square value of the frequency shift and is shown in Fig. 9. As expected from the theory [16], the frequency shift noise increases with decreasing oscillation amplitude, but there is no significant variation in the frequency shift noise at the same oscillation amplitude for varying average optical excitation power.

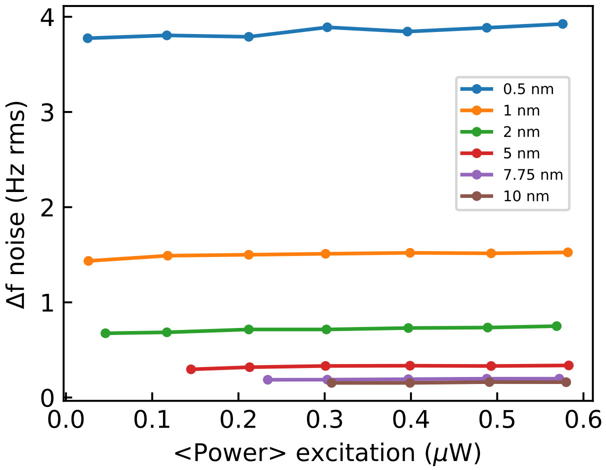

Figure 9 Frequency shift noise as a function of average optical power of the excitation laser at varying oscillation amplitudes. The frequency shift noise was measured as the root mean square (RMS) of the frequency shift from the lock-in amplifier.

Since we can precisely adjust our fiber-cantilever separation distance, we are able to choose an operating position on an interference fringe arbitrarily. Typically, we choose a fringe position that maximizes the sensitivity. On a single fringe, we could choose the operating position either on the negative or positive slope side of the fringe. It has been reported that the effective Q-factor is decreased or increased depending on the slope of the interferometer signal due to the optomechanical coupling [9, 17, 18]. For example, by adjusting the fiber-cantilever cavity position to be on either side of a single fringe at the same deflection DC value, we observe the effective Q-factors at the negative and positive slope side to vary as much as 3000.

To determine if the different effective Q-factor at the negative and positive slope affect the frequency shift noise, we measured the frequency shift noise at various oscillation amplitudes on both the negative and positive slope side of the fringe at the same DC deflection values, as shown in Fig. 10. The results shows negligible difference in frequency shift noise between the negative slope and positive slope side of the fringe.

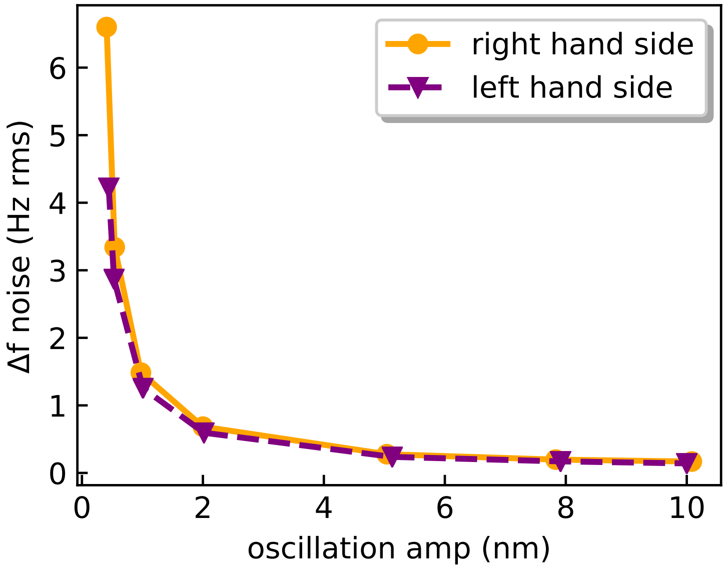

Figure 10 Frequency shift noise as a function of oscillation amplitude of cantilever being driven via optical excitation at 77 K.

Conclusion

In conclusion, we have integrated an optical drive cantilever excitation system into our low temperature AFM in a non-invasive way. By using the optical circuit as shown in Fig. 1, we are able to have a two laser detection and excitation system deployed through a single optical fiber. The optical drive reduces spurious mechanical resonances making the AFM suitable to study sensitive tip-sample physics without artifacts from crosstalk in the frequency shift and dissipation channels. The setup can easily be adopted for the existing AFMs which use fiber-optic interferometer.

Competing interests

The authors declare that they have no competing interests.

Author's contributions

YM designed and constructed the experimental setup. YM, HG, ARG and JB performed the experiments. YM, HG and ARG analyzed the data. RB and HB contributed to the preliminary experiments. YM and PG conceived of the study. YM, HG and PG wrote the manuscript All authors read and approved the final manuscript.

Acknowledgements

Financial support from The Natural Sciences and Engineering Research Council of Canada and Le Fonds de Recherche du Québec—Nature et Technologies are gratefully acknowledged.

Additional information

Correspondence and requests for materials should be addressed to YM (yoichi.miyahara@txstate.edu) or PG (peter.grutter@mcgill.ca).

Author details

[1]Department of Physics, McGill University, 3600 rue University, H3A 2T8 Montreal, Canada. [2]Department of Physics, Texas State University, 601 University Drive, 78666 San Marcos, USA.

References

1. Kobayashi, K., Yamada, H., Matsushige, K.: Reduction of frequency noise and frequency shift by phase shifting elements in frequency modulation atomic force microscopy. Review of Scientific Instruments **82**(3), 033702 (2011). doi:10.1063/1.3557416
2. Labuda, A., Miyahara, Y., Cockins, L., Grutter, P.H.: Decoupling conservative and dissipative forces in frequency modulation atomic force microscopy. Physical Review B **84**(12), 125433 (2011). doi:10.1103/PhysRevB.84.125433
3. Labuda, A., Kobayashi, K., Miyahara, Y., Grütter, P.: Retrofitting an atomic force microscope with photothermal excitation for a clean cantilever response in low Q environments. Review of Scientific Instruments **83**(May), 053703 (2012). doi:10.1063/1.4712286
4. Rugar, D., Mamin, H.J., Guethner, P.: Improved fiber-optic interferometer for atomic force microscopy. Applied Physics Letters **55**(25), 2588–2590 (1989). doi:10.1063/1.101987
5. Weld, D.M., Kapitulnik, A.: Feedback control and characterization of a microcantilever using optical radiation pressure. Applied Physics Letters **89**(16), 164102 (2006). doi:10.1063/1.2362598
6. Rasool, H.I., Wilkinson, P.R., Stieg, A.Z., Gimzewski, J.K.: A low noise all-fiber interferometer for high resolution frequency modulated atomic force microscopy imaging in liquids. Review of Scientific Instruments **81**(2), 023703 (2010). doi:10.1063/1.3297901
7. Smith, D.T., Pratt, J.R., Howard, L.P.: A fiber-optic interferometer with subpicometer resolution for dc and low-frequency displacement measurement. Review of Scientific Instruments **80**(3), 035105 (2009). doi:10.1063/1.3097187
8. Subba-Rao, V., Sudakar, C., Esmacher, J., Pantea, M., Naik, R., Hoffmann, P.M.: Improving a high-resolution fiber-optic interferometer through deposition of a TiO2 reflective coating by simple dip-coating. Review of Scientific Instruments **80**(11), 115104 (2009). doi:10.1063/1.3244088
9. Vogel, M., Mooser, C., Karrai, K., Warburton, R.J.: Optically tunable mechanics of microlevers. Applied Physics Letters **83**(7), 1337–1339 (2003). doi:10.1063/1.1600513
10. Wilkinson, P.R., Pratt, J.R.: Analytical model for low finesse, external cavity, fiber Fabry–Perot interferometers including multiple reflections and angular misalignment. Applied Optics **50**(23), 4671 (2011). doi:10.1364/AO.50.004671
11. Von Schmidsfeld, A., Reichling, M.: Controlling the opto-mechanics of a cantilever in an interferometer via cavity loss. Applied Physics Letters **107**(12), 2–7 (2015). doi:10.1063/1.4931702
12. Ismail, N., Kores, C.C., Geskus, D., Pollnau, M.: Fabry-Pérot resonator: spectral line shapes, generic and related Airy distributions, linewidths, finesses, and performance at low or frequency-dependent reflectivity. Optics Express **24**(15), 16366 (2016). doi:10.1364/OE.24.016366
13. Sader, J.E., Chon, J.W., Mulvaney, P.: Calibration of rectangular atomic force microscope cantilevers. Review of scientific instruments **70**(10), 3967–3969 (1999)
14. Roy-Gobeil, A.: Single-electron charging using atomic force microscopy. PhD thesis, McGill University (2017)
15. Roy-Gobeil, A., Miyahara, Y., Bevan, K.H., Grutter, P.: Fully Quantized Electron Transfer Observed in a Single Redox Molecule at a Metal Interface. Nano Letters **19**(9), 6104–6108 (2019). doi:10.1021/acs.nanolett.9b02032
16. Albrecht, T.R., Grütter, P., Horne, D., Rugar, D.: Frequency modulation detection using high- Q cantilevers for enhanced force microscope sensitivity. Journal of Applied Physics **69**(2), 668–673 (1991). doi:10.1063/1.347347
17. Hölscher, H., Milde, P., Zerweck, U., Eng, L.M., Hoffmann, R.: The effective quality factor at low temperatures in dynamic force microscopes with Fabry–Pérot interferometer detection. Applied Physics Letters **94**(22), 223514 (2009). doi:10.1063/1.3149700
18. Tröger, L., Reichling, M.: Quantification of antagonistic optomechanical forces in an interferometric detection system for dynamic force microscopy. Applied Physics Letters **97**(21), 213105 (2010). doi:10.1063/1.3509412

4 | Sample Preparation

For the experiments conducted in this thesis, the samples that were primarily studied were self-assembled monolayers (SAMs) of ferrocene-terminated alkanethiols. When a fresh gold substrate is exposed to alkanethiols, they spontaneously adsorb from the liquid or gas phase [18]. The eventual NC-AFM measurements we perform are done at constant height mode by disabling feedback to the tip. We perform constant height measurements to reduce the measurement noise since feedback introduces additional noise into the measurement. Since our tip will only be on the order of nanometers away from the surface, any variation in sample topography can cause a tip crash with feedback disabled. Therefore, we want our samples to be as flat as possible.

To grow flat SAMs samples, it is essential to be able to have an atomically flat gold substrate for which the alkanethiols will adsorb. We achieve this by employing a method of making gold known as Template Stripping [19, 20, 21, 22]. Template Stripped Gold (TSG) provides us with a flat surface that has the added benefit of not being exposed to the atmosphere until a sample is needed and cleaved.

4.1 Template Stripped Gold

4.1.1 Direct Evaporation on Silicon Wafer

The TSG is prepared on a 4 inch polished silicon wafer. We use undoped 500 micron thick silicon wafers with 100 orientation from University Wafer, although any polished wafer should suffice. Ultraflat wafers are recommended, although they were not used in this study.

This silicon wafer is cleaned in a solution of 1:1 ethanol to chloroform. The wafer is put in a glass container containing enough solution to generously cover the wafer. It is heated on a hot plate and allowed to lightly boil for two minutes. After the boil, the wafer is ultrasonicated in the same solution for 10 minutes. Finally, the wafer is blown dry with pressurized Nitrogen gas and is ready to be loaded into the vacuum chamber for gold evaporation.

The evaporator we used for this study is the Thermionics Vacuum Products model VE-90, and can be seen in figure 4.1. This system has an integrated Inficon XTC/2 from Leybold quartz crystal deposition controller.

The vacuum chamber is kept under vacuum when not in use, thus allowing a quicker pump down time for experiments. The chamber is vented with nitrogen, and the cleaned silicon wafer is mounted and hung inverted at the top of the vacuum chamber. Bulk gold with purity of 99.99% is added into the trough, and the chamber is sealed and pumped down to a pressure of 8.5×10^{-7} mbar using a turbo diffusion pump.

Once this pressure is reached, a current is applied to the metal boat containing the bulk gold and is slowly ramped up until we achieve evaporation, typically around 120 A heating current. The gold is vaporized generating a vapor pressure in the chamber. The evaporated gold traverses the chamber in a vapor stream, and hits the silicon wafer substrate, sticking to it creating the film. This process is illustrated in figure 4.1. Note, the shutter is kept closed when evaporation begins to ensure that unwanted contaminants initially coming off of the evaporation boat do not deposit on the sample. When ready for deposition onto the substrate, the shutter is opened. We can increase our current to increase the deposition rate. We evaporate at 1 Angstrom/second which typically occurs around 160 A heating current. The wafer is constantly rotated during the deposition to ensure a more evenly distributed and uniform coating of gold. After deposition, the wafer is left under a high vacuum to cool to room temperature.

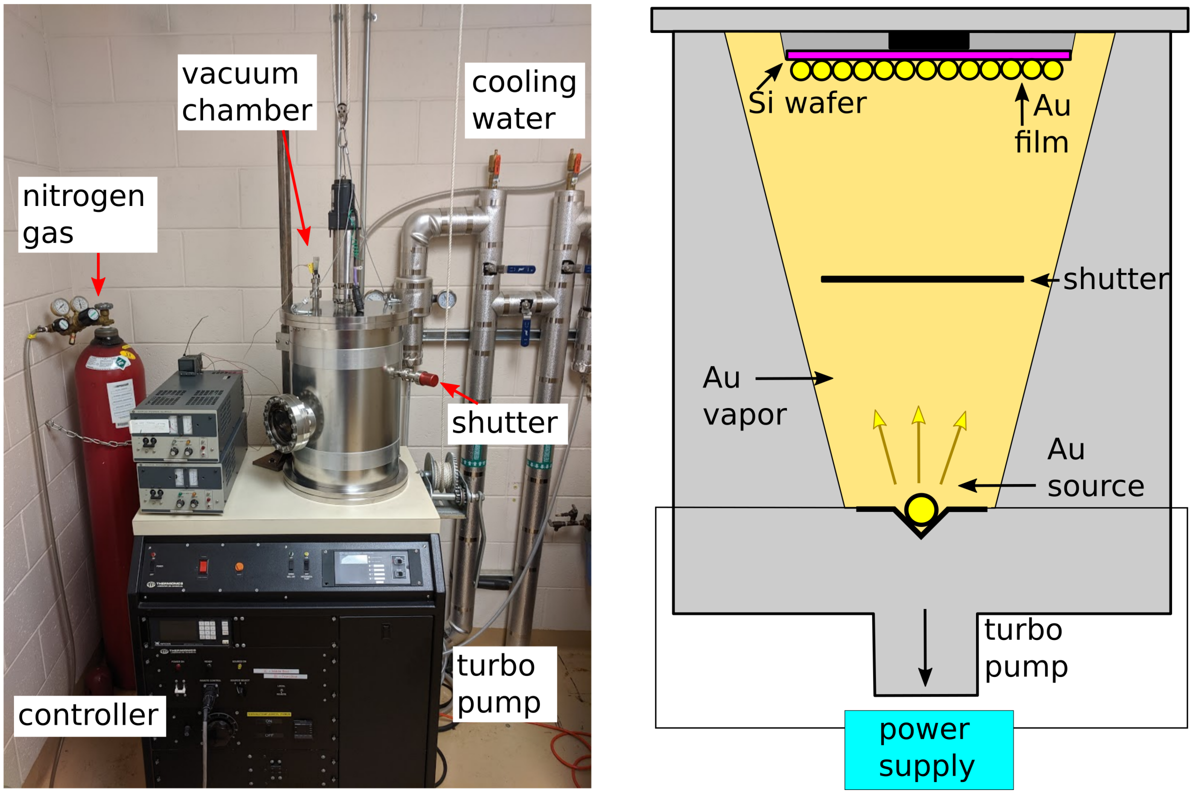

Figure 4.1: The gold evaporator used for gold deposition onto the silicon wafer. The wafer is hung inverted at the top of the vacuum chamber and the gold is evaporated at the bottom of the chamber. The evaporation is done at a pressure of 8.5×10^{-7} mbar.

4.1.2 Template Stripping Gold

Template stripping gold uses the bottom of the gold film, that is the gold that is touching the surface substrate, instead of the top of the gold that was lastly deposited during the evaporation. To strip the gold off of the silicon substrate, we need to attach support structures to the top. Since different sized samples were needed for AFM measurements and electrochemistry measurements, two different support structures were used. For AFM samples, another silicon wafer was diced into small chips (3mm by 8mm) using a commercial microfabrication wafer dicer. The chips were cleaned via ultrasonication in a solution of 1:1 acetone to isopropanol for 10 minute, then blown dry with a strong stream of nitrogen gas. For the electrochemistry samples, a glass slide was cut using a glass diamond cutter (12.5 mm by 22 mm), and were cleaned in the same process as described above.

For attaching the silicon chips, approximately 1 μL of Epotek 377 epoxy was dropped on to the gold surface via micropipette, and the cleaned silicon chip was gently placed on top, with the polished side making contact with the epoxy. For the glass slides, three drops of approximately 2 μL of Epotek 377 each were deposited on the surface via micropipette, with the three drops spanning the approximate length of the glass slide. The slide was then placed over the drops at an angle and slowly lowered onto the epoxy. A gold deposited wafer is shown in figure 4.2 with chips and slides being glued to it. The wafer is baked at 150°C for one hour to allow the epoxy to cure. The same wafer post-cure is shown in figure 4.2 b. A typical yield on a 4 inch wafer is approximately 100 small chips.

Care was taken to ensure that too much epoxy was not used. If there was excess, the epoxy would flow out from under the slides and chips and bridge to other slides and chips. If samples are connected via epoxy, it is nearly impossible to separate them when stripping.

To template strip the gold, a razor blade is used to gently scrape the edges of an adhered chip and apply some force to a chip corner to have the Si/epoxy/Au sample pop off of the substrate. The gold preparation and template stripping procedure can be seen in figure 4.3. The transferred gold samples were then imaged with a Multimode Nanoscope III AFM in tapping mode to measure the surface roughness and topography, as shown in figure 4.4.

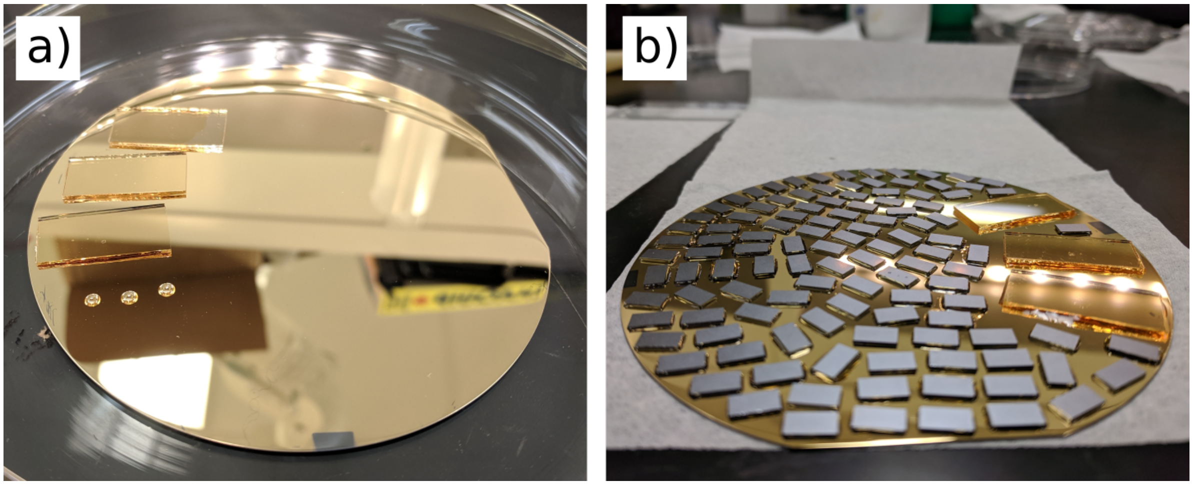

Figure 4.2: a) The wafer with a fresh deposition of 50 nm of gold and several cut glass slides being glued onto the surface. These glass slides are adhered with epoxy and will be used for electrochemistry measurements. b) The same wafer but with more slides and silicon chips. The chips are also adhered with epoxy and will be used for the AFM measurements.

To quantify the roughness, we use the root mean squared of the topography deviation. We calculate the roughness as being $R_q = \sqrt{\frac{1}{n}\sum_{i=1}^{n} {y_i}^2}$. Looking at a 5 μm by 5 μm area and 1 μm by 1 μm area, we observe roughness of $R_q = 1.14$ nm and $R_q = 1.03$ nm respectively. Typical samples are approximately $R_q = 1$ nm, but we can achieve template stripped gold with sub-nanometer root mean square roughness.

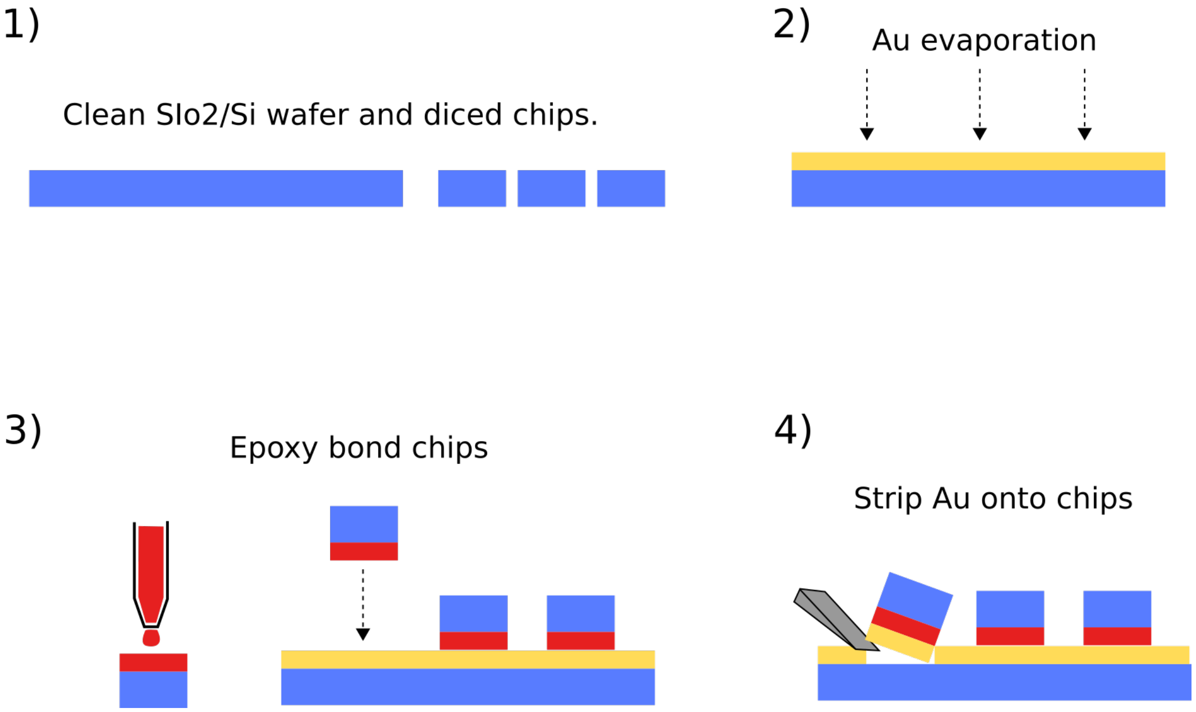

Figure 4.3: This cartoon shows the steps used for the preparation of template stripped gold from a bare silicon wafer. A cleaned silicon wafer has 50 nm of gold deposited via thermal evaporation. Then support chips are epoxy-bonded to the gold, which can then be used for stripping the gold, resulting in the silicon epoxy gold sandwich.

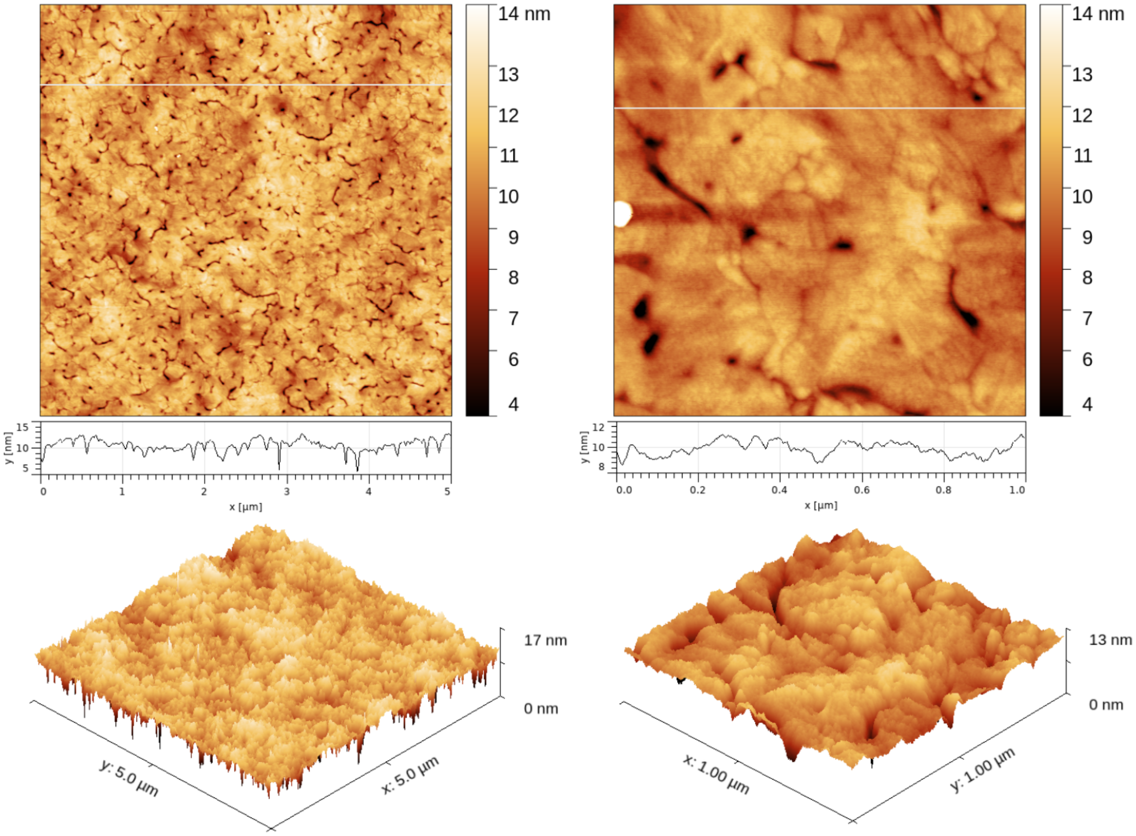

Figure 4.4: Tapping mode AFM images of TSG taken at ambient conditions on a MultimodMultimode Nanoscope III AFM. The left image shows a 5 μm by 5 μm scan area and the left shows a 1 μm by 1 μm area of the same sample. The line traces are indicated in the AFM images with a grey line. We see local variations of subnanometer and global variations on the order of several nanometers.

4.2 Self Assembled Monolayers of Alkane Thiols

Self-assembled monolayers of alkanethiols form on Au substrates by spontaneous adsorption by either the vapor or liquid phase. By submerging a freshly prepared Au substrate in a dilute solution of alkanethiols from minutes to weeks. The simplest method in achieving this is by incubating a clean gold substrate in a solution of alkanethiols [23, 24, 25]. We will eventually use these SAMs as thin film barriers to electron transport between a back electrode and a redox molecule.

4.2.1 Solution Preparation and Incubation

In our experiments, we want to grow a binary SAM consisting of a ferrocene-terminated hexadecanethiol ($FcC_{16}SH$) diluted to low coverage in non-functionalized alkanethiols ($C_{15}SH$). We want the ferrocene to be dispersed so that we can perform experiments on a single molecule without fear of several molecules being electrostatically coupled. The $FcC_{16}SH$ provides us with a redox molecule separated from the Au substrate by an alkane tunnel barrier while the $C_{15}SH$ simply acts as a background dilution layer to encourage dispersion among the ferrocene. The extra carbon on the ferrocene thiol means that the ferrocene molecules will be sticking out on top of the dilution layer, allowing them to be fully exposed for AFM and electrochemistry measurements [23, 24].

We chose to prepare our binary SAMs using a single incubation approach, although it is possible to use a two-step approach as can be seen in [1]. All of the sample preparation was done in ambient conditions. Before preparing samples, all of the glassware being used was washed three times with ethanol. A solution of 1 mM $C_{15}SH$ in ethanol was prepared in ambient conditions by dissolving 6.11mg of $C_{15}SH$ into 25 mL of pure ethanol. The solute was dissolved by gently flipping the sealed volumetric flask upside down. If non-dissolved chunks remained, the flask was heated under hot tap water for approximately 1 minute and was gently stirred again by inverting the flask. A solution of 1 mM $FcC_{16}SH$ in ethanol was prepared by dissolving 0.89mg of $FcC_{16}SH$ into 2 mL of pure ethanol. The same mixing procedure was used as above. However, if chunks of solute persisted, the flask was ultrasonicated in a room-temperature bath for a few seconds and then the solution was gently mixed again until full dissolution. To prepare the binary incubating solution, the $FcC_{16}SH$ is then be diluted by the $C_{15}SH$. The $FcC_{16}SH$ concentration can easily be tuned by adjusting the volumes of the two constituents. In this study, we used concentrations varying from 0.05% to 5% $FcC_{16}SH$ by volume.

The incubation solution is then be added into a 5 mL glass incubation vial. A freshly cleaved TSG sample is then immersed in the vial, with the Au surface facing up. The incubation is kept out of UV light either by incubating in a dark area or by covering in aluminum foil. After the desired incubation time, the sample is removed and washed with 50 mL of ethanol from a high-pressure squirt bottle. It is then gently rinsed with deionized water to check the hydrophobicity of the SAM, and then blown dry with high-pressure nitrogen. This procedure is illustrated in figure 4.5.

The stock solution, which is prepared in 25 mL, can be stored for future incubations. The flask is wrapped in aluminum foil to protect the thiols from degrading via UV light and is stored in the freezer at $-20°C$. When a fresh sample needs to be incubated, the stock solution is heated under hot tap water for 1 to 2 minutes, allowed to cool to room temperature, then is transferred into an incubation vial. The stock solution is then returned

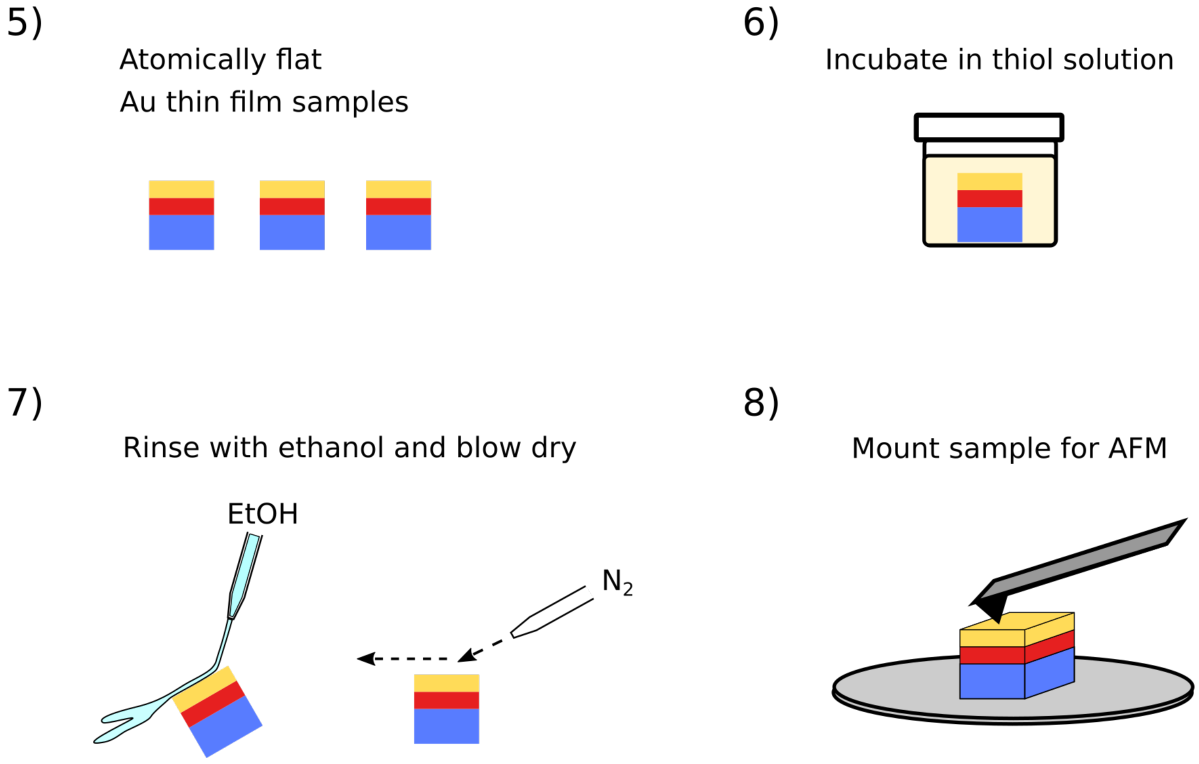

Figure 4.5: This cartoon shows the process of using atomically flat TSG samples to create SAMs. The gold is incubated in an alkanethiol solution, then rinsed with ethanol and blown dry with high-pressure nitrogen. It is then mounted on for AFM scanning or can be inserted into the electrochemical cell for cyclic voltammetry measurements.

to the freezer for storage. Stock solutions as old as 4 weeks have successfully been used with no adverse effects of storage.

Older solutions have been used, but upon incubation, they show a global roughness of features on the order of tens of microns. These films and others that showed this global roughness were studied with AFM and electrochemistry, and there were no measurable side effects in the characterizations. Despite the global roughness, there were no local effects. However, as protocol, we now choose not to use solutions older than 4 weeks.

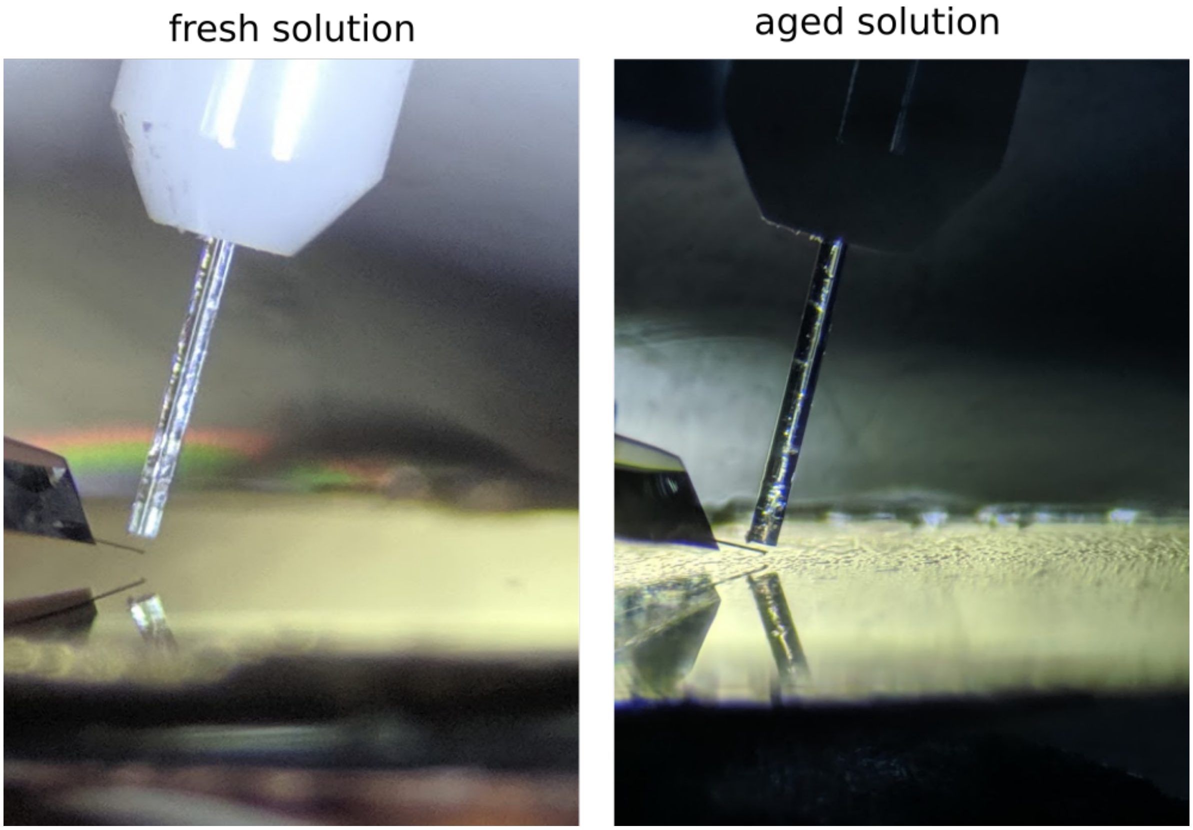

Figure 4.6: Pictures of a freshly incubated SAM and a SAM incubated in an 8-week old stock solution. As we can see, the fresh SAM appears flat and reflective as we expect while the aged stock solution SAM has a global roughness/film across the entire surface. No local side effects were seen due to this roughness, as it seems these global features are much larger than our typical 1 μm by 1 μm scan area.

4.2.2 Characterization of SAMs

To characterize our SAMs samples, we studied both its physical surface characteristics and electrochemical properties by using AFM and cyclic voltammetry measurements. Through performing these measurements, we were trying to identify and count the ferrocene molecular density in our SAMs. Here we show how to identify and characterize molecules in our SAMs, and in section 5, we explain how we count the molecules and discuss the apparent disparity between the surface and electrochemical measurements.

AFM Characterization

For surface characterization of the prepared SAMs, intermittent contact mode AFM was performed using a Multimode Nanoscope III AFM with 240AC-PP microcantilevers by Opus. Our platinum-coated tips and supplemental electronics for the MultiMode allow us to perform Kelvin Probe Force Microscopy (KPFM) in conjunction with amplitude modulation AFM. In addition to the topography and phase information from intermittent contact mode, we are also able to extract spatially resolved information about the work function of our sample surface. A cartoon illustration of what our SAM looks like under an AFM probe and the molecular sketch of ferrocenylhexadecanethiolate and pentadecanethiolate molecules is shown in figure 4.7.

The topography channel from a scan of a TSG sample incubated in 0.05% $FcC_{16}SH$ binary thiol incubation solution is shown in figure 4.8. We can see the Au substrate similar to images of bare Au in figure 4.4, especially in the grain structure of the Au. However, we notice that the Au seems a bit hazy, which is a result of the $C_{15}SH$ SAM layer covering it. We see small blobs distributed across the surface. A line trace shows a cut of the image which intersects two blobs, and we see that they are approximately 20 nm wide and 1 nm tall. We suspect that these blobs are the ferrocene head groups of the $FcC_{16}SH$ molecules. The observed height is what we would expect for an additional carbon-carbon bond and ferrocene molecule. The width is of the blob is dependent on the tip radius we are using. Since the molecule is essentially a single point, we are imaging the tip via a tip-convolution

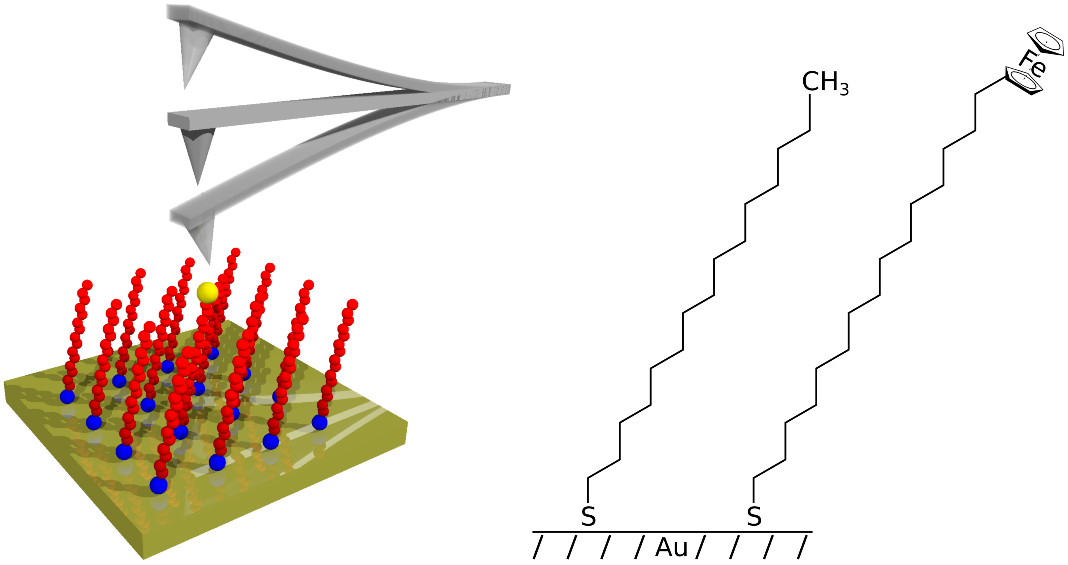

Figure 4.7: Left shows a cartoon illustrating how our SAM would look on TSG. The blue spheres are the sulfurs adsorbed to the Au substrate, and the red chains represent the alkanes. The yellow sphere at the top of the alkane in the middle represents a ferrocene molecule. Note, the cantilever is not drawn to scale. Right shows the molecular sketch of ferrocenylhexadecanethiolate and pentadecanethiolate molecules.

effect.

Another set of AFM images of a TSG sample incubated in 0.5% FcC$_{16}$SH binary thiol incubation solution is shown in figure 4.9. The topography image has very similar features as figure 4.8. Note, there are more blobs per area, which is a result of the higher concentration of ferrocene in the solution that will be discussed in section 5. It is interesting to note that we also see a contrast of the blob regions in the phase image and KPFM image. As far as we are aware, this has never been observed before.

The phase image is composed of the phase shift signal, or delay, between the oscillation of the cantilever as it comes into and out of contact with the sample. The phase is a measurement of energy dissipation involved in the interaction between the tip and sample. Factors including viscoelasticity, adhesion, and contact area all contribute to the phase contrast, but it is difficult to define the actual mechanism for phase contrast [26]. Since we see phase contrast in the blobs, we know there is different energy dissipation in the blobs than in the background, which we would expect to see if these blobs were, in fact, ferrocene molecules.

The KPFM measurement spatially resolves the work function of the surface of our sample [27]. We see large contrast differences between the TSG background grain boundaries, which is explained by the SAM not growing uniformly across a grain boundary. Although not as well defined, we also see KPFM contrast from the surface blobs. Although we can't be quantitative about the work function in this scan, we can see that there is a work function difference between the blobs and the diluting C15 SAM layer. Again, we would expect to see some work function contrast.

These AFM images do not prove that the blobs we are seeing are ferrocene molecules, but they do provide strong evidence to suggest it. To be certain, we need to perform single-electron charging experiments on our samples to see if they are redox-active molecules.

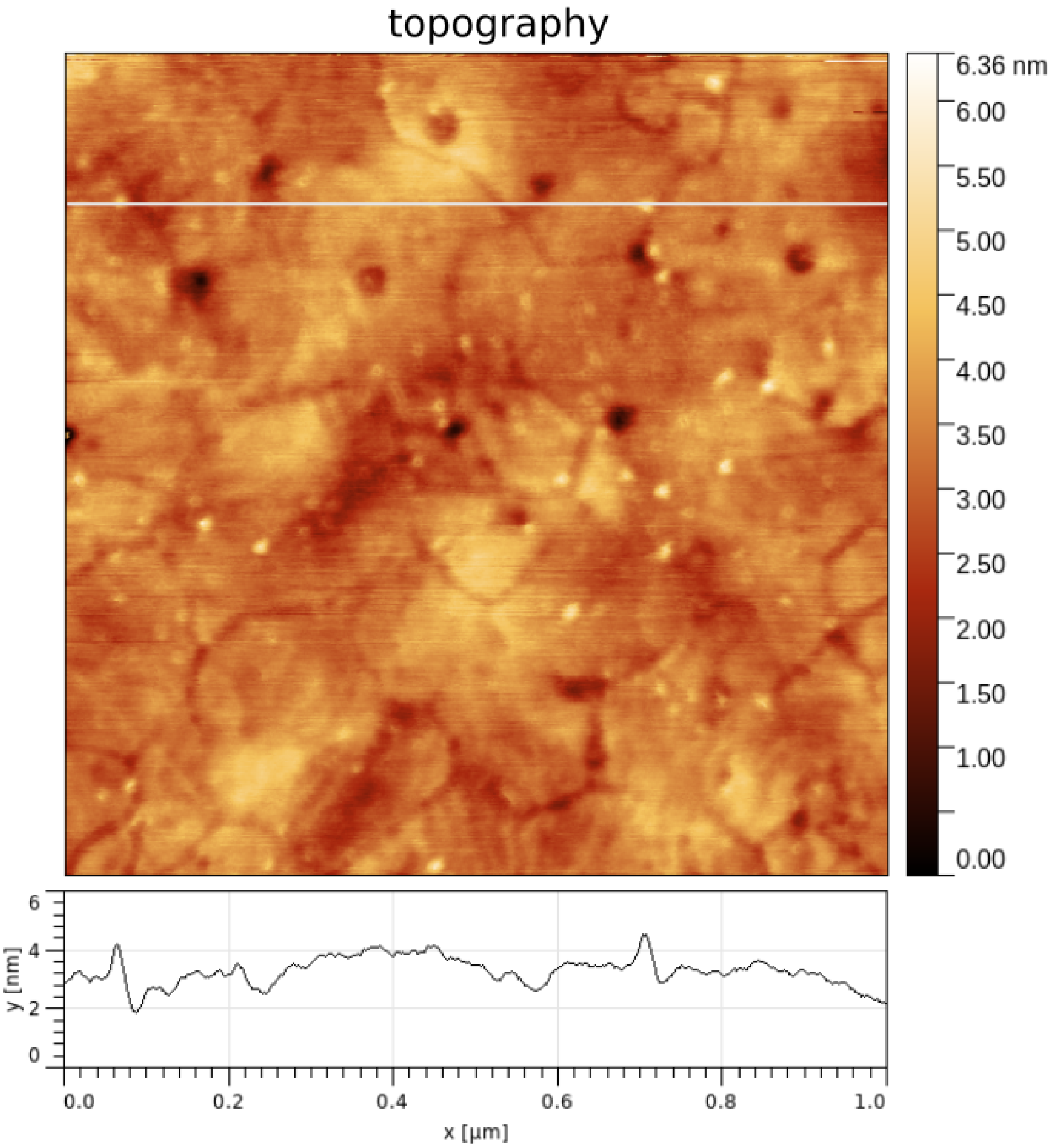

Figure 4.8: The topography channel of an intermittent contact mode AFM image of a TSG sample incubated in 0.05% $FcC_{16}SH$ binary thiol incubation solution. In this 1 μm by 1 μm scan, we can see the atomically flat TSG in the background with grain boundaries (made hazy by the $C_{15}SH$ thiols) and we the ferrocene molecules as small blobs on the surface. If we look at the trace plotted below the AFM image, we see the two peaks of approximately 1nm in height correspond to the bright colored blobs.

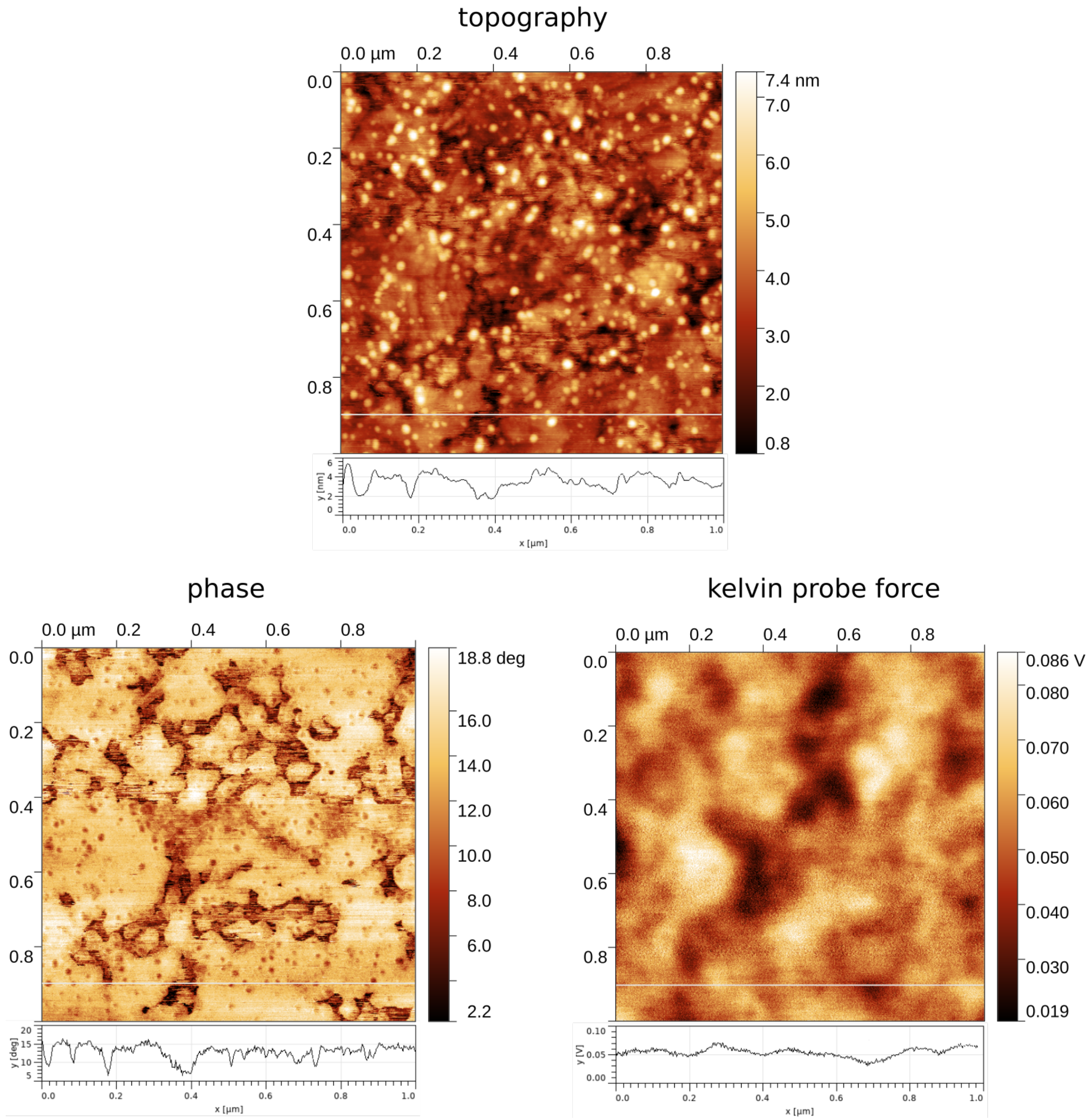

Figure 4.9: The topography, phase, and KPFM images from a 1 μm by 1 μm scan of a sample incubated in a 0.5% $FcC_{16}SH$ binary thiol incubation solution. As we can see, there are strong contrast blobs in the topography and phase channels while there is weak contrast in the KPFM channel. The same line trace is shown in all channels.

4.3 Electrochemistry Measurements

Electrochemistry is a powerful tool for physicists and chemists to probe reactions involving the transfer of electrons. This transfer of electrons can result in chemical changes or the creation of ions, and is manifested as chemical reduction or electrochemical reduction. To illustrate the difference between chemical and electrochemical reduction/oxidation, we can look at the reduction of ferrocenium as illustrated in figure 4.10.

Ferrocenium $[\mathrm{Fe(Cp)_2}]^+$ abbreviated as Fc^+ can be reduced to ferrocene $[\mathrm{Fe(Cp)_2}]$ abbreviated as Fc, by gaining a single electron via homogeneous electron transfer. In this notation, Cp is the abbreviation for cyclopentadienyl, the organic part of the ferrocene molecule. In an example chemical reduction using cobaltocene, $[\mathrm{Co(Cp^*)_2}]$ can reduce Fc^+ because the lowest unoccupied molecular orbital (LUMO) of Fc^+ is at a lower energy than the electron in the highest occupied molecular orbital (HOMO) of $[\mathrm{Co(Cp^*)_2}]$, as shown in equation 4.1. In solution, the transfer of the electron between the two molecules is thermodynamically favorable, thus the energy level difference is the driving force for the reaction. Note, the work in this thesis does not involve cobaltocene, it is simply used as an example for chemical reduction.

$$\mathrm{Fc}^+ + [\mathrm{Co(Cp^*)_2}] \rightleftharpoons \mathrm{Fc} + [\mathrm{Co(Cp^*)_2}]^+ \tag{4.1}$$

In the electrochemical reduction, Fc^+ is reduced via heterogeneous electron transfer from the electrode. An external voltage is applied to the electrode, allowing us to modulate the energy level of the electrons in the electrode. Once the electrons are at an energy level higher than the Fc^+ LUMO, an electron from the electrode will transfer to the Fc^+, as shown in equation 4.2. The driving force in this reaction is the potential difference between the Fc^+ LUMO and the electrode [28].

$$\mathrm{Fc^+} + \mathrm{e^-} \rightleftharpoons \mathrm{Fc} \tag{4.2}$$

This electrochemistry method for redox allows easy controllability of the reaction by tuning the energy level of the electrodes while being able to measure the thermodynamic and kinetic properties of the reaction. By sweeping the voltage of the electrode from low to high voltages, and thus modulating its energy levels from those below to above the Fc^+ HOMO, we can repeatedly measure the reduction of the reaction. Then by reversing this, and applying high to low voltages, we can observe the oxidation of the reaction. This technique of sweeping the voltages and measuring reaction kinetics is known as cyclic voltammetry (CV).

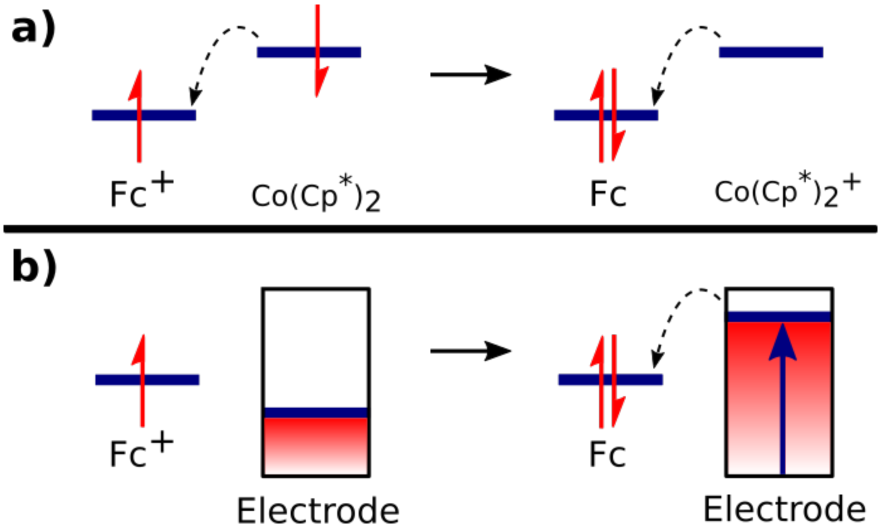

Figure 4.10: Comparison between homogeneous chemical reduction (a) and heterogeneous electrochemical reduction (b). In the chemical reduction, the driving force of the electron transfer is the energy level difference between the [Co(Cp*)$_2$)] LUMO and the Fc$^+$ HOMO. In the electrochemical reduction, the driving force is the energy level difference between the electrode and the Fc$^+$ HOMO. Adapted from [3].

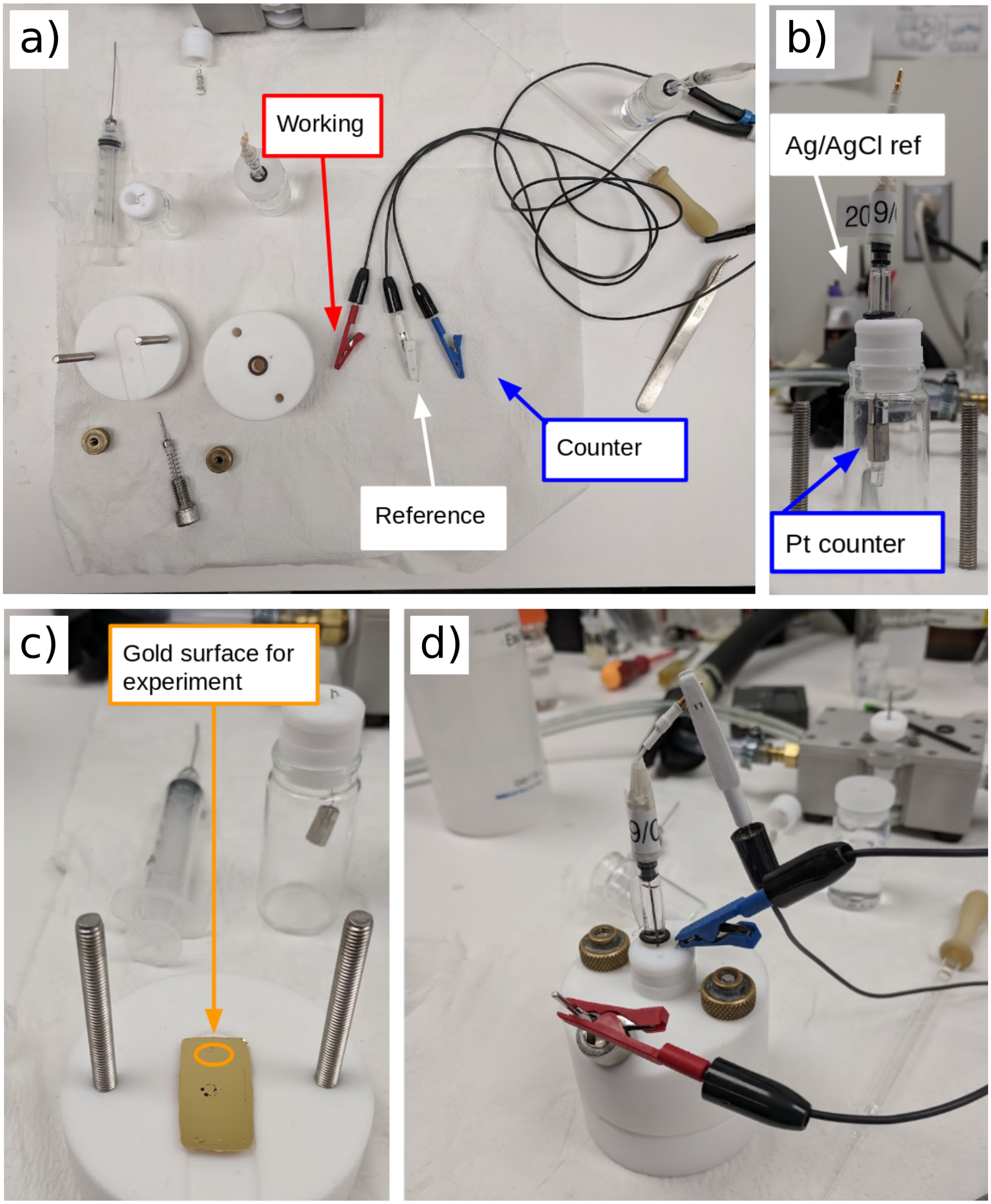

Figure 4.11: Pictures of the electrochemical cell used for our cyclic voltammetry measurements. a) The disassembled cell with the three electrode alligator clips from the potentiostat. b) The reference Ag/AgCl reference electrode and Pt counter electrode used for the experiment. c) The SAMs prepared slide installed for the experiment and the area that will be used for the CV measurements. d shows the fully assembled cell ready for measurements.

4.3.1 Electrochemical Cell

Our CV experimental system consists of an electrochemical cell, a potentiostat, and a data acquisition system. The electrochemical cell consists of three electrodes - the working, counter and reference electrodes - and an electrolyte solution. The entire cell is machined out of Teflon and can be seen in figure 4.11. In our case the working electrode is the gold Au substrate that the SAM is grown on, the reference electrode is silver chloride Ag/AgCl, and the counter electrode is platinum Pt. The electrolyte solution we use is 100 mM $NaClO_4$ sodium perchlorate. The working electrode's potential is varied linearly with time and the reference electrode maintains a constant potential such that we can accurately reference the working electrode voltage. The counter electrode completes the circuit by conducting current from the source to the working electrode. This is the current we measure during the CV measurement. The electrolyte solution provides ions to facilitate the redox reaction. Before experiments, the electrolyte is degassed with Nitrogen for 30 minutes.

4.3.2 Cyclic Voltammograms

The result of the CV measurement is a plot of the current response to the applied potential to the working electrode, known as a voltammogram or cyclic voltammogram. An example of a single sweep of a cyclic voltammogram shown in figure 4.12. The applied potential begins at -100 mV vs. Ag/AgCl, and is then linearly swept at 10 mV/s until 600 mV vs. Ag/AgCl. The voltage is then ramped from 600 mV vs. Ag/AgCl back to -100 mV vs. Ag/AgCl at the same scan rate.

Electrochemistry of the SAM-Bound Ferrocene

To understand the cyclic voltammogram, we need to understand the single electron transfer equilibrium between Fc and Fc^+. The current measured for the redox-active SAMs results from coupled electron transfer and ion-pair reactions where the electrogenerated Fc^+ pairs with anions present in the electrolyte solution. The electrochemical oxidation of the SAM-bound ferrocene to ferrocenium is summarized in the following equations:

$$\begin{gathered} \mathrm{Fc_{SAM}} \rightleftharpoons \mathrm{Fc^+_{SAM}} + \mathrm{e^-} \\ \mathrm{Fc^+_{SAM}} + \mathrm{X^-_{(aq)}} \rightleftharpoons \mathrm{(Fc^+X^-)_{SAM}} \end{gathered} \tag{4.3}$$

where the first equation is the charge transfer process and the second is the purely chemical ion-pairing process. These two processes occur in a concerted manner, that is, the electron transfer does not occur if the ion-pairing reaction is not favorable (as is the case of hydrophilic anions). Pairing of the anion X^- with the ferrocenium will neutralize excess positive charge generated at the SAM/electrolyte solution interface, thus stabilizing the oxidized cation [29].

The forward scan is known as the oxidation trace. As the sample is scanned to greater potentials, the Fc at the electrode surface is oxidized to Fc^+ as the potential becomes more positive. As the concentration of Fc^+ increases at the electrode, it forms a diffusion layer, slowing the diffusion rate of Fc to the electrode. The peak current is eventually reached around 200 mV vs. Ag/AgCl, but further increasing the potential results in a decrease in current as the diffusion rate slows and there is no difference between the concentrations of Fc and Fc^+. The changing concentrations of the ion species are described by the equation 4.3. At the switching potential, the potential is scanned from 600 mV vs. Ag/AgCl to -100 mV vs. Ag/AgCl. The concentration of Fc^+ ions is depleted as they are reduced to Fc. Similar to the oxidation trace, a diffusion layer of Fc forms at the electrode, slowing the diffusion of Fc^+ to the electrode.

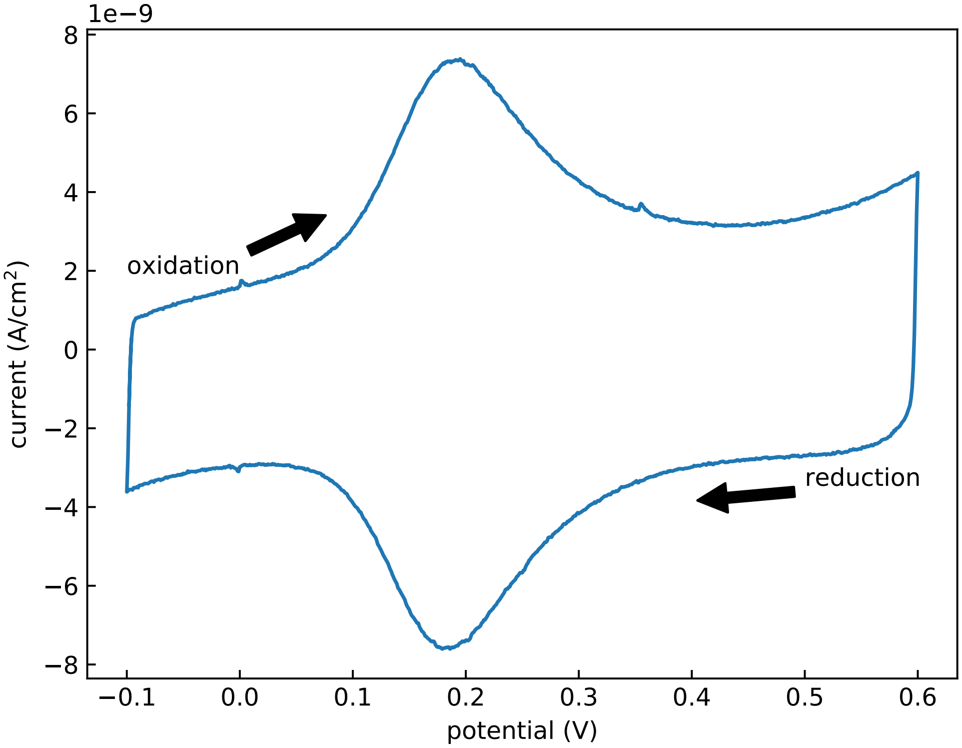

Figure 4.12: An example cyclic voltammogram of 0.05% Fc-C_{16}SH at a scan rate varying from 0.1V. The ferrocene molecules undergo oxidation as the potential is swept from -100 mV vs. Ag/AgCl to 600 mV vs. Ag/AgCl, are are reduced again as the potential is ramped back down to -100 mV vs. Ag/AgCl.

Baseline Subtraction via Asymmetric Least Squares Smoothing

One common characteristic of a cyclic voltammogram that needs to be considered to analyze data is the presence of background current. As we can see in figure 4.12, the peaks are situated on top of a box-like background. This non-faradaic background current is the result of the electrical double layer at a charged electrode [30].

For the scope of this work, we can consider the simple capacitive model of charging current. Let us consider our electrochemical cell containing an inert electrolyte, in which no charge passes across the electrode-solution interface. If we apply a potential to the electrode which varies from its equilibrium we see that a charge imbalance will arise across the interface. For this to be neutralized, the charged species in the solution near the electrode surface will rearrange until it is neutral.

This interfacial region can be modeled as a capacitor, where its capacitance C is defined by the charge on the capacitor and potential across the capacitor as $C = q/E$. Whenever there is a potential change at the electrode, charges flow at the interface until the capacitance equation is solved and the charges are neutralized. This charging current is what we see as the background current in our cyclic voltammograms. A simple cartoon of this capacitive model for the double layer is shown in figure 4.13. In reality, the structure of the double layer is more nuanced in its explanations, and are given a thorough explanation in Bard's Electrochemical methods: fundamentals and applications [30].

To analyze the oxidation or reduction peak, it is necessary to remove the background non-faradaic current. Since the peak will ultimately be integrated to determine the number of ferrocene molecules in our sample, it is critical to determine an accurate and reproducible baseline. Due to the varying nature of the peak and background between different samples, fitting a baseline (for example a linear baseline) is non-trivial. For reproducibility and robustness, we chose to implement a baseline correction using asymmetric least squares smoothing for automatic baseline detection and subtraction.

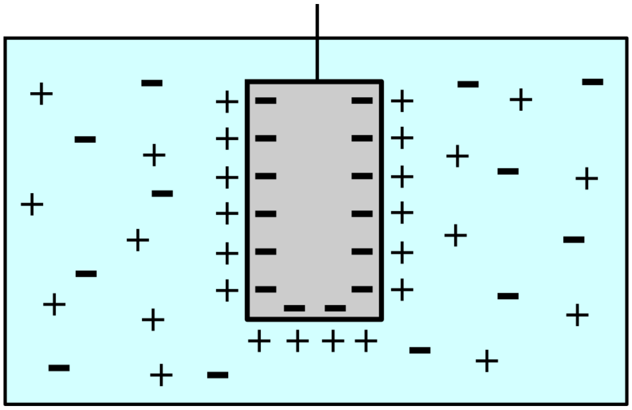

Figure 4.13: A cartoon of the capacitive model for the double layer in the electrochemical cell. When there is a potential change at the electrodes, charges flow at the interface until the charges are neutralized.

If we let y be a signal of length m, and z be another series which is smooth and faithful to y, we can minimize the penalized least squares function

$$S = \sum_i \omega_i \left(y_i - z_i\right)^2 + \lambda \sum_i \left(\Delta^2 z_i\right)^2 \tag{4.4}$$

where $\Delta^2 z_i = -\left(z_{i-1} - z_{i-2}\right) = z_i - 2z_{i-1} + z_{i-2}$. The first term measure the fit to data, and the second term is the penalty term for behaviour in z that is non-smooth. The parameter λ simply tunes the balance between each term, and the vector w are weights that minimize S. The minimization leads to a the system of equations

$$\left(W = \lambda D'D\right) z = Wy \tag{4.5}$$

where $W = diag(\omega)$ and D is a difference matrix. The number of equations is equal to length m, but due to the sparseness of the matrix where only the main diagonal and two sub-diagonals are non-zero [31], it is quickly solved via Python programming language.

This implementation allows us a fast means of baseline fitting with two parameters we can manually tune; λ tunes the smoothness of the baseline and p tunes the asymmetry. The Python implementation is shown below. Typically, we use values of $\lambda = 1 \times 10^7$ and $p = 0.001$. The default number of iterations is set to 10 but can be adjusted if convergence isn't achieved. The full derivation for the technique can be found in reference [31].

```
def baseline_als(y, lam, p, niter=10):
  L = len(y)
  D = sparse.diags([1,-2,1],[0,-1,-2], shape=(L,L-2))
  w = np.ones(L)
  for i in range(niter):
    W = sparse.spdiags(w, 0, L, L)
    Z = W + lam * D.dot(D.transpose())
    z = spsolve(Z, w*y)
    w = p * (y > z) + (1-p) * (y < z)
  return z
```

The application of this baseline can be seen in figure 4.14, where the baseline of several different scans was determined, and subtracted, resulting in oxidation peaks that could be integrated and studied. The extracted background capacitances were consistent between the tested varying scan rates, with the $C_{background} = 381 \pm 28$ μF, as shown in figure 4.15.

Characterizing Reaction via Scan Rate

The scan rate of the CV experiment has significant effects on the cyclic voltammogram. Increasing the scan rate of the reaction leads to a decrease in the diffusion layer at the electrode. This decrease in the diffusion layer leads to an increase in the rate at which ions can be oxidized or reduced, thus resulting in larger currents during oxidation and reduction.

We performed CV measurements on a sample of 0.05% Fc-C_{16}SH at successive scan rates varying from 0.1 V/s to 1.0 V/s. The full oxidation and reduction cyclic voltammograms are shown in figure 4.14 top. If we look at just the oxidation traces, we can use our baseline correction algorithm to fit the baseline, of each plot, which is shown as the black dashed lines for each trace in figure 4.14 middle. By then subtracting this determined baseline from each trace, we are left with baseline-corrected voltammograms as shown in figure 4.14 bottom.

With the corrected oxidation voltammogram, we can extract the peak area, peak current, and peak potential. The area was calculated via a Python implementation of the composite trapezoidal rule, and the peak was determined via the Python scipy signal package. Plotting the peak area versus the scan rate gives us a linear, as shown in figure 4.15 left, which is the expected response for the non-faradaic response to increased scan rate [32].

To determine if the reaction is electrochemically reversible, we can plot the peak voltage vs the scan rate, as shown in figure 4.15 right. As we can see, there is no clear dependence of scan rate on peak potential, indicating a fully reversible reaction [33]. Since this reaction is electrochemically reversible, we can determine if the electron transfer is diffusion-limited or if it is a surface contained redox reaction by using the Randles-Sevcik Equation:

$$i_p = \frac{n^2 F^2}{4RT} v A \Gamma^* \tag{4.6}$$

where Γ^* is the surface coverage of adsorbed species, v is scan rate, A is the electrode area, and n is the number of transferred electrons. According to this, the peak current should vary linearly with the scan rate. As we see in figure 4.15 middle, there is a linear relationship between peak current and scan rate indicating that the reaction is surface contained redox.

4.3.3 Electrochemistry Characterization of SAMs

During a CV experiment, we measure the current response of our redox-active molecules as a response to an applied potential. During oxidation, we measure a peak, as discussed in section 4.3. If we take this oxidation trace and perform our background subtraction, we are left with a curve showing the oxidation peak of the ferrocene molecules. The shape and area of the peak can reveal valuable information and properties about the ferrocene molecules adsorbed to the surface.

In our sample preparation, we tune the concentration of $FcC_{16}SH$ in the binary solution to tune the number of ferrocene molecules that are adsorbed to our Au surface. It is important to note that due to the kinetics of the adsorption of $FcC_{16}SH$ thiols, the concentration in solution does not directly correlate to the concentration adsorbed on the substrate surface. Ultimately for our LT-AFM measurements, we want fully dispersed ferrocene molecules that don't interact with each other. Looking at the voltammogram from the CV experiment, we can analyze the peak shape to determine if the ferrocene molecules are fully dispersed or exhibit some clustering. In the perfect case where all ferrocene is fully dispersed, the oxidation peak would fit to a single Gaussian. However, if there are populations of dispersed and clustered ferrocene, the oxidation peak will be the convolution of multiple Gaussians. An example voltammogram from a sample containing 100% $FcC_{16}SH$ is shown in figure 4.16. There is a large shoulder on the left-hand side of the peak and a smaller shoulder on the right, which we can fit to three Gaussians. We can infer that there are three populations of ferrocene; most disperse (orange), less disperse (green), and clustered (red) [34]. Since individual molecules have a slightly different electrostatic environment as compared to clustered molecules, we see each Gaussian at different oxidation potentials. Although there are three Gaussians in the 100% sample, the more dilute concentrations that we typically work with have two Gaussians.

As we decrease the concentration of $FcC_{16}SH$ on our sample, we decrease the total number of redox-active molecules in our electrode area. As a result, we expect the peak area to decrease as well as the peak shape to shift from a peak with a shoulder to one resembling a single Gaussian. An analysis between samples incubated in 5% and 0.05% $FcC_{16}SH$ solution is shown in figure 4.17. Qualitatively looking at the oxidation traces, we can see that the 5% sample has an obvious shoulder while the 0.05% sample appears more Gaussian. Additionally, the 5% peak is three orders of magnitude larger than the 0.05%. We can apply our baseline subtraction analysis and fit each peak to two Gaussians. The orange Gaussian in each corresponds to the disperse ferrocene population while the green Gaussian corresponds to the less disperse ferrocene population.

The sum of the two Gaussians is plotted on top of the experimental data. To quantify the dispersity of the ferrocene for the 5% and 0.05% sample, the area of each Gaussian relative to the sum was calculated, as shown in figure 4.17 second row. In the 5% sample, the disperse ferrocene Gaussian is 83.4% of the total peak area. In the 0.05% sample, the disperse Gaussian is 92.7% of the total peak area. This shows that the relative contribution of the dispersed Gaussian is larger in the 0.05% sample, meaning the ferrocene molecules are more disperse [35].

We can calculate and plot the residuals by taking the difference between the experimental data and each fit. For each fit, we can then look at the distribution of the residuals including the mean and standard deviation. In the 0.05% Fc sample, we see that the residuals have a mean of $\mu = -0.03$ with a standard deviation of $\sigma = 0.33$, showing it fits well to two Gaussians. The 5% sample residuals have $\mu = 0.16$ and standard deviation $\sigma = 1.12$.

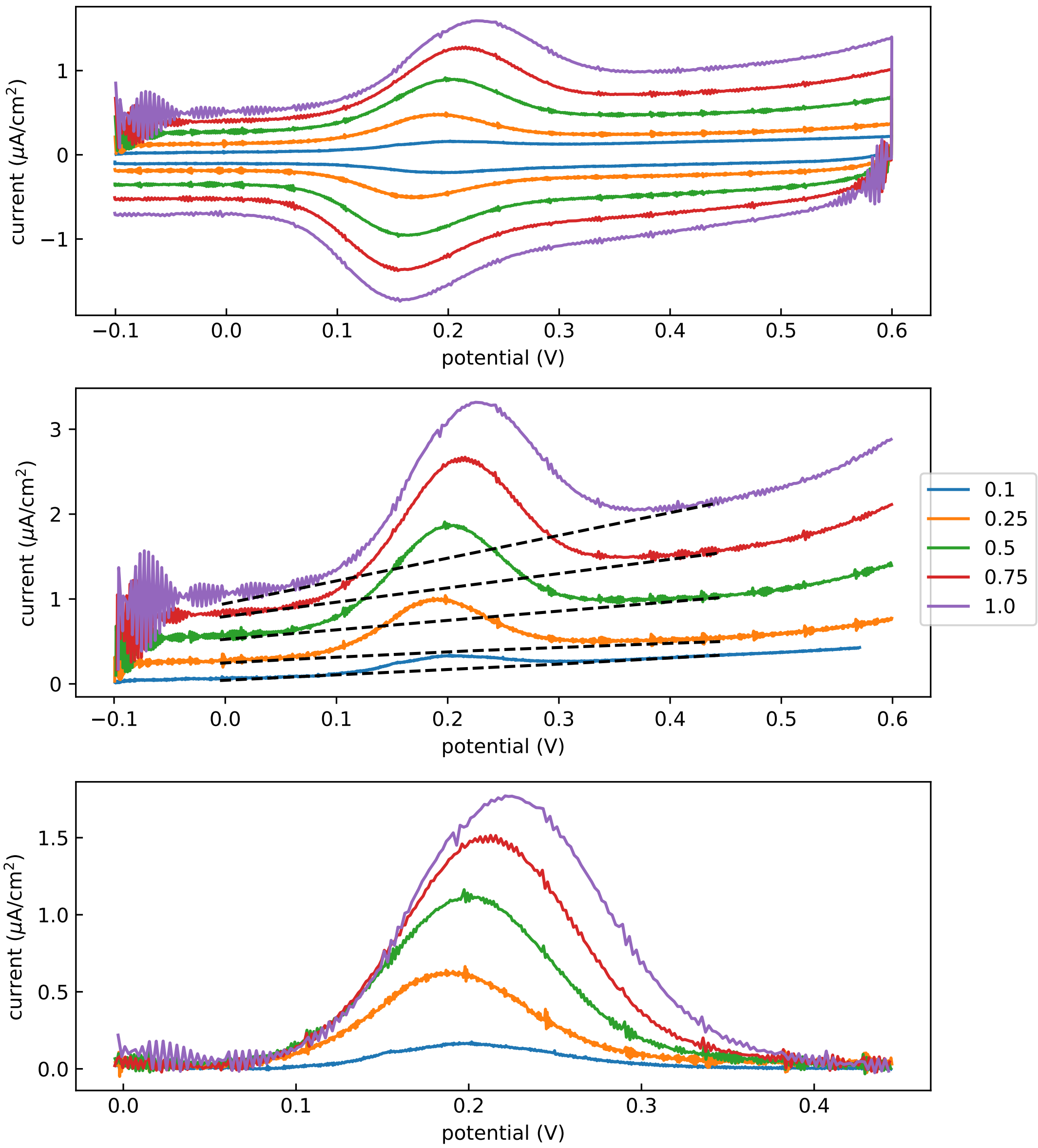

Figure 4.14: Cyclic voltammograms of 0.05% Fc-C_{16}SH at scan rates varying from 0.1 V to 1.0 V. As the scan rate increases, we see that the faradaic oxidation and reduction peaks grow in amplitude and width. We also see that the non-faradaic background increases as well. The determined baseline for each oxidation trace is determined using our asymmetric least squares baseline fitting algorithm, and the non-faradaic background is subtracted. This leaves us with clean oxidation peaks which we can then analyze. The ringing at the beginning of the peaks is a result of the electronics.

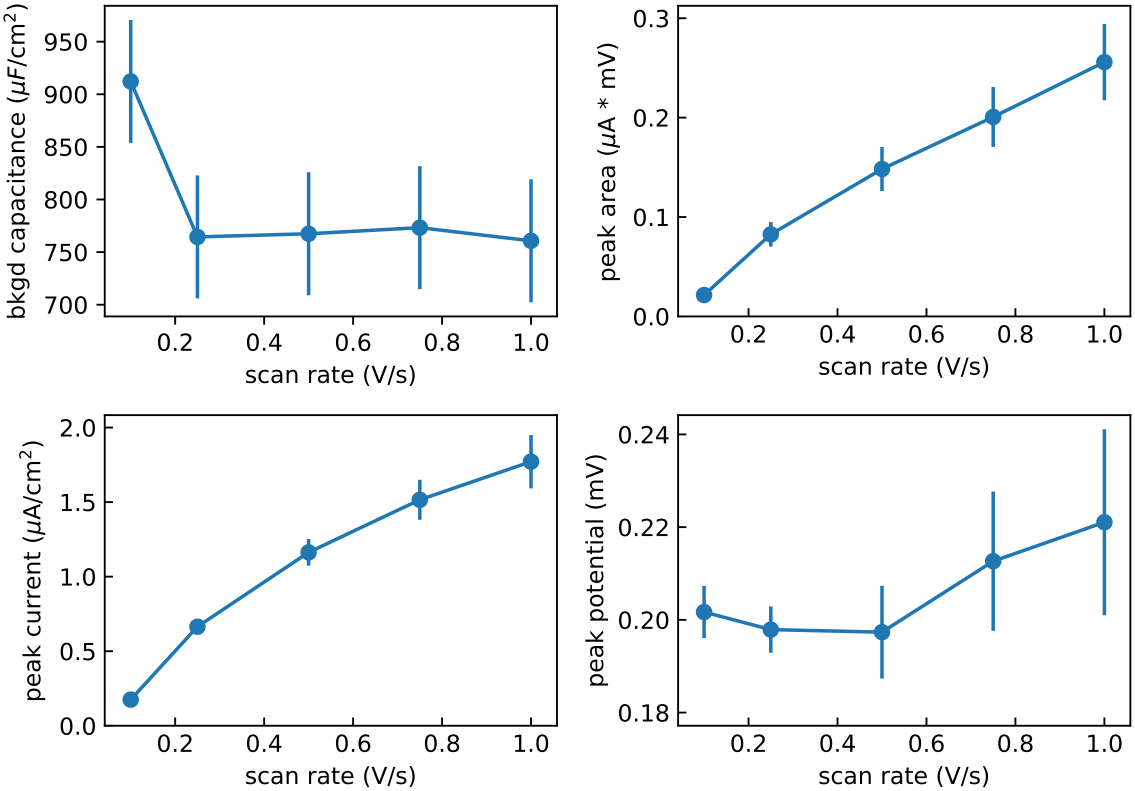

Figure 4.15: The background capacitance, scan area, peak current, and peak voltage of the data in figure 4.14 as a function of scan rate. The background capacitances are constant as a function of scan rate with $C_{background} = 381 \pm 28$ μF. The linear relationship of the area and peak current to scan rate indicates that the reaction is surface limited, not diffusive. The flat relationship between peak voltage and scan rate indicates that the reaction is reversible.

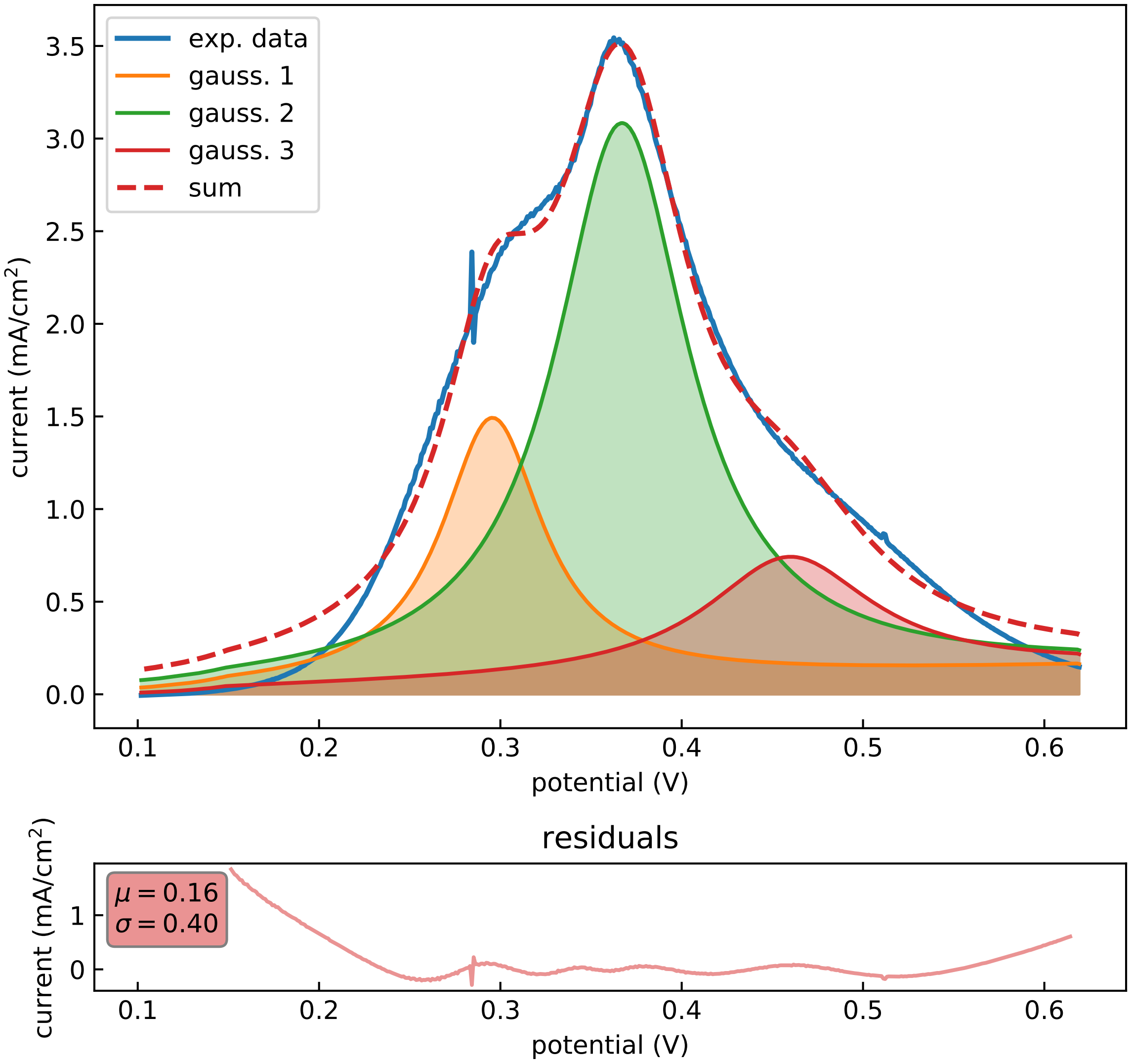

Figure 4.16: A cyclic voltammogram gathered from a CV experiment (scan rate 0.01 V/s) of a 100% $FcC_{16}SH$ solution. The peak has shoulders on both the left and right-hand side, indicating the sample isn't fully disperse. This peak fits best as a convolution of three Gaussians, implying three different ferrocene populations: most disperse (orange), less disperse (green), and clustered (red).

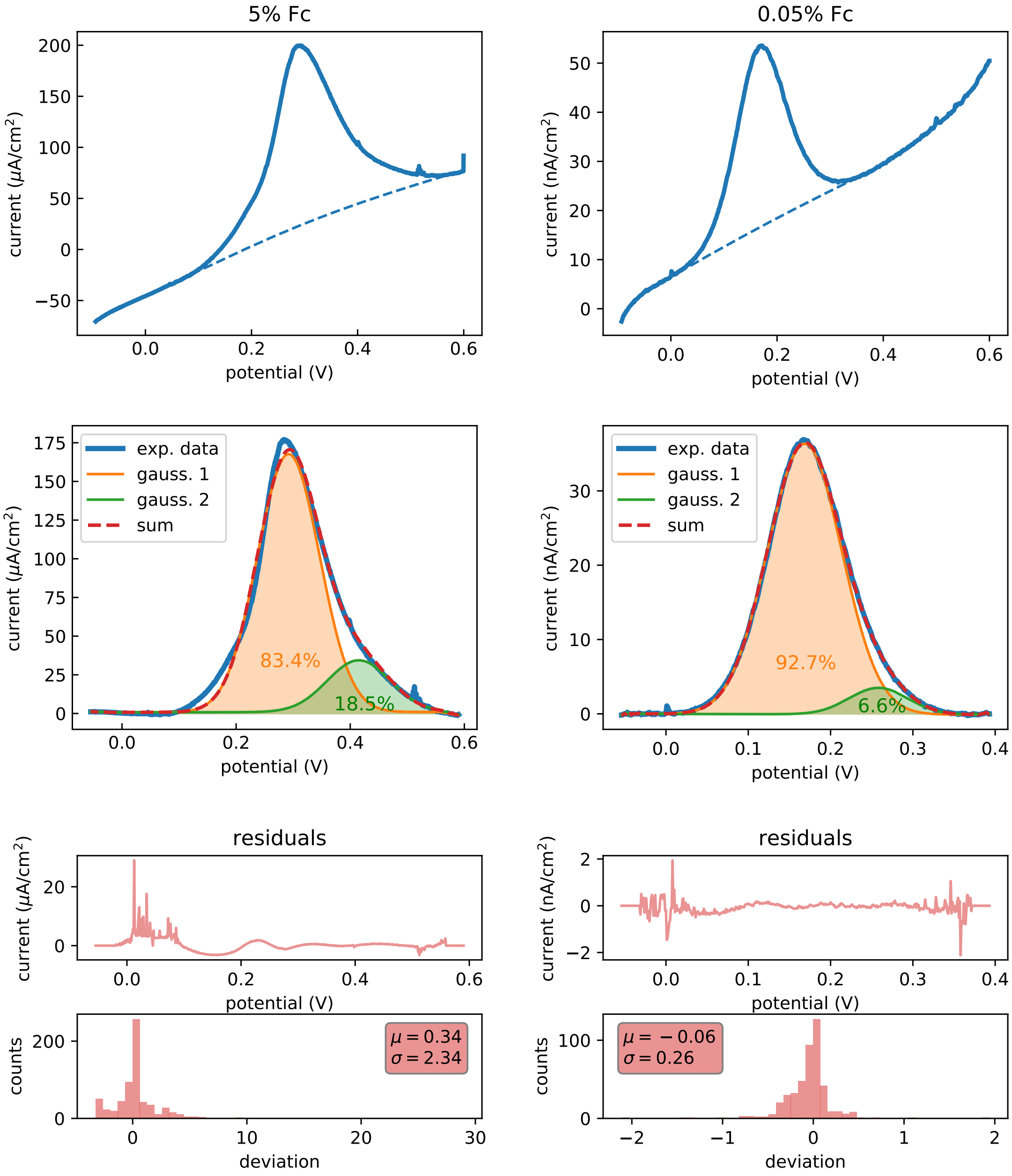

Figure 4.17: Analysis of the peak shape of 5% and a 0.05% FcC$_{16}$SH samples. The top row shows the oxidation peak with the determined background for subtraction. Note the 5% oxidation peak is three orders of magnitude larger than the 0.05% and has a shoulder. The second row shows the best two-Gaussian fit to the oxidation peak. The orange and green Gaussian are the dispersed and less dispersed population, respectively. The relative area of each Gaussian to the sum is shown as a percentage. The third and fourth row show the residuals for each fit and the standard deviation and distribution of the residuals.

5 | Results

5.1 Discrepancy Between the Number of Molecules

The ultimate goal of the $FcC_{16}SH$ sample preparation was to make samples that had fully disperse redox-active ferrocene molecules sitting on top of an insulating $C_{15}SH$ tunnel barrier on gold to be used for single-electron charging experiments. After successfully making a binary SAM at a fixed $FcC_{16}SH$ concentration, we then began to study the effects of varying the concentration of $FcC_{16}SH$ in the incubation solution. We used ambient intermittent contact AFM and electrochemistry to count the density of redox molecules on the surface of our sample. As you can see in figure 5.1, there is an increase in the density of blobs on the surface as the concentration of the $FcC_{16}SH$ is increased.

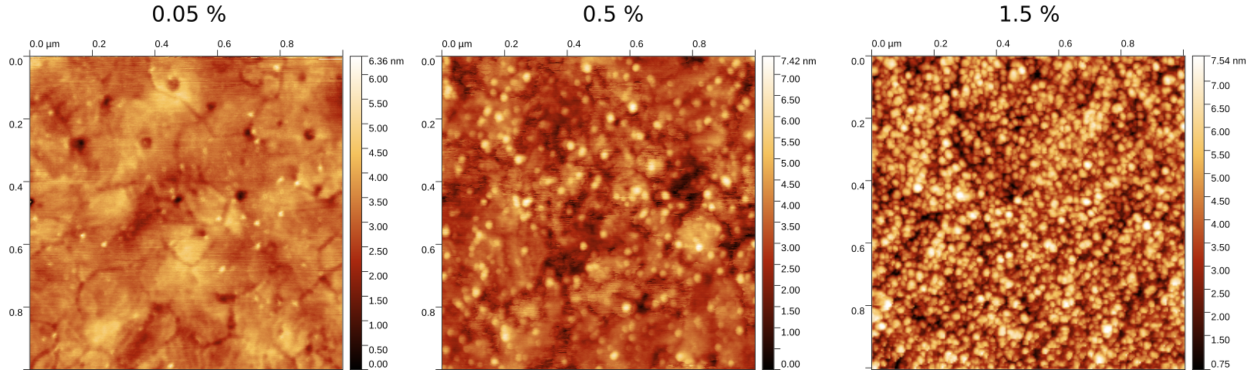

Figure 5.1: Topography intermittent contact AFM images shown of samples incubated in 0.05%, 0.5%, and 1.5% $FcC_{16}SH$ binary thiol incubation solutions. As we can see, the molecule "blobs" increase in density as the concentration of the incubating solution increases.

5.1.1 Counting Molecules via AFM

Counting the molecules from the AFM images is not as straightforward as one might imagine. The simplest method used was manually counting and marking every blob on the image.

However, this is tedious and introduces bias into the determination of what is a molecule and what isn't. However, since the molecule blobs are protrusions that should be local maxima on the surface, our samples lend themselves to using image processing to identify them. The method that proved to be the most successful for blob detection was a binary watershedding algorithm.

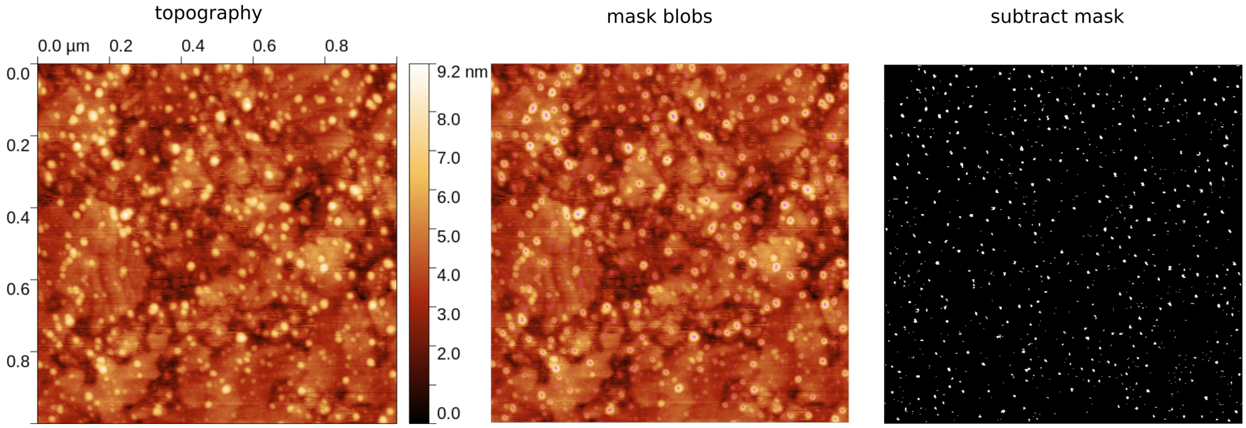

Figure 5.2: The process of determining blob location via the watershed algorithm. The watershed algorithm is run on the topography AFM image, and every determined molecule is highlighted with a mask (as shown in pink in the middle image). The mask can then be subtracted from the topography image and turned into a binary image as shown on the right. The total number of molecules can then be counted.

The watershed algorithm works for local minima determination, so we first invert our image so that maxima will now be minima. A virtual water droplet is placed randomly on the inverted surface, with a specified drop size, and it follows the steepest descent to minimize its potential energy. Once it reaches a local minima, the drop stays here, filling the local minima with its volume. This process is repeated with different drops all across the surface. We are then left with a surface scattered with small lakes. We remove the smallest of these lakes (less than 3px^2), assuming these are the result of noise, but keep the larger lakes as our true local minima, or molecule. Each lake is marked, and the total number of lakes can then be counted to arrive at our number of molecules on the surface. To visualize this, the original image can be masked using the lakes and subtracted, resulting in an image containing just points that are indicating the location of the molecules, as seen in figure 5.2. It is important to note that the resulting lakes do not reflect the exact size as the molecule, but are simply used for counting.

Although this can count the number of clear molecules on the surface, it fails in detecting the more subtle molecules that the human eye can easily measure. Those smaller looking blobs that are not sticking out from the surface as well or are hidden in grain boundaries are not easily detected with the watershed algorithm. To better improve this, it is possible to use computer vision and machine learning algorithms for automated blob detection, as shown in reference [36].

5.1.2 Counting Molecules via Electrochemistry

To count the number of molecules via electrochemistry CV measurements, we use the oxidation voltammogram for the samples of various concentrations. First, each voltammogram can be fit with a baseline using our asymmetric least squares baseline fitting as described in section 4.3.2, leaving us with clean and leveled oxidation peaks, as shown in figure 5.3. Each peak can then be integrated, leaving us with a peak area in units of $\mu A * V$. We can convert this to $A * V$, and calculate the density of charges in units $[\frac{C}{cm^2}]$ using the following equation:

$$Q = \frac{A_{electrode}}{v * A_{peak}} \tag{5.1}$$

where $A_{electrode} = 0.48cm^2$ is the electrode area, A_{peak} is the integrated peak area, and v is the scan rate. The surface coverage can then be determined by dividing Q by Faraday's constant:

$$\sigma = \frac{Q}{\mathscr{F}} \tag{5.2}$$

where $\mathscr{F} = 96485 \, \frac{C}{mol}$ is Faraday's constant. This leaves us with the surface coverage in $[\frac{mols}{cm^2}]$, which we can then easily convert to $[\frac{molecules}{\mu m^2}]$ using Avogadro's number and simple unit conversion.

Each of the oxidation peaks in figure 5.3 were also fit to two Gaussians. As we can see, the relative size of the orange Gaussian (which we attribute to the disperse population) grows compared to the green Gaussian (less disperse). This is in agreement with 4.17, and indicates that the ferrocene are more disperse as the $\mathrm{FcC_{16}SH}$ concentration in the incubating solution is decreased.

The combined plot showing the number of detected ferrocene molecules as a function of $\mathrm{FcC_{16}SH}$ concentration in the incubation solution is shown in figure 5.4. As we can see, the electrochemistry detects over 20 times more molecules than the AFM images.

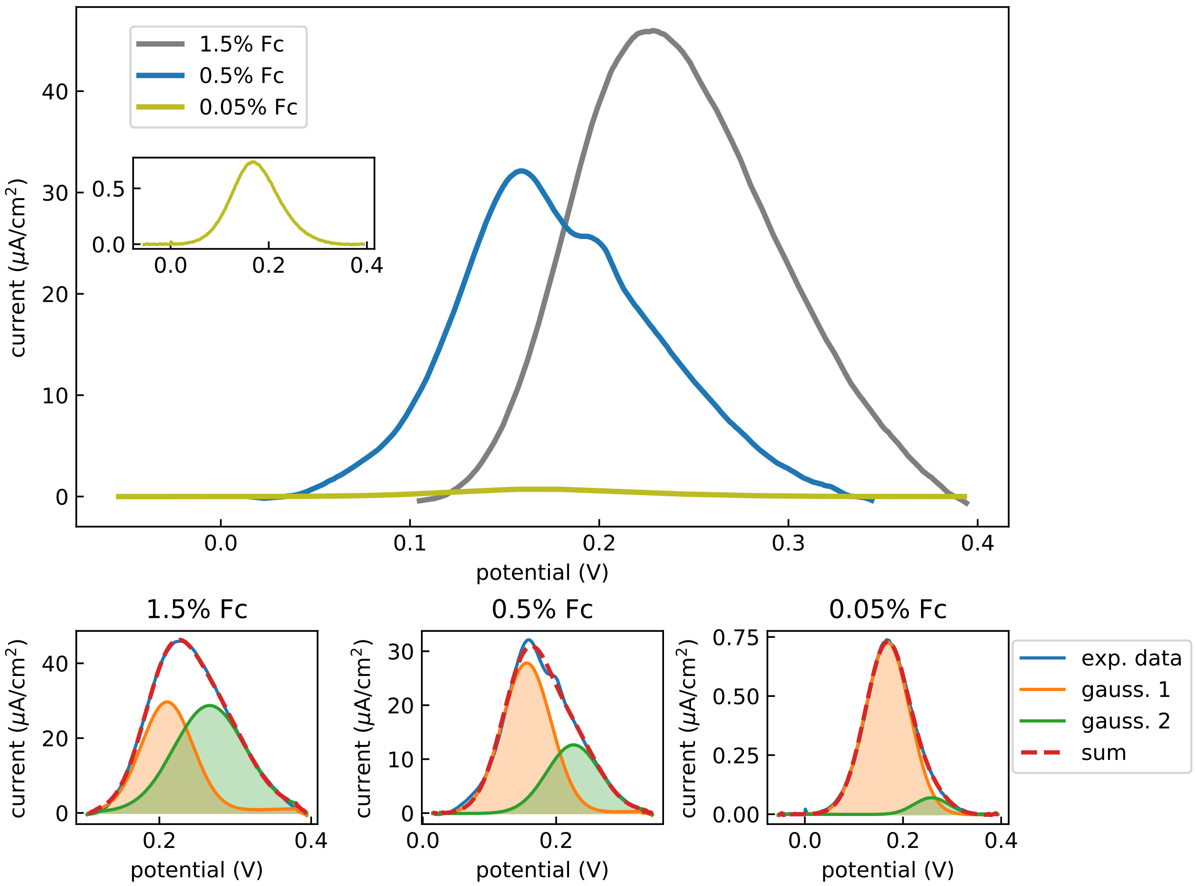

Figure 5.3: CV voltammograms of samples incubated in 1.5%, 0.5%, and 0.05% $FcC_{16}SH$ binary thiol incubation solutions. As the concentration of the incubating solution decreases, the peaks become smaller in amplitude, indicating a decrease in the number of redox active ferrocene molecules. We can fit each peak to two Gaussians, where Gaussian 1 (orange) is disperse ferrocene and Gaussian 2 (green) is less disperse. As the concentration decreases, the disperse peak grows relative to the less disperse peak. This means that the ferrocene molecules are more disperse in the samples incubated in the less concentrated solution. Note, these data sets were taken on different days. Variations in the peak position are not uncommon at such low ferrocene concentrations, and may be a result of slight changes in the electrochemical cell setup at different times (for example the age of the reference electrode).

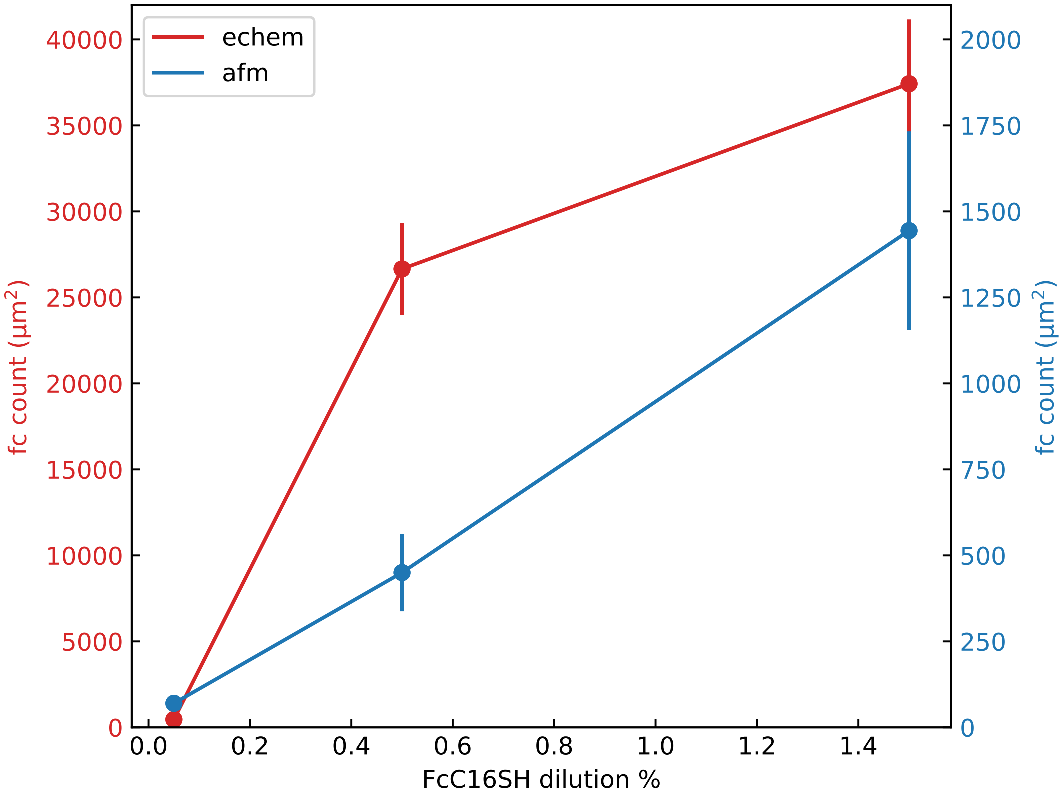

Figure 5.4: The number of ferrocene molecules per micron squared area determined via AFM images and electrochemistry measurements. The number of molecules was determined by manually counting the AFM images and by integrating the CV cyclic voltammograms. As you can see there is a discrepancy by a factor of 20 between the AFM and electrochemistry determinations. The lines are not a fit, they simply connect the data points.

5.2 LT-AFM Measurements

5.2.1 NC-AFM Measurements

As we have shown, the samples we prepare with 0.05% $FcC_{16}SH$ are shown to be evenly distributed and fully dispersed, according to the electrochemistry and AFM data. With these samples, we can pursue single-electron charging of the ferrocene molecules via e-AFM.

To perform these measurements, the prepared samples are mounted into the LT-AFM, and are pumped down and cooled down to liquid nitrogen temperatures, as described in section 2.1.1. While performing non-contact AFM on the samples at 77 K, we can see contrast blobs in the topography, frequency error, and dissipation channel, as shown in figure 5.5. These blobs are similar to those we saw in the ambient microscope performing intermittent contact AFM, which would mean that we can see where the single molecules are on our sample surface. The contrast in topography reveals protrusions that are approximately 1.5nm tall, which is consistent with the height have seen in our other images. Contrast in the dissipation channel can suggest different material properties in the blobs than the background, which is expected for ferrocene molecules on a thiol background.

5.2.2 Stability of SAMs in Electrochemistry and NC-AFM

We have shown the value in individually using electrochemistry and AFM to characterize our $FcC_{16}SH$ samples. Due to the discrepancy between the AFM and electrochemistry results, it seems natural to want to combine the use of both techniques in order to investigate the origin of this disparity. For examples, we may want to perform CV measurements followed by NC-AFM experiments on the same sample. However, we have seen that there are certain conditions where the ferrocene SAM seems to go through some irreversible process post CV measurement. In order to look at the stability of the SAM, we studied the effects of air exposure on a 0.05% $FcC_{16}SH$ sample using CV measurements.

If the sample is installed in the electrochemical cell and constantly submerged in the electrolyte solution, we see no degradation on the SAM, even after performing repetitive and

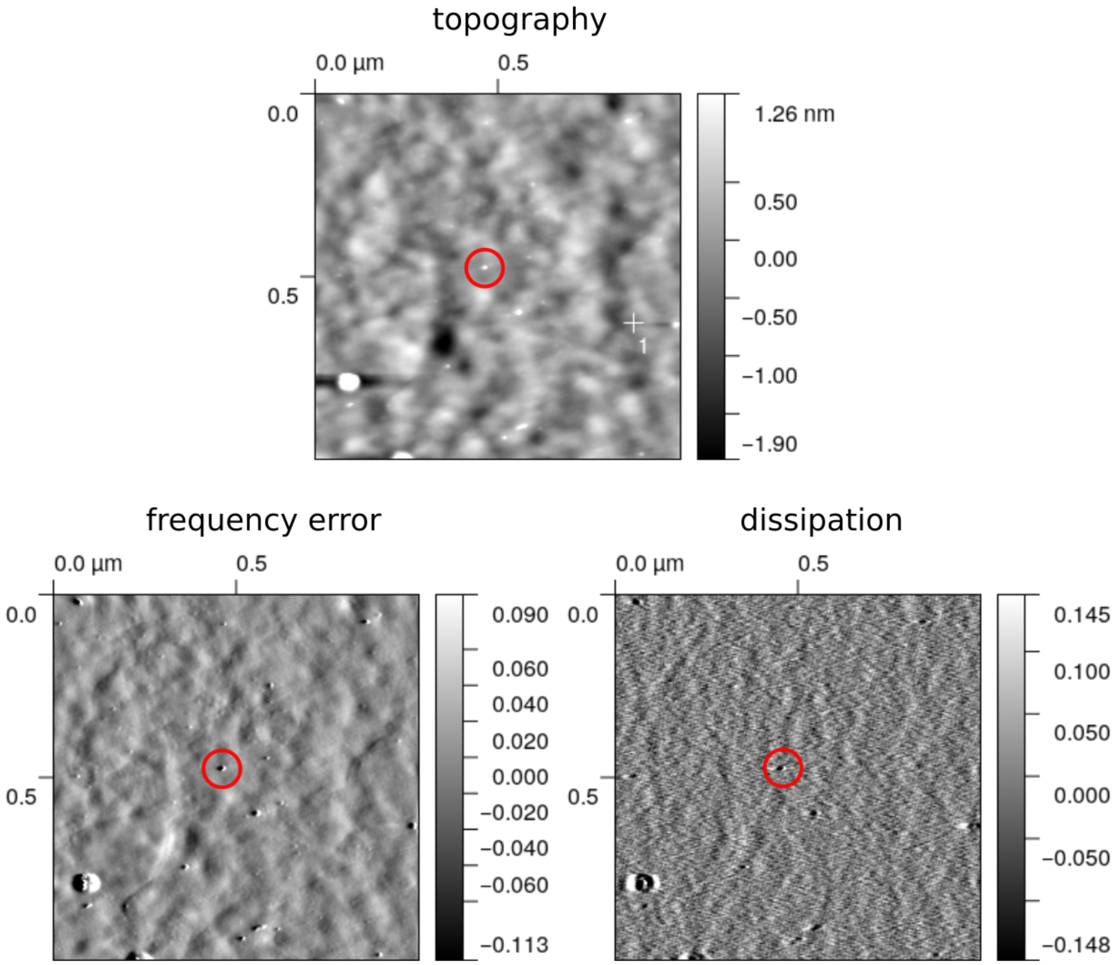

Figure 5.5: The topography, frequency error, and dissipation images from a 1 μm by 1 μm scan of a sample incubated in a 0.05% $FcC_{16}SH$ binary thiol incubation solution. The images were taken on the LT-AFM at a temperature of 77 K and a pressure of 3×10^{-4} mbar. As we can see, there is a clear contrast in the molecule "blobs" (example circled in red) that we observe with intermittent contact AFM at room temperature.

continuous electrochemistry measurements for up to an hour. However, if we perform a CV measurement on a freshly prepared SAM sample (as described in section 4.3), then clean the sample with deionized water and let sit in ambient conditions for 90 minutes, then perform another CV measurement, we see that there is serious degradation in the oxidation peak, as shown in figure 5.6. The solid blue oxidation peak turns into the dashed blue double peak. Fitting each trace to two Gaussians, we see that the peak amplitude of the disperse ferrocene (orange) is decreased by a factor of 5, and the less disperse Gaussian (green) is shifted to a higher potential, indicating more clustering in the ferrocene molecules. For comparison, we removed a fresh SAM from incubation, cleaned it as described in section 4.2, and let it sit in ambient conditions for 90 minutes. This sample, as shown in the pink curve, is a clean oxidation peak, with an even larger amplitude than the first fresh SAM before ambient exposure.

There are two important take aways from this. Firstly, there is an irreversible chemical process which can occur from performing CV measurements then leaving the sample in ambient conditions. Although we don't know the details of what is happening, it means that CV measurements should not be performed on SAM samples that will be used for electron charging experiments in the LT-AFM, as they would be exposed to an ambient atmosphere for 90 minutes. However, we see that there is no significant electrochemical effect to *only* exposing a fresh SAM to ambient conditions. This is important to us, as the sample would be exposed to ambient conditions for approximately 90 minutes during the microscope assembly. From these experiments we can confidently mount our samples without fear of electrochemical degradation occurring in the sample. This is contrary to reports in the literature that suggest preparing SAMs in a glove box as exposure to air degrades the SAM [37, 38, 39].

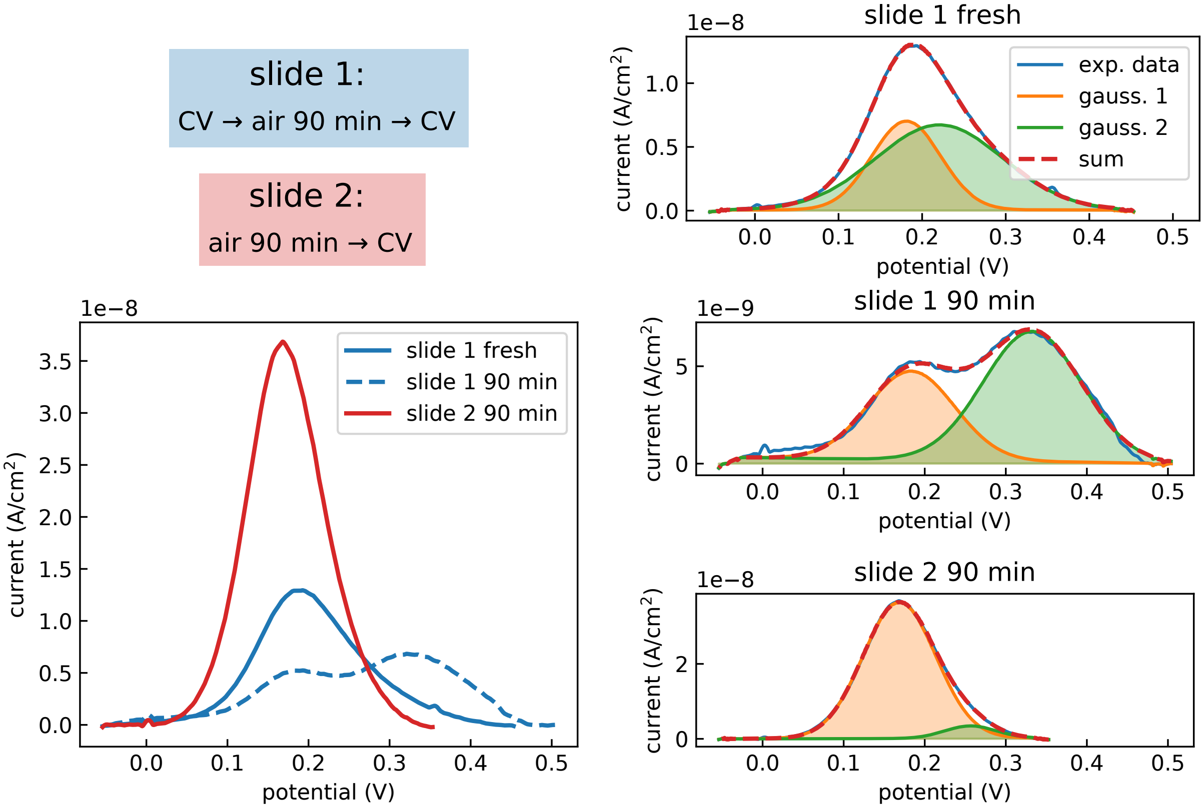

Figure 5.6: Cyclic voltammograms for 0.05% $FcC_{16}SH$ samples. Left) Solid blue shows the oxidation trace for a freshly incubated SAM. Dashed blue shows the oxidation trace for the same SAM after being removed from the cell, cleaned with deionized water, and left in ambient conditions for 90 minutes. Pink shows the oxidation trace for a different SAM that was left in ambient conditions for 90 minutes without any prior CV experiments. Right) Each of the traces fit to two Gaussians, where the orange Gaussian corresponds to the disperse ferrocene population and the green to the less disperse. After slide 1 is exposed to air after the initial CV, the amplitude of the disperse peak is decreased by a factor of 5, and the less disperse peak is shifted to a higher potential, indicating a larger relative population of clustered ferrocene molecules.

6 | Outlook

In this thesis, we have shown how to prepare samples of ferrocene alkane thiol binary SAMs to tune the surface concentration of redox-active ferrocene molecules on the surface. We have shown how changing the concentration affects the number of adsorbed ferrocene thiols, and have characterized the adsorption using atomic force microscopy and cyclic voltammetry. We have shown a disparity between the number of molecules in the AFM images and the cyclic voltammograms.

One likely cause of this mismatch is that there may be additional redox-active ferrocenes in heterogeneous structures such as grain boundaries that are visible to the electrochemistry but invisible to the AFM. Since the CV measurements are performed on an area of 0.48 cm^2 and the AFM scans are measured on a 1 $\mu\mathrm{m}^2$, there are likely regions of heterogeneous structures on the global scale that are present in CV measurements. Future experiments to investigate this could involve using a smaller electrode area for the CV measurements. This can potentially be achieved by using scanning electrochemical microscopy (SECM), which allows for spatially resolved CV measurements on the sub-micron length scale.

Another potential cause of the disparity is that the number of molecules in each blob in the AFM image is assumed to be one, although each blob could contain multiple molecules. Since the adsorption kinetics of the $\mathrm{FcC_{16}SH}$ thiols are much faster than the diluting $\mathrm{C_{15}SH}$ alkane thiols [40], they may clump together during surface adsorption. We can investigate this in future experiments by performing electrostatic force microscopy (EFM) [4] on the samples, as seen in an example in figure 6.1. Images at 4 K will result in charging rings around the molecule due to the Coulomb blockade effect. We can use the number of charging rings to directly correlate the number of redox-active molecules on the surface.

It would also be interesting to explore different configurations of ferrocene thiol molecules

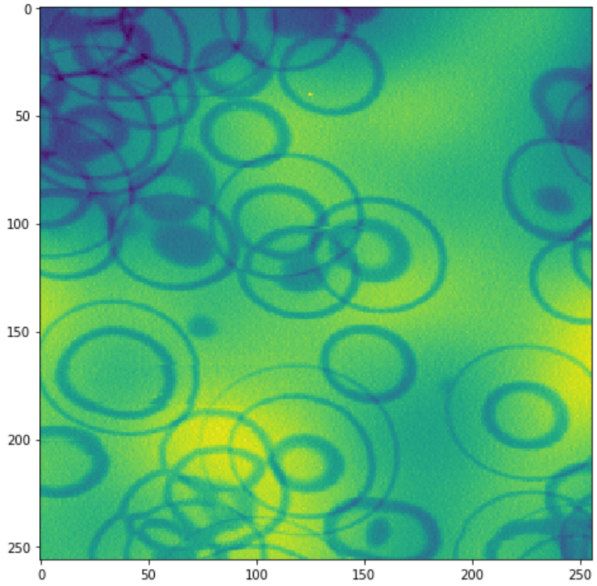

Figure 6.1: Example EFM experimental data of quantum dots on a tunnel barrier taken at 4 K. Charging rings can be seen here in the frequency shift channel. In the future molecule experiments, the charging rings can be used to determine the number of molecules in each blob.

in the future. One interesting candidate would be the C12 spiro molecule, as shown in figure 6.2. This molecule has one C12 arm functionalized with a ferrocene head and another C11 arm with no head group. In a unitary SAM with just this molecule, one could imagine that the nonfunctionalized arm would act as a self-diluting layer, creating regions of both grouped and individual ferrocene molecules. This would be useful for investigating blob molecule grouping. Additionally, it would make sample preparation easier as it would be a single thiol incubation solution.

With this work, we now better understand our thiol sample preparation and can use these prepared samples to probe the fundamental physics of single-electron charging of ferrocene molecules with AFM. For example, the reorganization of a single molecule in a vacuum and

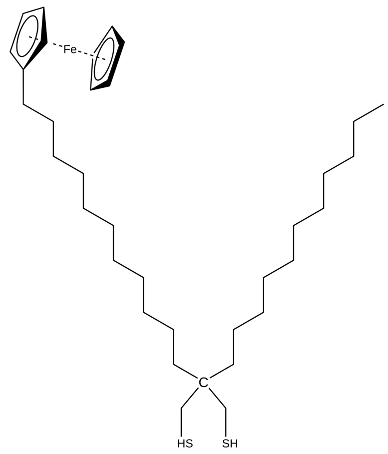

Figure 6.2: A spiro molecule with one C12 arm functionalized with a ferrocene head group and the other C11 arm is non-functionalized. This configuration allows the molecule to act as its own diluting layer.

the electron-phonon coupling can be explored in future experiments [5, 41].

Bibliography

[1] A. Roy-Gobeil, *Single-electron charging using atomic force microscopy.* PhD thesis, McGill University, 12 2016.

[2] L. P. Cockins, *High Aspect Ratio Cantilever Tips for Non-Contact Electrostatic Force Microscopy.* PhD thesis, McGill University, 8 2006.

[3] N. Elgrishi, K. J. Rountree, B. D. McCarthy, E. S. Rountree, T. T. Eisenhart, and J. L. Dempsey, "A practical beginner's guide to cyclic voltammetry," *Journal of Chemical Education*, vol. 95, no. 2, pp. 197–206, 2017.

[4] A. Mascaro, Y. Miyahara, T. Enright, O. E. Dagdeviren, and P. Grütter, "Review of time-resolved non-contact electrostatic force microscopy techniques with applications to ionic transport measurements," *Beilstein journal of nanotechnology*, vol. 10, no. 1, pp. 617–633, 2019.

[5] A. Roy-Gobeil, Y. Miyahara, K. H. Bevan, and P. Grutter, "Fully quantized electron transfer observed in a single redox molecule at a metal interface," *Nano letters*, vol. 19, no. 9, pp. 6104–6108, 2019.

[6] P. Zahl, T. Wagner, R. Möller, and A. Klust, "Open source scanning probe microscopy control software package gxsm," *Journal of Vacuum Science & Technology B, Nanotechnology and Microelectronics: Materials, Processing, Measurement, and Phenomena*, vol. 28, no. 3, pp. C4E39–C4E47, 2010.

[7] "Soft db instrumentation & digital signal processing applications." `https://www.softdb.com/dsp-instruments/`. Accessed: 2019-11-25.

[8] "Gnome x scanning microscopy." `http://gxsm.sourceforge.net/`. Accessed: 2019-11-25.

[9] M. A. Roseman, *Low Temperature Magnetic Force Microscopy Studies of Superconducting Niobium Films.* PhD thesis, McGill University, 10 2001.

[10] R.-P. Stomp, *Dissipative and Electrostatic Force Spectroscopy of InAs Quantum Dots by Non-contact Atomic Force Microscopy.* PhD thesis, McGill University, 8 2005.

[11] "Nanosensors: The world leader in scanning probes." `https://www.nanosensors.com/`. Accessed: 2019-12-09.

[12] U. Rabe, S. Hirsekorn, M. Reinstädtler, T. Sulzbach, C. Lehrer, and W. Arnold, "Influence of the cantilever holder on the vibrations of afm cantilevers," *Nanotechnology*, vol. 18, no. 4, p. 044008, 2006.

[13] T. Tsuji, K. Kobari, S. Ide, and K. Yamanaka, "Suppression of spurious vibration of cantilever in atomic force microscopy by enhancement of bending rigidity of cantilever chip substrate," *Review of Scientific Instruments*, vol. 78, no. 10, p. 103703, 2007.

[14] J. Lübbe, L. Tröger, S. Torbrügge, R. Bechstein, C. Richter, A. Kühnle, and M. Reichling, "Achieving high effective q-factors in ultra-high vacuum dynamic force microscopy," *Measurement Science and Technology*, vol. 21, no. 12, p. 125501, 2010.

[15] R. J. E. Merry, N. C. T. de Kleijn, M. J. G. van de Molengraft, and M. Steinbuch, "Using a walking piezo actuator to drive and control a high-precision stage," *IEEE/ASME Transactions on Mechatronics*, vol. 14, pp. 21–31, Feb 2009.

[16] T. Albrecht, P. Grütter, D. Horne, and D. Rugar, "Frequency modulation detection using high-q cantilevers for enhanced force microscope sensitivity," *Journal of Applied Physics*, vol. 69, no. 2, pp. 668–673, 1991.

[17] Y. Miyahara, H. Griffin, A. Roy-Gobeil, R. Belyansky, H. Bergeron, J. Bustamante, and P. Grutter, "Optical excitation of atomic force microscopy cantilever for accurate spectroscopic measurements," 2019.

[18] G. Poirier, "Coverage-dependent phases and phase stability of decanethiol on au (111)," *Langmuir*, vol. 15, no. 4, pp. 1167–1175, 1999.

[19] L. Chai and J. Klein, "Large area, molecularly smooth (0.2 nm rms) gold films for surface forces and other studies," *Langmuir*, vol. 23, no. 14, pp. 7777–7783, 2007.

[20] E. A. Weiss, G. K. Kaufman, J. K. Kriebel, Z. Li, R. Schalek, and G. M. Whitesides, "Si/sio2-templated formation of ultraflat metal surfaces on glass, polymer, and solder supports: Their use as substrates for self-assembled monolayers," *Langmuir*, vol. 23, no. 19, pp. 9686–9694, 2007.

[21] D. W. Mosley, B. Y. Chow, and J. M. Jacobson, "Solid-state bonding technique for template-stripped ultraflat gold substrates," *Langmuir*, vol. 22, no. 6, pp. 2437–2440, 2006.

[22] M. Hegner, P. Wagner, and G. Semenza, "Ultralarge atomically flat template-stripped au surfaces for scanning probe microscopy," *Surface Science*, vol. 291, no. 1-2, pp. 39–46, 1993.

[23] F. Schreiber, "Structure and growth of self-assembling monolayers," *Progress in surface science*, vol. 65, no. 5-8, pp. 151–257, 2000.

[24] J. C. Love, L. A. Estroff, J. K. Kriebel, R. G. Nuzzo, and G. M. Whitesides, "Self-assembled monolayers of thiolates on metals as a form of nanotechnology," *Chemical reviews*, vol. 105, no. 4, pp. 1103–1170, 2005.

[25] G. K. Rowe and S. E. Creager, "Redox and ion-pairing thermodynamics in self-assembled monolayers," *Langmuir*, vol. 7, no. 10, pp. 2307–2312, 1991.

[26] G. K. Pang, K. Baba-Kishi, and A. Patel, "Topographic and phase-contrast imaging in atomic force microscopy," *Ultramicroscopy*, vol. 81, no. 2, pp. 35–40, 2000.

[27] S. Sadewasser and T. Glatzel, *Kelvin probe force microscopy*, vol. 48. Springer, 2012.

[28] R. G. Compton and C. E. Banks, *Understanding voltammetry.* World Scientific, 2011.

[29] Y. Feng, E. R. Dionne, V. Toader, G. Beaudoin, and A. Badia, "Odd–even effects in electroactive self-assembled monolayers investigated by electrochemical surface plasmon resonance and impedance spectroscopy," *The Journal of Physical Chemistry C*, vol. 121, no. 44, pp. 24626–24640, 2017.

[30] A. J. Bard, L. R. Faulkner, J. Leddy, and C. G. Zoski, *Electrochemical methods: fundamentals and applications*, vol. 2. wiley New York, 1980.

[31] P. H. Eilers and H. F. Boelens, “Baseline correction with asymmetric least squares smoothing,” *Leiden University Medical Centre Report*, vol. 1, no. 1, p. 5, 2005.

[32] P. Biesheuvel and J. Dykstra, “The difference between faradaic and nonfaradaic processes in electrochemistry,” *arXiv preprint arXiv:1809.02930*, 2018.

[33] E. R. Dionne and A. Badia, “Electroactive self-assembled monolayers detect micelle formation,” *ACS applied materials & interfaces*, vol. 9, no. 6, pp. 5607–5621, 2017.

[34] E. R. Dionne, V. Toader, and A. Badia, “Microcantilevers bend to the pressure of clustered redox centers,” *Langmuir*, vol. 30, no. 3, pp. 742–752, 2014.

[35] A. L. Eckermann, D. J. Feld, J. A. Shaw, and T. J. Meade, “Electrochemistry of redox-active self-assembled monolayers,” *Coordination chemistry reviews*, vol. 254, no. 15-16, pp. 1769–1802, 2010.

[36] M. Ter Haak, “Machine learning for blob detection in high-resolution 3d microscopy images,” 2018.

[37] M.-T. Lee, C.-C. Hsueh, M. S. Freund, and G. S. Ferguson, “Air oxidation of self-assembled monolayers on polycrystalline gold: the role of the gold substrate,” *Langmuir*, vol. 14, no. 22, pp. 6419–6423, 1998.

[38] M. H. Schoenfisch and J. E. Pemberton, “Air stability of alkanethiol self-assembled monolayers on silver and gold surfaces,” *Journal of the American Chemical Society*, vol. 120, no. 18, pp. 4502–4513, 1998.

[39] T. M. Willey, A. L. Vance, T. Van Buuren, C. Bostedt, L. Terminello, and C. Fadley, “Rapid degradation of alkanethiol-based self-assembled monolayers on gold in ambient laboratory conditions,” *Surface Science*, vol. 576, no. 1-3, pp. 188–196, 2005.

[40] W. Pan, C. Durning, and N. Turro, “Kinetics of alkanethiol adsorption on gold,” *Langmuir*, vol. 12, no. 18, pp. 4469–4473, 1996.

[41] K. H. Bevan, A. Roy-Gobeil, Y. Miyahara, and P. Grutter, “Relating franck-condon blockade to redox chemistry in the single-particle picture,” *The Journal of chemical physics*, vol. 149, no. 10, p. 104109, 2018.

[42] L. Tröger and M. Reichling, “Quantification of antagonistic optomechanical forces in an interferometric detection system for dynamic force microscopy,” *Applied Physics Letters*, vol. 97, p. 213105, nov 2010.

[43] H. Hölscher, P. Milde, U. Zerweck, L. M. Eng, and R. Hoffmann, “The effective quality factor at low temperatures in dynamic force microscopes with Fabry–Pérot interferometer detection,” *Applied Physics Letters*, vol. 94, p. 223514, jun 2009.

[44] A. Von Schmidsfeld and M. Reichling, “Controlling the opto-mechanics of a cantilever in an interferometer via cavity loss,” *Applied Physics Letters*, vol. 107, no. 12, pp. 2–7, 2015.

[45] M. Vogel, C. Mooser, K. Karrai, and R. J. Warburton, “Optically tunable mechanics of microlevers,” *Applied Physics Letters*, vol. 83, pp. 1337–1339, aug 2003.

[46] P. R. Wilkinson and J. R. Pratt, “Analytical model for low finesse, external cavity, fiber Fabry–Perot interferometers including multiple reflections and angular misalignment,” *Applied Optics*, vol. 50, p. 4671, aug 2011.

[47] T. R. Albrecht, P. Grütter, D. Horne, and D. Rugar, “Frequency modulation detection using high- Q cantilevers for enhanced force microscope sensitivity,” *Journal of Applied Physics*, vol. 69, pp. 668–673, jan 1991.

[48] D. Rugar, H. J. Mamin, and P. Guethner, “Improved fiber-optic interferometer for atomic force microscopy,” *Applied Physics Letters*, vol. 55, pp. 2588–2590, dec 1989.

[49] N. Ismail, C. C. Kores, D. Geskus, and M. Pollnau, “Fabry-Pérot resonator: spectral line shapes, generic and related Airy distributions, linewidths, finesses, and performance at low or frequency-dependent reflectivity,” *Optics Express*, vol. 24, p. 16366, jul 2016.

[50] D. T. Smith, J. R. Pratt, and L. P. Howard, “A fiber-optic interferometer with sub-picometer resolution for dc and low-frequency displacement measurement,” *Review of Scientific Instruments*, vol. 80, p. 035105, mar 2009.

[51] V. Subba-Rao, C. Sudakar, J. Esmacher, M. Pantea, R. Naik, and P. M. Hoffmann, “Improving a high-resolution fiber-optic interferometer through deposition of a TiO2 reflective coating by simple dip-coating,” *Review of Scientific Instruments*, vol. 80, p. 115104, nov 2009.

[52] H. I. Rasool, P. R. Wilkinson, A. Z. Stieg, and J. K. Gimzewski, “A low noise all-fiber interferometer for high resolution frequency modulated atomic force microscopy imaging in liquids,” *Review of Scientific Instruments*, vol. 81, p. 023703, feb 2010.

[53] D. M. Weld and A. Kapitulnik, “Feedback control and characterization of a microcantilever using optical radiation pressure,” *Applied Physics Letters*, vol. 89, p. 164102, oct 2006.

[54] A. Labuda, K. Kobayashi, Y. Miyahara, and P. Grütter, “Retrofitting an atomic force microscope with photothermal excitation for a clean cantilever response in low Q environments,” *Review of Scientific Instruments*, vol. 83, no. May, p. 053703, 2012.

[55] K. Kobayashi, H. Yamada, and K. Matsushige, “Reduction of frequency noise and frequency shift by phase shifting elements in frequency modulation atomic force microscopy,” *Review of Scientific Instruments*, vol. 82, no. 3, p. 033702, 2011.

[56] A. Labuda, Y. Miyahara, L. Cockins, and P. H. Grutter, “Decoupling conservative and dissipative forces in frequency modulation atomic force microscopy,” *Physical Review B*, vol. 84, p. 125433, sep 2011.

[57] J. E. Sader, J. W. Chon, and P. Mulvaney, “Calibration of rectangular atomic force microscope cantilevers,” *Review of scientific instruments*, vol. 70, no. 10, pp. 3967–3969, 1999.

[58] E. Hecht, *Optics*. Pearson education, Addison-Wesley, 2002.

[59] O. Svelto and D. C. Hanna, *Principles of lasers*, vol. 5. Springer, 2010.